Contactless quantum non-linear optics with cold Rydberg atoms

BUSCHE, HANNES

Contactless quantum non-linear optics with cold Rydberg atoms

Hannes Busche

A thesis submitted in partial fulfilment
of the requirements for the degree of
Doctor of Philosophy

Department of Physics
Durham University

2017

Abstract

Rydberg quantum optics achieves optical non-linearities at the single-photon level by mapping the strong dipolar interactions between Rydberg atoms in cold atomic gases onto light fields using electromagnetically-induced transparency and photon storage. The non-linearities are a direct consequence of the long-range character of the interaction which allows a single photon to modify the optical response in a volume containing many atoms. In this thesis, the long-range character of the resulting effective photon-photon interaction is directly observed as photons propagating in non-overlapping optical modes are stored as collective Rydberg excitations in adjacent and non-overlapping microscopic clouds of ^{87}Rb atoms. While stored, van-der-Waals interactions imprint spatially non-uniform phase shifts in the collective excitations. These distort the photons' retrieval modes resulting in anti-correlated retrieval between the original modes. In this first demonstration of contactless effective interactions between photons, these effects are observed between photons separated by more than 15 times their wavelength, well above the optical diffraction limit. This represents a promising step towards the implementation of scalable, multichannel quantum optical devices such as quantum gates.

The experiments are enabled by a new, specialised experimental setup centred around a pair of in-vacuo aspheric lenses. These provide optical resolution of order 1 µm to optically trap and address the ensembles separated by distances well below the range of Rydberg interactions. The ensembles are prepared in ≈ 100 ms thanks to efficient loading of a magneto-optical trap (MOT) from an atomic beam produced by a 2D MOT. Combined with the ability to recycle the ensembles $> 20\,000$ times, effective cycle times exceeding 100 kHz enable the acquisition of large datasets for the analysis of photon statistics within a matter of minutes.

Declaration

I confirm that no part of the material offered has previously been submitted by myself for a degree in this or any other university. Where material has been generated through joint work, the work of others has been indicated.

Hannes Busche
Durham, 22nd February 2017

Contents

List of Figures

List of Tables

1 Introduction

One of the most remarkable properties of light – and electromagnetic radiation more generally – is the lack of intrinsic interactions with other light and its weak interaction with the environment. While direct interactions between photons are impossible, photons can interact via virtual charged fermion loops [1, 2], though in practice these processes are only relevant at extreme energies. The absence of interactions makes electromagnetic radiation an excellent carrier of information that provides insights into fundamental processes in nature, ranging from cosmological scales in astronomy to sub-microscopic in the life sciences. At the same time, the ability to control light with optics and transmit information through fibre networks constitutes a fundamental pillar of today's information society [3]. Robustness and ease of transmission make photons attractive as quantum information carriers [4]. Yet, the lack of intrinsic interactions also makes coherent processing of the encoded information and implementing deterministic quantum optical devices notoriously difficult (figure 1.1 a).

Interactions between light fields can be mediated indirectly by matter if the light-matter interaction is strong enough to modify a medium's optical properties and evoke a non-linear response [5] (figure 1.1 b). Optical fields sufficiently strong to observe non-linear behaviour became available in the mid-twentieth century with the invention of the laser [6, 7]. Processing of quantum information encoded in optical qubits, however, requires effective interactions at the level of individual photons [8]. These can be achieved, for example, in cavity quantum electrodynamics (CQED) where the coupling between an atom and microwave or optical photons is strongly enhanced by high-Q resonators. CQED with microwave photons and Rydberg atoms

has enabled observation of the laws of quantum mechanics at the level of individual quanta [9, 10]. In the optical domain [11, 12], non-linearities at the single-photon level [13, 14], have been exploited for a variety of photon-controlled devices [15, 16], including a deterministic quantum gate [17].

Rydberg mediated non-linear optics

CQED and most other approaches to non-linear optics require photons that propagate in either the same or in overlapping optical modes inside a common medium. These requirements can be removed by creating a mapping between photons and quanta that exhibit strong and long-range interactions such as highly excited Rydberg atoms [18, 19]. Their dipolar interactions range over many micrometers leading to a blockade mechanism that limits the number of Rydberg excitations in cold atomic ensembles to just one within a few micrometers [20–25]. Rydberg non-linear optics [26–29] employs electromagnetically-induced transparency (EIT) [30–32] to create the required mapping [33]. EIT provides coherent control over the propagation, transmission, and dispersion of a weak signal light field that is near-resonant with an atomic transition by introducing a control field coupling the excited state of the transition to a third, long-lived state – for example a Rydberg state or a ground state. If both signal and control fields are resonant, the atomic medium is rendered transparent for the signal light.[1] EIT can also be used to control the signal group velocity which enables storage of photons as atomic spin-waves by reducing it to zero [38, 39].

The first Rydberg mediated optical non-linearity was observed in Durham by Pritchard *et al.* in 2009 [26] as an intensity dependent transmission of an EIT signal field. The dipolar interactions shift the control field off resonance and render the initially transparent medium opaque in the vicinity of another photon [26, 40, 41] which can lead to strong anti-

[1] EIT also gives rise to strong Kerr non-linearities [34], phase modulation at the few photon level [35, 36], and can be used to implement all-optical switches [37].

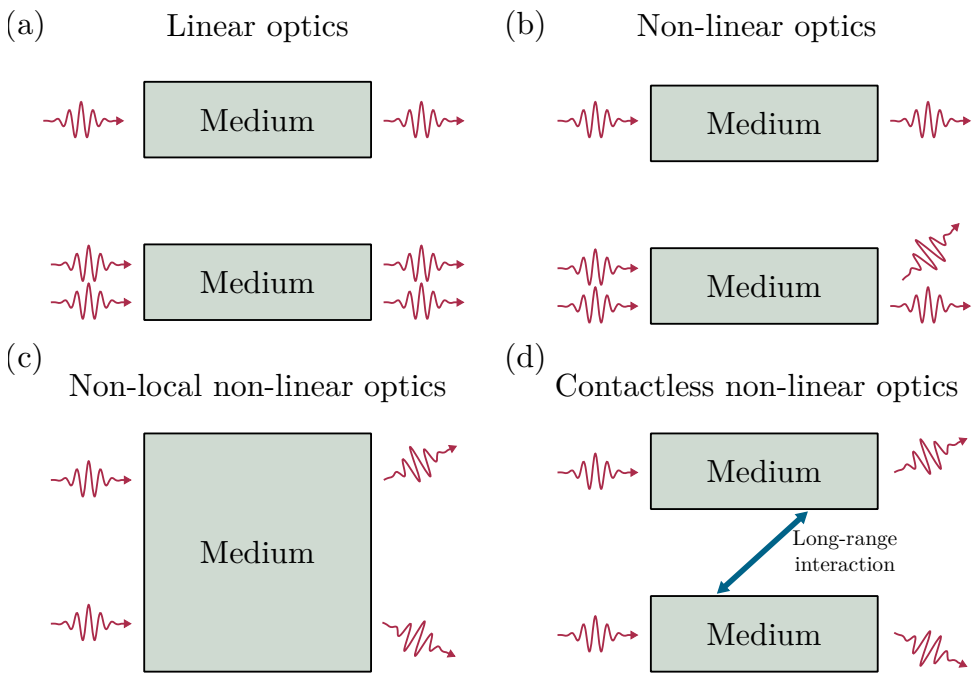

Figure 1.1: From linear optics to contactless non-linear optics. (a) In linear optics, the effect of an optical medium on a light field is independent of the intensity. (b) In non-linear media, the optical response depends on the intensity of the light. In some systems such as CQED or Rydberg quantum optics, non-linear responses at the single photon level are possible. (c) In non-local non-linear optics, the optical response depends not only on the local light intensity, but also on that in other regions of the medium, e.g. due to diffusion of heat or atomic excitations. (d) A completely contactless interaction between light fields in separated optical media can be induced if the light-fields evoke long-range interactions between them which are mediated through free space such as dipolar interactions between Rydberg atoms.

bunching in the transmitted light [40]. The resulting optical non-linearities are inherently 'non-local'[2] [42–44] (figure 1.1 c) as they build on long-range interactions and a single photon converted into a single excitation can alter the optical response in volumes containing hundreds of atoms.

Highly non-classical light [45–48] has also been observed as a consequence of blockade and interaction-induced dephasing [49–51] following storage of photons as collective Rydberg excitations [52] in microscopic cold atom clouds. Besides dissipative non-linearities, dispersive non-linearities can also be realised by detuning the EIT fields [53, 54] and attractive interactions can create two-photon bound states [54]. Applications of Rydberg quantum optics include optical switches [55], transistors [56–58], and phase shifters [59] gated by single photons, the generation of entangled atom-photon pairs [60], or, by reversing the blockade effect, single-photon subtractors [61]. Similarly, one can also image spatial distributions of Rydberg atoms due to the breakdown of Rydberg EIT in their vicinity [62–64].

Contactless effective photon interactions

The above examples all exploit the long-range character of Rydberg-mediated non-linearities and an emergence of spatial correlations during storage [51] has been observed indirectly within a single storage medium [48]. However, a truly contactless non-linearity [65] between spatially separated photons (figure 1.1 d) remained to be observed.

Contactless optical non-linearities mediated by long-range Rydberg interactions can be helpful to overcome no-go theorems for deterministic optical quantum information processing (QIP) based on purely local non-linearities [66, 67] and implement deterministic gates for photonic qubits [43, 68, 69]. In CQED these had to be circumnavigated by consecutive

[2]The term non-local non-linear optics was originally used to describe non-linear responses to classical light fields. To avoid confusion with the concept of non-locality in quantum mechanics, this thesis mostly refers to long-range or contactless interactions instead.

interaction of the qubits with an atom inside the cavity [17]. A variety of approaches have been outlined for optical quantum gates based on Rydberg interactions [43, 68–71]. Schemes based on contactless, Rydberg mediated interactions [70, 71] between spatially separated optical modes mimic Rydberg-based schemes for atomic qubits [20, 72, 73] and may be particularly well suited for integration into scalable multichannel photonic devices, e.g. based on photonic waveguides [74], if atom-surface interactions can be controlled [75–77].

'Non-local' optical non-linearities (figure 1.1 c) have been observed previously in liquid crystals [78, 79] mediated by spatial reorientation of molecules or diffusion processes, e.g. of heat in lead glass [80] or excitations in atomic vapours [81]. However these were limited to strong light fields in the same media, or media which are in thermal contact [82]. Similarly, in interaction enhanced, EIT-based imaging of Rydberg atoms immersed in an ultra-cold gas, the EIT fields can induce non-radiative energy transfer between excitations that results in a spatial change of the transmission over time [64]. In linear-optics [83], a remote interaction between two photons can be engineered via entanglement swapping [84] where two photons are entangled indirectly as two entangled partners interact on a beam splitter, but the result of the interaction is inherently probabilistic.

This thesis demonstrates an effective contactless interaction between photons that are stored as strongly interacting collective Rydberg excitations and do not touch, as neither their optical modes nor the atomic storage media overlap [85]. In analogy to experiments with individual Rydberg atoms [24, 25, 86] and collectively encoded qubits [87], we implement two channels for signal photons which are separated by an adjustable distance on the order of 10 µm, up to 20 times the wavelength of the signal light. The channels each consist of a tightly focussed optical mode for the signal light and microscopic, optically trapped cold atom clouds that serve as storage media [88]. The interactions manifest themselves in anti-correlations in the photon retrieval between channels which are the result of non-uniform phase gradients [45, 46, 49, 50, 89] imprinted by

Van der Waals (VdW) interactions between pairs of individual atoms that contribute to the collective states. The modified phase relation leads to a change in the photons' retrieval modes [71]. Complementary work has recently observed spatial correlations and robust $\pi/2$-phase shifts as a result of interactions between a stored photon and signal photons propagating under Rydberg EIT conditions in independent modes [90].

New experimental setup

In order to perform the experiments described above, a new setup for experiments in Rydberg quantum optics [28, 29] using laser cooled [91] and optically trapped [92] Rb atoms has been built during this thesis. The most important features of the setup are the following. Near diffraction-limited optical resolution ($\approx 1\,\mu m$), well below the range of Rydberg interactions, is achieved by high numerical aperture (NA) aspheric lenses which are placed inside the vacuum chamber [93]. They allow the creation of tightly focussed optical tweezers that trap the atomic media, as well as individual addressing of the ensembles with independent signal beams. Fast preparation of the atomic ensembles is achieved by reducing the time needed to load atoms into a magneto-optical trap (MOT) as a first step in the preparation of the media thanks to a two-dimensional magneto-optical trap (2D MOT) [94] which provides a dense and cold atomic beam as an atom source. Combined with the ability to recycle the microscopic ensembles several 10 000 times before reloading the traps, we can thus perform on the order of 100 000 individual experiments per second which is a great advantage when large data sets are required, e.g. to analyse correlations in photon counting statistics.

Because of the high resolution below the range of dipole blockade and Rydberg interactions more generally, the setup could, in principle, also perform other experiments beyond Rydberg quantum optics. These include experiments on interactions between single Rydberg atoms trapped in two adjacent [95] or large arrays of optical tweezers [96], e.g. for QIP [19, 97] or quantum simulation [98]. Moreover, microscopic atom clouds of multiple

atoms that support no more than a single collective Rydberg excitation may also be used as single atom source [99] or collectively encoded qubits [87].[3]

Thesis structure

This thesis is structured as follows: Chapter 2 reviews and summarises the most important properties of Rydberg atoms and their interactions, and how they can be mapped onto photons using EIT and photon storage. Chapter 3 introduces the new experimental setup. Finally, effective interactions at the single photon level are demonstrated within a single medium in chapter 4 and as contactless interactions between non-overlapping photons in spatially separated channels in chapter 5.

Publications arising from this work

- H. Busche, P. Huillery, S. W. Ball, T. V. Ilieva, M. P. A. Jones, and C. S. Adams, "Contactless non-linear optics mediated by long-range Rydberg interactions", Nat. Phys., to appear (2017). [85]

- H. Busche, S. W. Ball, and P. Huillery, "A high repetition rate experimental setup for quantum non-linear optics with cold Rydberg atoms", Eur. Phys. J. Spec. Top. **225,** 2839–2861 (2016). [88]

Related publications

- D. Maxwell, D. J. Szwer, D. Paredes-Barato, H. Busche, J. D. Pritchard, A. Gauguet, M. P. A. Jones, and C. S. Adams, "Microwave control of the interaction between two optical photons", Phys. Rev. A **89,** 043827 (2014). [47]

- D. Maxwell, D. J. Szwer, D. Paredes-Barato, H. Busche, J. D. Pritchard, A. Gauguet, K. J. Weatherill, M. P. A. Jones, and C. S. Adams, "Storage and Control of Optical Photons Using Rydberg Polaritons", Phys. Rev. Lett.. **110,** 103001 (2013). [46]

[3] Experiments on Rydberg based ion sources [100] are not feasible in the setup as ion detection was omitted.

Other publications by the author

- C. S. Hofmann, G. Günter, H. Schempp, N. L. M. Müller, A. Faber, H. Busche, M. Robert-de-Saint-Vincent, S. Whitlock, and M. Weidemüller, "An experimental approach for investigating many-body phenomena in Rydberg-interacting quantum systems", Front. Phys. **9,** 571–586 (2014). [101]

2 Rydberg non-linear optics: Background

Due to the lack of intrinsic interactions between optical photons, any interaction between them needs to be mediated indirectly by coupling them to an interacting matter system. If the photons are to be made interact without spatial overlap, its interaction range has to exceed the minimum possible size of their optical modes, i.e. the optical diffraction limit which is of the order of 1 µm. Moreover, both the light-matter coupling and the interaction must be coherent if the arising effective interaction shall maintain or process the photons' properties at the quantum level.

This chapter introduces the fundamental ingredients used in Rydberg quantum optics [28, 29] to achieve effective interactions between individual photons [8]: Rydberg atoms [18, 19] contribute their strong and long-ranged dipolar interactions (section 2.1) while EIT [32] adds a coherent mapping between light and matter (section 2.2). This combination results in strong optical non-linearities [26, 40] that can be further enhanced by interaction-induced dephasing [49, 50, 85] when storing the photons as collective Rydberg excitations (section 2.3) to increase interaction times [45, 46, 89].

2.1 Rydberg atoms and their interactions

Rydberg atoms [18, 19] are atoms whose valence electron is in an excited state with high principal quantum number n. Their name originates from the fact that the binding energies E_n are well described by Rydberg's

formula

$$E_n = -\frac{Ry}{n^2} \tag{2.1}$$

which he introduced to describe the convergence of spectral lines in atomic hydrogen towards the ionisation threshold [102]. Here, Ry is the Rydberg constant and n the principal quantum number. Many of their properties can be derived from Bohr's atom model [103]. The accuracy of this rather simple model is a consequence of the high probability to find the highly excited valence electron far from the remaining shells such that the potential of the nucleus shielded by the remaining electrons is Coulomb-like [18, 19, 104].

The large electron orbital radius $\propto n^2$ gives rise to dramatic scalings of various properties with the principal quantum number n which are summarised in table 2.1 [18, 19, 104]. Amongst others, they include a high polarisability $\propto n^7$, large transition dipole moments $\propto n^2$ between adjacent Rydberg states, and long radiative lifetimes $\propto n^3$ (for low angular momentum states). The dipole moments and polarisability are responsible for the strong, µm-ranged dipolar interactions and render them sensitive to both DC electric [105–111] and microwave fields [9, 46, 112] providing convenient handles to control and manipulate the atoms. Their lifetimes of order 10 to 100 µs result from the increasingly low overlap between the large Rydberg orbitals with the ground and other low-lying states and are an important prerequisite not only for applications in quantum simulation [64, 98, 113–115] and information processing [19, 20, 72, 73, 97, 116], but also make Rydberg atoms suitable for use in quantum optics in the context of EIT [26, 33, 40, 117] and photon storage [45, 46] which require long-lived atomic states (sections 2.2.3 and 2.3).

In alkali atoms, there is a non-zero probability to find the valance electron inside the closed inner shells for Rydberg states with low orbital angular momentum $L \leq 3$ [18]. Here, the electron is less efficiently shielded from nuclear charges and it also interacts other electrons. These effects are

Table 2.1: Scaling of Rydberg atom properties with principal quantum number n [18, 19, 104].

Property	Scaling
Binding energy	n^{-2}
Energy difference of adjacent states	n^{-3}
Orbital radius	n^{2}
Polarisability	n^{7}
Radiative lifetime	n^{3}
Ionisation energy	n^{-4}
Van der Waals interactions (C_6)	n^{11}
Van der Waals blockade radius $r_b^{(6)}$	$n^{11/6}$
Resonant dipole interactions (C_3)	n^{4}
Resonant dipole blockade radius $r_b^{(3)}$	$n^{4/3}$

accounted for by introducing the quantum defect δ_{nLJ} [118] into equation 2.1,

$$E_n = -\frac{Ry}{(n-\delta_{nLJ})^2}, \tag{2.2}$$

which depends on the atomic species and the state's orbital and total angular momentum, and principal quantum numbers, L, J, and n [18]. Quantum defects are usually obtained from spectroscopic measurements, e.g. by the group of T. Gallagher for Rb [119, 120]. The value for the Rydberg constant of Rb is $Ry/hc = 109\,736.605\,\mathrm{cm}^{-1}$ [18].

2.1.1 Dipolar interactions

Besides their long lifetimes, the attractiveness of Rydberg atoms for applications in quantum simulation, information processing, and Rydberg quantum optics [28, 29] is a consequence of their strong dipolar interactions which are a result of the large transition dipole moments. In the context of Rydberg quantum optics, the µm-range of the interaction enables a highly non-local change in the optical response of a medium [42–44, 65, 69, 121,

122] and enables the central result of this thesis, the demonstration of effective interactions between photons in non-overlapping optical modes and media [85] (chapter 5), since it by far exceeds the diffraction limited size of the optical modes.

Strictly speaking, Rydberg atoms do not possess a permanent dipole moment, unless a strong external electric field is applied to break symmetry. However, when interacting with a second Rydberg atom, their original states mix with other Rydberg states and the atoms can interact via the coupling of the induced transition dipole moments and the exchange of virtual microwave photons [18, 19]. The interaction potential between two dipoles $\vec{d_1}$ and $\vec{d_2}$ separated by $\vec{r}$ is [123]

$$V\left(\vec{r}\right) = \frac{1}{4\pi\epsilon_0}\left(\frac{\vec{d_1}\cdot\vec{d_2}}{|\vec{r}|^3} - \frac{3(\vec{d_1}\cdot\vec{r})(\vec{d_2}\cdot\vec{r})}{|\vec{r}|^5}\right). \tag{2.3}$$

To understand the interaction between two Rydberg atoms in states $|r\rangle$ and $|r'\rangle$, it is convenient to consider pair states $|rr'\rangle \leftrightarrow |r''r'''\rangle$ [18] and compare $V(\vec{r})$ to the energy difference between $|rr'\rangle$ and $|r''r'''\rangle$

$$\Delta E = E_{r''} + E_{r'''} - E_r - E_{r'} \tag{2.4}$$

for the atoms in absence of interaction-induced energy shifts on the pair states.

Depending on ΔE and the Rydberg states under consideration, the following interactions can be distinguished:

1. **Van der Waals interactions**: If ΔE is large compared to the interaction potential $V(\vec{r})$, i.e. if the separation $\vec{r}$ between the atoms is large, they interact via the VdW potential

$$V_{VdW} = -\frac{C_6}{|\vec{r}|^6} \tag{2.5}$$

where the VdW coefficient C_6 describes the interaction strength [18]. They typically occur when two atoms in the same state $|r\rangle = |r'\rangle$

or if $|r\rangle$ and $|r'\rangle$ with $\Delta L \neq 1$ are not directly dipole coupled. The $\propto 1/|\vec{r}|^6$ dependence can be understood as the interaction has to occur as a second order dipole coupling via intermediate states $|r''r'''\rangle$ and the exchange of two instead of single virtual microwave photons.

The interaction strength scales as $C_6 \propto (n^4)^2/n^{-3} = n^{11}$. For interactions between two Rb atoms in $|rr\rangle = |60S_{1/2}, 60S_{1/2}\rangle$ the interaction strength is $C_6/\hbar = -140\,\mathrm{GHz}\,\mu\mathrm{m}^6$ [104, 124, 125]. The sign of the VdW interaction depends on ΔE. For Rb atoms in high-lying $S_{1/2}$-states, the interactions are repulsive as $C_6 < 0$. In order to calculate C_6 accurately, it is usually necessary to take multiple adjacent pair states into account [18, 104, 124, 125].

2. **Resonant dipole interactions**: If the potential $V(\vec{r})$ is strong enough to overcome the energy shift ΔE, e.g. at short distances, they interact directly via resonant dipole interactions [18]

$$V_{dd}(\vec{r}) = \pm\frac{C_3}{|\vec{r}|^3}. \tag{2.6}$$

The interaction strength scales as $C_3 \propto n^4$. For the pair states $|rr\rangle = |60S_{1/2}, 60S_{1/2}\rangle \leftrightarrow |r'r''\rangle = |60P_{3/2}, 59P_{3/2}\rangle$ in Rb, the interaction strength is $C_3/\hbar = 14.3\,\mathrm{GHz}\,\mu\mathrm{m}^3$ [104, 125].

Resonant dipole interactions can occur between Rydberg atoms in non-dipole coupled states if another, dipole coupled pair state is nearby [18]. A prominent example for Rb $|nS_{1/2}\rangle$-states occurs at $|38S_{1/2}39S_{1/2}\rangle \leftrightarrow |38P_{3/2}38P_{3/2}\rangle$ [126]. Alternatively, pair states can be brought into resonance with each other by applying an electric field that induces Stark shifts on the individual, highly polarisable Rydberg states [127, 128]. These situations are referred to as Förster resonance [129–131] since the underlying non-radiative energy transfer between the atoms is equivalent to Förster resonant energy transfer (FRET) between acceptor and donor molecules [64, 132, 133]. It represents an analogy to Feshbach resonances [134] between ground

state atoms where their scattering length can be tuned by applying external magnetic fields. Förster resonances have also been observed between three or even four Rydberg atoms [135, 136].

Obviously, resonant dipole interactions are present if two atoms are initially prepared in a pair state $|rr'\rangle$ where $|r\rangle$ and $|r'\rangle$ are directly dipole coupled, and which is intrinsically resonant with $|r'r\rangle$ and $\Delta E = 0$. These exchange or 'excitation hopping' processes can occur over large spatial separations [137, 138] and are well suited to simulate energy transfer in biological systems and processes, e.g. photosynthesis, or spin models [64, 133, 137, 138].

In the previous discussion, the angular dependence of the interaction was omitted. While VdW interactions between atoms in $|nS_{1/2}\rangle$-states are almost isotropic, the angular dependence [139] has to be taken into account for resonant dipole interactions and VdW interactions involving states with orbital angular momentum $L \neq 0$ [104, 125].

2.1.2 Dipole blockade

The hallmark of dipolar interactions between Rydberg atoms [18, 19] is the effect of dipole or excitation blockade which prevents the creation of multiple Rydberg excitations in a cold atomic ensemble within a few µm of each other [21]. It distinguishes Rydberg atoms from other quanta exhibiting strong dipolar interactions like polar molecules [140, 141] or magnetic ground-state atoms [142, 143] and arises from their extraordinarily large interaction strength which induces significant energy shifts over distances that exceed typical mean inter-atomic spacings. Dipole blockade was first proposed in two seminal papers by Jaksch *et al.* and Lukin *et al.* [20, 116] as a conditional switch to implement a universal quantum gate between atomic qubits. Similarly, blockade is of fundamental importance in Rydberg quantum optics [28, 29] as it allows a single photon to change the optical response of an atomic medium over a volume of many μm^3 [56, 57, 59, 61].

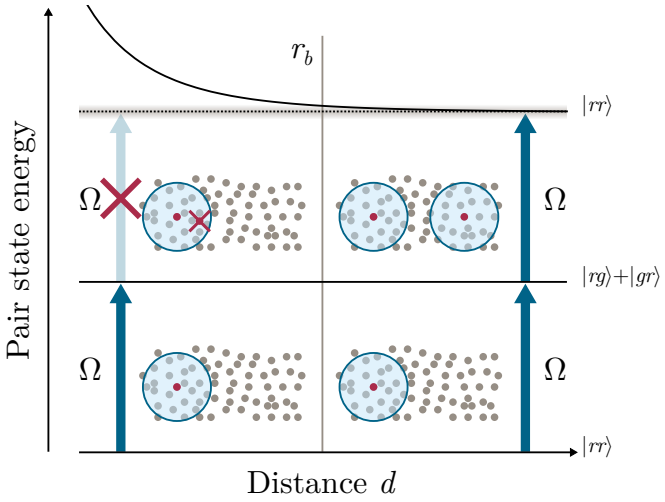

Figure 2.1: Dipole blockade between Rydberg atoms. Below a criticial distance, the blockade radius r_b, the dipolar interactions between Rydberg atoms exceed the linewidth of the excitation field Ω such that creation of multiple Rydberg excitations within a volume defined by r_b is prevented.

The effect of Rydberg blockade is illustrated in figure 2.1. Consider two atoms separated by a distance d and an excitation laser field with Rabi frequency Ω in resonance with a transition between the atoms' ground state $|g\rangle$ and some Rydberg state $|r\rangle$. Rydberg blockade occurs in regions where the interaction potential between Rydberg atoms is strong enough to shift the energy of the pair state $|rr\rangle$ by more than its linewidth [20, 21, 116],

$$\hbar\Omega = \frac{C_\kappa}{r_b^{(\kappa)^\kappa}}, \tag{2.7}$$

where $\kappa = 6$ for VdW and $\kappa = 3$ for resonant dipole interactions.[1] The linewidth is given by either the natural linewidth Γ_r of the Rydberg state or the linewidth of the laser field, typically Ω, whichever is larger.[2] The

[1] Of course, C_κ, and hence also $r_b^{(\kappa)}$ may depend on the angular orientation of the dipole moments with respect to each other and $\vec{r}$.

[2] For short excitation pulses, the linewidth can also be determined by Fourier broadening. In thermal vapour cells at room temperature, dipole blockade is yet to be observed

blockaded volume is defined by the blockade radius [21]

$$r_b^{(\kappa)} = \sqrt[\kappa]{\frac{C_\kappa}{\hbar\Omega}}. \tag{2.8}$$

For $d > r_b^{(\kappa)}$, both atoms can be excited resulting in the pair state $|rr\rangle$. However, for $d < r_b^{(\kappa)}$ blockade prevents multiple excitations resulting in one of the pair states $|gr\rangle$ or $|rg\rangle$. The scaling of the blockade radius with the principal quantum number n can be deduced as $r_b^{(6)} \propto C_6^{1/6} \propto n^{11/6}$ for VdW and $r_b^{(3)} \propto C_3^{1/3} \propto n^{4/3}$ for resonant dipole interactions.

If the density of a cold atom ensemble is sufficiently high to find multiple atoms within $r_b^{(\kappa)}$, dipole blockade limits the number of Rydberg excitations within an excitation volume defined by the geometry of the ensemble and the excitation lasers. Consequently, dipole blockade was first observed indirectly as a saturation of the number of Rydberg excitations in a cold atomic gas [22, 23]. This saturation of the excitation number can lead to sub-Poissonian counting statistics [144–147], the emergence of spatial correlations arising from geometric constraints imposed by the blockade [98, 148, 149], and the formation of Rydberg atom crystals [114, 150, 151]. Rydberg blockade has not only been observed in atomic ensembles but also directly between individual atoms [24, 25] leading to a controlled NOT-gates and entanglement generation between two atomic qubits [72, 73].

Collective Rydberg excitations

Within the blockaded volume, a single Rydberg excitation is shared amongst all $\mathcal{N}$ atoms [20] forming the collective superposition state

$$|R\rangle = \frac{1}{\sqrt{\mathcal{N}}} \sum_j \left(|r_j\rangle \otimes \bigotimes_{k \neq j} |g_k\rangle \right) \tag{2.9}$$

due to strong Doppler broadening.

where $|g_j\rangle$ and $|r_j\rangle$ correspond to the ground and Rydberg state of an individual atom j. As a result of the blockade mechanism, the atoms in $|R\rangle$ are maximally entangled [19, 20]. This superposition state is also referred to as Rydberg 'superatom'. An important consequence of the collective nature is a collective enhancement of the Rabi frequency $\sqrt{\mathcal{N}}\Omega$ to drive transitions between the collective ground state $|G\rangle = |g_1\rangle \otimes \ldots |g_\mathcal{N}\rangle$ and $|R\rangle$ by the square root of the atom number $\mathcal{N}$ [20]. This collective enhancement was initially observed as a density dependent increase of the excitation rate to Rydberg states [52] and later as a $\mathcal{N}$-dependent acceleration of collective Rabi oscillations [24, 25, 98, 152–154].

The collective nature of Rydberg excitations is of fundamental importance in Rydberg quantum optics [28, 29], in particular in the context of photon storage [45, 46]. The above definition of the collective state $|R\rangle$ does not consider a specific phase relation or different excitation probabilities for the individual atoms j. However, during photon storage [38, 39] the photons' phase $\phi(\vec{r}_j)$ and electric field amplitude $\epsilon(\vec{r}_j)$ at the position $\vec{r}_j$ are imprinted into

$$|R\rangle = \frac{1}{\sqrt{\sum_j \epsilon(\vec{r}_j)^2}} \sum_j \epsilon(\vec{r}_j) e^{i\phi(\vec{r}_j)} \left(|g_j\rangle \otimes \bigotimes_{k\neq j} |r_k\rangle \right) \tag{2.10}$$

forming a spin-wave that maintains the phase information and coherence of the original photon. This ensures retrieval of stored photons in their original modes [45, 46, 155–158].

2.2 Electromagnetically induced transparency

Mapping the strong interactions between Rydberg atoms [18, 19] onto light fields requires a coherent coupling between the light field and the atoms. A popular way to coherently manipulate the optical response of an atomic medium is EIT [32]. Here, the transmission and propagation

of a weak signal light field resonant with an atomic transition between a ground and an excited state can be manipulated by a strong control field which couples the excited to a third state with long coherence times. This results in a dramatic change in the optical response as the medium becomes transparent if both fields are resonant with the respective transitions. EIT was initially proposed by Harris *et al.* [30] and demonstrated by Boller *et al.* [31] in a Sr vapour using a Λ-scheme coupling to a (metastable) ground state, but can also be realised in a ladder scheme [159] provided that decoherence of the upper state is sufficiently low, i.e. with long-lived Rydberg states [33, 68].

Soon after the first demontration of EIT with Rydberg atoms by Mohapatra *et al.* [33], it was shown that their high polarisability can give rise to a giant electro-optical Kerr effect [108] when a Rydberg-EIT medium is subjected to an external electrical field which induces Stark shifts of the Rydberg state and thus an effective detuning of the control field. These initial experiments were carried out in a thermal vapour where Doppler broadening impedes the observation of atomic interaction effects [160]. In cold atoms however [117], transitions are sufficiently narrow such that Rydberg interactions can manifest themselves in strong optical non-linearities [27–29]; for example, an intensity dependent transmission as first demonstrated by Pritchard *et al.* [26]. Below, we give a brief overview of atom-light interactions and the resulting optical response in a three-level system and how it can be modified by Rydberg interactions on the single photon level.

2.2.1 Three-level atoms

The simplest example of an interaction of atoms and light is an idealised two-level system where two states are coherently coupled, e.g. a laser field coupling a stable atomic ground to an excited state or a microwave field coupling two long-lived, quasi-metastable Rydberg states. While the former enables probabilistic generation of single photons via incoherent

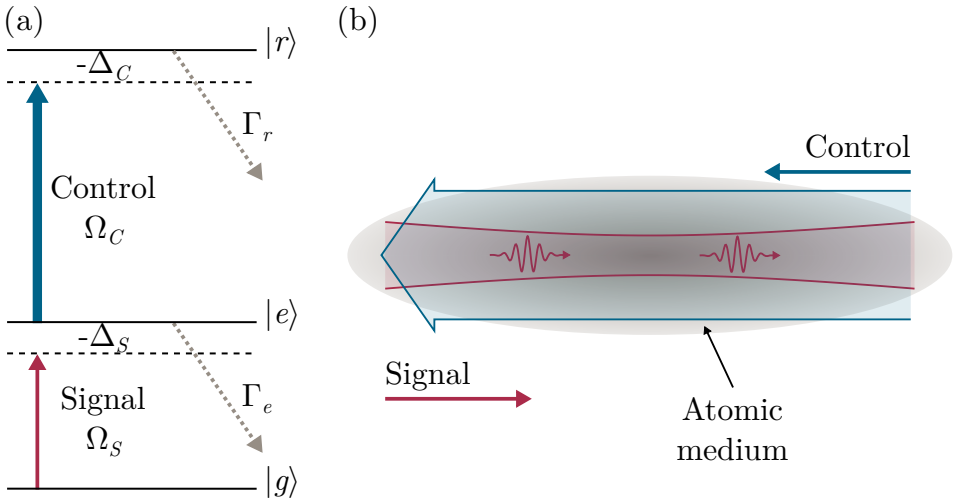

Figure 2.2: EIT in a three-level ladder system coupling to a Rydberg state. (a) Overview of relevant states and transitions with detunings and decoherence rates. The optical response of an atomic medium to a signal field coupling a ground state $|g\rangle$ to an intermediate state $|e\rangle$ can be controlled by a stronger control field coupling $|e\rangle$ to a Rydberg state $|r\rangle$. (b) Example of a typical implementation of EIT in a cold atomic ensemble.

spontaneous emission from individual atoms or ions [161, 162] and the latter can be used to coherently manipulate the phase of stored optical photons [46, 70, 90], two-level atoms are not suited to mediate single photon non-linearities on their own due to linear absorption on resonance. As discussed above this behaviour changes substantially by introducing a coherently coupling between the excited to a third atomic state giving rise to EIT and providing control over the atom-light interaction, optical response, and photon propagation inside the atomic medium [32]. The brief discussion of atom-light interactions, EIT, and the optical response in a three-level ladder system in this and the following section follow in part the thesis of J. Pritchard [104] which provides a more detailed discussion, and work of Gea-Banacloche *et al.* [159], and Fleischhauer *et al.* [32].

The three atomic states are arranged in a ladder configuration [33, 68, 159] as in figure 2.2: a ground state $|g\rangle$, an intermediate, low-lying excited state $|e\rangle$, and a Rydberg state $|r\rangle$. The ground and Rydberg states are

dipole coupled to the intermediate state with transition frequencies ω_{ge} and ω_{er}, respectively. A signal light field with frequency ω_S detuning $\Delta_S = \omega_S - \omega_{ge}$, and Rabi frequency Ω_S couples $|g\rangle$ and $|e\rangle$ while a control field with frequency ω_C, detuning $\Delta_C = \omega_C - \omega_{er}$, and Rabi frequency Ω_C couples $|e\rangle$ and $|r\rangle$. The fields are named according to their role. The signal light – or photons – are to be made to interact and represent potential carriers of classical or quantum information whereas the control field will be used to control their propagation.[3]

The interaction of the three-level atoms with the signal and control fields is described by the interaction Hamiltonian [32, 104]

$$H_3 = \hbar \begin{pmatrix} 0 & \Omega_S/2 & 0 \\ \Omega_S/2 & -\Delta_S & \Omega_C/2 \\ 0 & \Omega_C/2 & -\Delta_S - \Delta_C \end{pmatrix} \tag{2.11}$$

where the states correspond to basis vectors $|g\rangle \equiv (1,0,0)^T$, $|e\rangle \equiv (0,1,0)^T$, and $|r\rangle \equiv (0,0,1)^T$. The density matrix ρ of the system evolves according to the optical Bloch equation [32, 104]

$$\frac{\mathrm{d}\rho}{\mathrm{d}t} = \frac{i}{\hbar}[\rho, H_3] + \mathcal{L}_3 \tag{2.12}$$

where the von Neumann equation is supplemented by the non-unitary Lindblad operator

$$\mathcal{L}_3 = -\frac{1}{2} \begin{pmatrix} -2\Gamma_e\rho_{ee} & (\Gamma_e + 2\gamma_S)\rho_{ge} & (\Gamma_r + 2\gamma_{rel})\rho_{gr} \\ (\Gamma_e + 2\gamma_S)\rho_{eg} & 2\Gamma_e\rho_{ee} - 2\Gamma_r\rho_{rr} & (\Gamma_e + \Gamma_r + 2\gamma_C)\rho_{er} \\ (\Gamma_r + 2\gamma_{rel})\rho_{rg} & (\Gamma_e + \Gamma_r + 2\gamma_C)\rho_{re} & 2\Gamma_r\rho_{rr} \end{pmatrix} \tag{2.13}$$

which accounts for decoherence induced by decay due to finite state lifetimes Γ_e and Γ_r, choosing $\Gamma_g = 0$ as $|g\rangle$ is a ground state, and dephasing

[3] In literature, e.g. [32], the fields are more commonly referred to as probe (signal) and coupling (control), i.e. outside the context of optical QIP.

induced by the finite laser linewidths γ_S, γ_C, and the two-photon transition linewidth γ_{rel}.

2.2.2 Optical response

While the solutions for diagonal elements of the density matrix ρ_{gg}, ρ_{ee}, and ρ_{rr} describe the population of the individual states, we are interested in the coherence ρ_{eg} between $|g\rangle$ and $|e\rangle$ to determine the complex susceptibility $\chi(\Delta_S)$ and optical response of the signal transition in the three-level medium. The steady state solution in the weak probe (or signal) regime, $\Omega_S \ll \Omega_C, \Gamma_e$ and $\rho_{gg} \approx 1$, can be obtained as [32, 104, 159]

$$\rho_{eg} = -\frac{i\Omega_S/2}{\gamma_e - i\Delta_S + \frac{\Omega_C^2/4}{\gamma_r - i(\Delta_S + \Delta_C)}}. \tag{2.14}$$

Here, the decay rates in $\mathcal{L}_3$ have been combined to $\gamma_e = \Gamma_e/2 + \gamma_S$ and $\gamma_r = \Gamma_r/2 + \gamma_{rel}$.

The complex susceptibility for the signal field detuned by Δ_S in a three-level medium is then given by [32, 104, 159]

$$\begin{aligned} \chi(\Delta_S) &= -\frac{2\rho_{at} d_{eg}^2}{\epsilon_0 \hbar \Omega_S} \rho_{eg} \\ &= \frac{i\rho_{at} d_{eg}^2/\epsilon_0 \hbar}{\gamma_e - i\Delta_S + \frac{\Omega_C^2/4}{\gamma_r/2 - i(\Delta_S + \Delta_C)}} \end{aligned} \tag{2.15}$$

where d_{eg} is the signal transition dipole moment and ρ_{at} the atomic number density. The real and imaginary parts of $\chi(\Delta_S)$ determine the medium's optical response [32, 104, 163], i.e. the transmission

$$T = \exp\left(-k_S z \operatorname{Im} \chi(\Delta_S)\right) \tag{2.16}$$

and phase shift

$$\Delta\phi = k_S z/2 \cdot \operatorname{Re} \chi(\Delta_S) \tag{2.17}$$

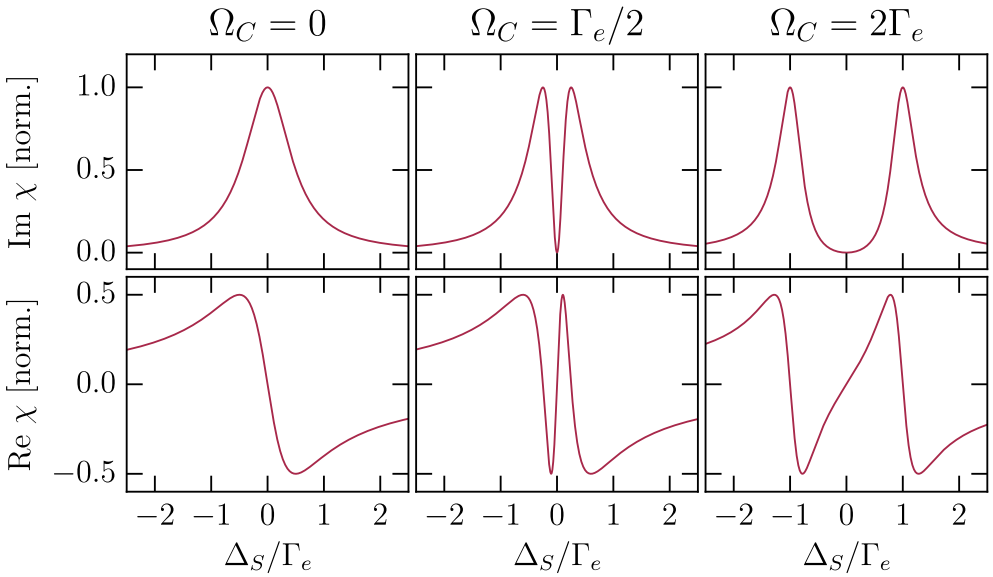

Figure 2.3: Optical susceptibility of a three-level EIT medium. The upper panels show the imaginary part of the susceptibility which defines transmission, the lower the real part which defines the dispersion, setting $\Delta_C = \Gamma_r = \gamma_S = \gamma_C = \gamma_{rel} = 0$. For $\Omega_C = 0$, the system is equivalent to the two-level case and the signal light is strongly absorbed on resonance. For $\Omega_C = \Gamma_e/2$ a narrow transparency window occurs at $\Delta_S = 0$ accompanied by a steep gradient in the dispersion which gives rise to the slow light effect [34]. For $\Omega_C = 2\Gamma_e$, Autler-Townes splitting [164] occurs as the splitting exceeds the linewidth of the signal transition. All susceptibilities are normalised to the imaginary part of the two-level susceptibility on resonance.

of the signal light (treated as plane wave with wave vector k_S propagating in z-direction).

2.2.3 EIT, dark states, and slow light

Figure 2.3 shows the change in both the real and imaginary part of the complex susceptibility for the signal light, and thus in its transmission and phase, with the control Rabi frequency. For $\Omega_C = 0$, the system reverts to a two-level system and resonant signal light is scattered by the atoms. For

$\Omega_C = \Gamma_e/2$ a narrow transparency window occurs around resonance. If the control Rabi frequency is increased beyond the linewidth of the signal transition, $\Omega_C > \Gamma_e$, the absorption line splits into two distinct lines which are separated by Ω_C. This effect is known as Autler-Townes splitting [164].

The emergence of a transparency window around the resonance frequency ω_{eg} in presence of the control field coupling to $|r\rangle$ can be understood when considering the 'dressed' eigenstates of H_3 for $\Delta_S + \Delta_C = 0$ [32, 104]

$$|+\rangle = \sin\theta \sin\phi\, |g\rangle + \cos\phi\, |e\rangle + \cos\theta \sin\phi\, |r\rangle\,, \tag{2.18}$$

$$|D\rangle = \cos\theta\, |g\rangle - \sin\theta\, |r\rangle\,, \tag{2.19}$$

$$|-\rangle = \sin\theta \cos\phi\, |g\rangle - \sin\phi\, |e\rangle + \cos\theta \cos\phi\, |r\rangle \tag{2.20}$$

with energy eigenvalues $E_D = 0$ and

$$E_\pm = \frac{\hbar}{2}\left(\Delta_S \pm \sqrt{\Delta_S^2 + \Omega_S^2 + \Omega_C^2}\right). \tag{2.21}$$

The admixture of the 'bare' atomic states depends on the properties of the signal and coupling fields and is described by the mixing angles [32, 104]

$$\theta = \arctan\frac{\Omega_S}{\Omega_C}, \tag{2.22}$$

$$\phi = \frac{1}{2}\arctan\frac{\sqrt{\Omega_S^2 + \Omega_C^2}}{\Delta_S}. \tag{2.23}$$

For a weak and resonant signal field ($\Delta_S = 0$, weak probe limit: $\Omega_S \ll \Omega_C, \Gamma_S$) the eigenstates are [32, 104]

$$|\pm\rangle = \frac{1}{\sqrt{2}}\left(|r\rangle \pm |e\rangle\right), \tag{2.24}$$

$$|D\rangle = |g\rangle\,. \tag{2.25}$$

Here, the zero-energy eigenstate or dark state $|D\rangle$ is equivalent to the atomic ground state which implies that atoms cannot be excited. The signal field can only couple to the $|e\rangle$-components of $|\pm\rangle$. Due to the

opposite signs of the probability amplitude of $|e\rangle$, the two excitation pathways interfere destructively [32] such that absorption of signal photons is suppressed, giving rise to EIT.

Obviously, the modified susceptibility in the presence of the control field affects not only the transmission but also the dispersion of the signal light [32] (figure 2.3). The real part of the susceptibility exhibits a steep, positive gradient around resonance. Accordingly, the signal group velocity

$$v_g = \frac{\mathrm{d}\omega_S}{\mathrm{d}k_S} = \frac{c}{\tilde{n}(\omega_S) + \omega_S \frac{\mathrm{d}\tilde{n}}{\mathrm{d}\omega_S}} \approx \frac{c}{\tilde{n}_g} \tag{2.26}$$

is reduced [165–167] as the group index

$$\tilde{n}_g = \frac{6\pi\rho_{at}c}{k_S^2} \frac{\gamma_e}{\Omega_C^2 + \gamma_r\gamma_e/4} \tag{2.27}$$

increases. Here, $\tilde{n} = \sqrt{1+\chi} \approx 1 + (\mathrm{Re}\,\chi + i\,\mathrm{Im}\,\chi)/2$ is the refracive index of the medium [32, 104]. The dependence of $\tilde{n}_g$ on Ω_C implies that v_g can be controlled via the intensity of the control field. Besides Ω_C, $\tilde{n}_g$ also depends on the atomic number density ρ_{at} which is related to the optical depth $OD = -\ln T$.

For sufficiently weak Ω_C and optically thick media, signal group velocities reduced by factors of several 10^7 can be observed, e.g. 17 m/s in a Bose-Einstein condensate (BEC) [34], similarly in elongated atomic vapour cells [168, 169]. By adiabatically reducing Ω_C to zero, this slow light phenomenon can also be used to bring a light pulses to a halt and store photons as atomic spin waves [38, 39, 170, 171]. This constitutes a fundamental tool for the work throughout this thesis to convert photons into strongly interacting collective Rydberg excitations [45, 46] (section 2.3 below).

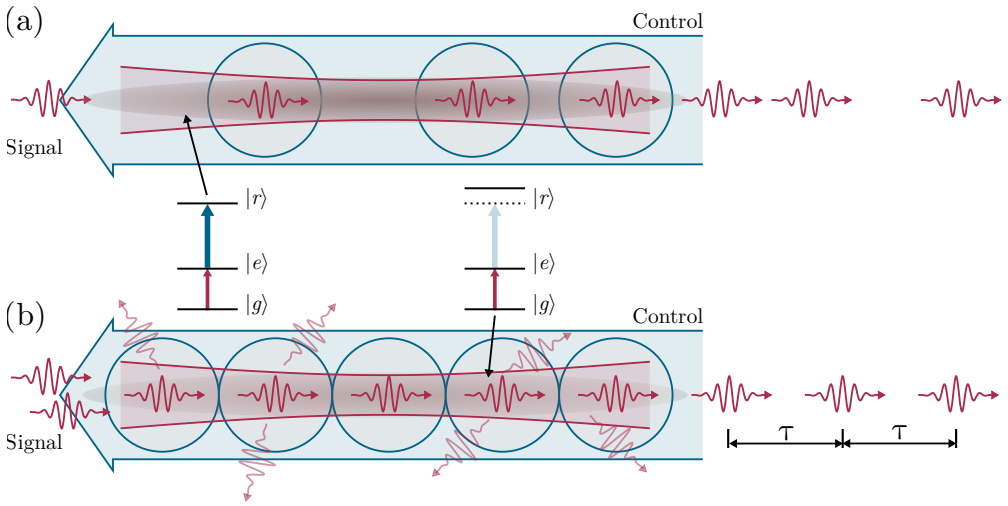

Figure 2.4: Effect of Rydberg interactions on EIT. (a) If the incoming rate of signal photons is low, photons are unlikely to propagate close to each other within the range of the dipole blockade indicated by the blue circles, such that the medium remains transparent for them. (b) At high incoming photon rates, the spatial separation decreases and photons are scattered in the blockaded volumes where the transparent three-level medium reverts to an opaque two-level system. This results in anti-bunching of the transmitted light.

2.2.4 Effect of Rydberg interactions

So far, the discussion of EIT did not consider the effect of dipolar interactions between Rydberg atoms [18, 19] which can shift the energy (section 2.1.1) of $|r\rangle$ effectively inducing a control detuning $\Delta_C = V(\vec{r})/\hbar$ and alter the optical response of the three-level medium [28]. The first optical non-linearities mediated by VdW interactions were observed in Durham by Pritchard *et al.* [26] who observed a signal-intensity dependent suppression of EIT as a result of Rydberg blockade [20, 21] (section 2.1.2). The effect of blockade on Rydberg EIT is simple and illustrated in figure 2.4: A single resonant signal photon propagating through the three-level medium involving a Rydberg state $|r\rangle$ sees the usual transparent medium. If however a photon enters a volume already occupied by another, $|r\rangle$ is shifted resulting in a two-level medium where one of them is scattered

provided the optical depth inside the blockaded volume OD_b is sufficiently high [42–44, 172]. The associated blockade radius is (assuming Ω_C is substantially larger than Ω_S)

$$r_{b,EIT}^{(6)} = \sqrt[6]{\frac{C_6}{2\hbar\Delta_{EIT}}} \tag{2.28}$$

and determined by the EIT linewidth $\Delta_{EIT} = \Omega_C^2/4\gamma_e$ [28, 122].

Using an elongated, quasi one-dimensional medium with higher density and thus increased optical depth, OD_b, and scattering rates, Peyronel *et al.* [40] subsequently observed non-linear behaviour at the single photon level leading to strong anti-bunching in the transmitted photon statistics as the spatial separation $r_{b,EIT}^{(6)}$ translates into a constant time delay between photons, see figure 2.4 (b). Due to the binary nature of dipole blockade [20, 21], the resulting effect resembles 'photon blockade' which can be observed in CQED [9, 12, 14]: In the Jaynes-Cummings model [173], a single atom trapped in a cavity breaks the harmonicity of the eigenstates such that a photon entering an empty cavity containing an atom shifts it off resonance for all subsequent photons in a monochromatic light pulse [14].

Besides dissipative, one can also realise strong dispersive non-linearities by detuning the signal and control fields off resonance ($\Delta_S \approx \Delta_C$) [53, 54]. Measuring both the phase and counting statistics of the transmitted signal photons, Firstenberg *et al.* [54] were able to observe dispersive non-linearities at the single photon-level. The blockade effect can also be reversed if detunings are chosen such that a signal photon shifts an initially detuned control field back on resonance thus realising a single photon absorber if the atomic medium is small enough to be blockaded by a single excitation [61, 174].

2.3 Photon storage

In addition to the ability to map Rydberg interactions onto propagating light fields, EIT [32] also allows to control the propagation of signal

photons as the signal group velocity depends on Ω_C. The most dramatic consequence becomes apparent when considering the group index $\tilde{n}_g$ as given by equation 2.26: In the limit $\Omega_C \to 0$, $\tilde{n}_g$ becomes extremely large (or even infinite in the ideal case $\gamma_r = 0$) practically reducing the group velocity of a signal pulse to zero and storing the photons as stationary collective Rydberg excitations (or spin-waves) [38, 45, 46]. While stored, the photons exhibit the same strong interactions as Rydberg atoms and can be retrieved again by restoring Ω_C .

There are several situations in which interactions between stored photons may be advantageous over propagating photons. For example, nonlinearities between propagating photons [40, 54] require a medium which is sufficiently long and optically thick to ensure that photons are scattered. Instead, in combination with blockade [20, 21], storage allows to isolate a few or even individual signal photons and release them at a later time after the original pulse has been transmitted [45, 46]. In addition, the retrieval modes of stored photons are sensitive to interaction-induced phase shifts between the individual atoms that contribute to the spin-wave [170, 175–177]. This allows weaker interactions beyond the range of dipole blockade to affect the retrieval if multiple photons are stored as multiple excitations [45, 46, 49, 50]. Since the phase-shifts increase over time, storage can enhance the effect of Rydberg mediated photon interactions by increasing the storage and thus interaction time [45, 88, 89]. However, the sensitivity of the photon retrieval to phase shifts also represents a disadvantage, e.g. due to dephasing caused by atomic motion [177] as will be discussed below.

2.3.1 Dark-state polaritons and storage protocol

A convenient formalism to understand the propagation of photons in a EIT medium as well as photon storage and retrieval, are dark-state polaritons [38, 170]: bosonic quasiparticles forming a superposition of the quantised signal field $\mathcal{E}_S(z,t)$ (which was treated as a classical field before) and

the coherence $\rho_{rg}(z,t)$ between states $|g\rangle$ and $|r\rangle$.[4] In one dimension, a polariton propagating in z-direction is represented by the quantum field operator (in the Heisenberg picture) [32]

$$\Psi_D(z,t) = \cos\theta\mathcal{E}_S(z,t) - \sin\theta\sqrt{\mathcal{N}}\rho_{gr}(z,t)\exp\left(i(k_S+k_C)z\right) \tag{2.29}$$

treating both signal and control fields as plane waves with wavevectors k_S and k_C. The mixing angle θ determines the admixture between the light and matter components [38]

$$\begin{aligned}\cos\theta &= \frac{\Omega_C}{\sqrt{\Omega_C^2 + g_S^2\mathcal{N}}},\\ \sin\theta &= \frac{g_S\sqrt{\mathcal{N}}}{\sqrt{\Omega_C^2 + g_S^2\mathcal{N}}},\end{aligned} \tag{2.30}$$

where $g_S = d_{ge}\sqrt{\omega_S/2\hbar\epsilon_0\tilde{V}}$ describes the atom-field coupling, d_{eg} is the dipole moment of the signal transition, and $\tilde{V}$ the quantisation volume containing $\mathcal{N}$ atoms.

The dependence of the admixture on Ω_C is related to the admixture of $|g\rangle$ and $|e\rangle$ in the dark-state $|D\rangle$ (equation 2.19). The atomic coherence ρ_{gr} represents a direct coupling between $|g\rangle$ and $|r\rangle$ and no population is created in $|e\rangle$ as the polariton $\Psi_D(z,t)$ propagates through an ensemble of ground state atoms. This is the origin of the name 'dark-state polariton' [38].

The polariton's group velocity is given by $v_g = c\cos^2\theta$ [38]. For $\theta \to 0$, the polariton's character is dominated by the photonic component and $v_g \to c$, whereas for $\theta \to \pi/2$ the polariton is matter-like and $v_g \to 0$. In principle, both the shape and quantum state of the photonic field are preserved during propagation [38]. As a result, the ability to control v_g between 0 and c by adjusting Ω_C enables storage of photons as collective atomic excitations, or spin-wave as the atomic part is commonly referred

[4] The original work [38] considers a lambda-scheme between two ground states.

to.

Storage protocol

In practice, signal photons can be stored as collective Rydberg excitations as follows. While they propagate through an atom cloud, their group velocity v_g is adjusted by changing Ω_C. (Ideally) adiabatic reduction of Ω_C and thus v_g to zero converts the photonic component into atomic excitation thereby creating a collective excitation in $|r\rangle$ via adiabatic transfer [38, 178].

The excitation corresponds to the collective state $|R\rangle$ as introduced in equation 2.10, and preserves shape and coherence of the photon which are imprinted in the phase and amplitude of the spin-wave [38]. If both signal photons and control field are considered as one-dimensional plane waves, $\phi(\vec{r_j}) = (k_S + k_C)z$ and $\epsilon(\vec{r_j}) = 1$. In order to retrieve the stored photons, the process can be reversed by adiabatically restoring Ω_C to its original value [38]. Upon reintroducing its photonic component, the polariton resumes propagation in its original direction, i.e. in the optical mode of the signal field. It is fully converted back into light once it exits the EIT medium.

The short-lived intermediate state $|e\rangle$ is not populated if the transfer is fully adiabatic [178] such that spontaneous emission and thus a major decoherence channel is closed [38, 170]. In practice this requires a spectral linewidth of the signal photons below the EIT width, $\gamma_S < \Delta_{EIT}$, and poses a lower limit for the signal pulse duration t_S due to Fourier broadening. Another important factor with respect to efficiency is the compression of the pulse inside the medium [170, 175, 176]. Upon entry into the atomic ensemble, a signal pulse is compressed by c/v_g. To achieve maximal storage efficiency, the entire pulse has to be contained inside the medium when Ω_C is reduced to zero imposing a minimal length $l > v_g t_S$ [170, 175]. Therefore, either the group velocity needs to be low, or the medium sufficiently long. In this work, the length of the medium is restricted as localisation of the stored photons comparable to the interaction-range between Rydberg

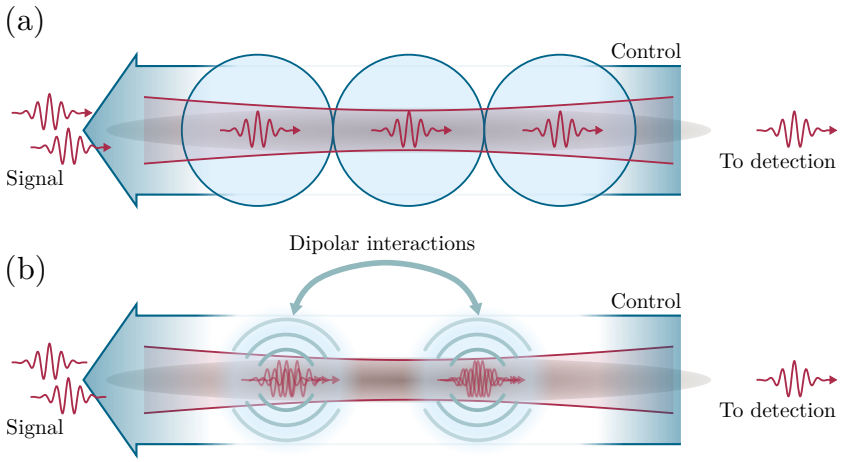

Figure 2.5: Effect of Rydberg blockade and interaction-induced dephasing on photon storage. (a) Excitation blockade limits the number of photons that can be stored as stationary collective Rydberg excitations within the blockade volume indicated by the blue circle to one. (b) Dipolar interactions imprint non-uniform phase shifts in the stationary collective excitations which lead to reduced photon retrieval in the original signal modes.

atoms is required.

The first demonstrations of light storage were achieved in an elongated atomic vapour cell [171] and a BEC [39]. The highest storage-and-retrieval efficiencies, exceeding 96% were so far achieved in a large MOT with $OD > 1000$ [179, 180], while the efficiency record for storage involving Rydberg states stands at $\approx 20\%$ [59].

2.3.2 Effect of Rydberg blockade

Combining photon storage with Rydberg blockade represents another way to observe optical non-linearities at the single photon level [45, 46]. The potential to use stationary collective Rydberg excitations and blockade to realise single-photon sources [155, 157] was pointed out already soon after the original proposal to use blockade for quantum gates [20] which also

mentioned the possibility to exploit blockade to create non-classical states of light. The effect of Rydberg blockade on photon storage is illustrated in figure 2.5 (a) and analogous to blockade between Rydberg atoms in general [22, 23, 52]: Blockade limits the number of collective excitations that can be created per volume [20, 21] leading to saturation of the storage medium if photon numbers are sufficiently high [88, 89]. If the excitation volume defined by the medium and optical modes of the EIT fields is comparable to the volume blockades by a single excitation, only a few or even a single photon can be stored and the retrieved light is highly non-classical [45, 46].

Before the reduction of $\Omega_C \to 0$ as required for the storage process [38], the volume blockaded by a photon stored as a Rydberg spin wave is equivalent to $r^{(6)}_{b,EIT}$ as defined above (equation 2.28) based on the EIT linewidth $\Delta_{EIT} = \Omega_C^2/4\gamma_e$. However, this definition does not longer hold during storage as it would imply that the blockaded volume diverges [122]. Instead, Moos *et al.* [122] discuss that the blockaded volume is determined by the collective Rabi frequency which corresponds to the coupling strength of the signal transition in the limit $\Omega_C \to 0$, and remains similar to $r^{(6)}_{b,EIT}$. In practice, we do not strictly follow the adiabatic reduction of the control field due to limited ability to control the pulse shape (section 3.7.5) and signal pulses and storage times are of order 100 to 400 ns implying that Fourier broadening restricts linewidths to a few MHz.

Interesting applications arise from the combination of storage with Rydberg EIT when storing a gate photon to use the resulting excitation as a binary switch for the optical response of the EIT medium. Using the gate excitation to shift the control field off resonance to create strongly dissipative non-linearities, one can realise single photon switches [55]. If scattering in the blockaded medium is sufficiently high, a single stored photon can suppress transmission of pulses containing multiple photons to implement single photon transistors with 'gain' > 1 [56–58]. Of course, an equivalent change in the optical response can also be created by Rydberg atoms created in other ways, such that these transistors are in concept closely related to optical detection and imaging schemes for Rydberg

excitations [62–64]. In a related fashion, a stored single photon can also be used to switch dispersive optical non-linearities enabling a conditional π-phase shift, representing an important step towards an universal quantum gate based on Rydberg quantum optics [43, 69].

In addition to the storage process itself, blockade may also be exploited in other ways. For example, conditional blockade of microwave rotations caused by longer-ranged resonant dipole interactions (section 2.1.1) could be used to implement an all-optical CZ-gate if the photons were stored sufficiently far from each other such that they do not interact initially cia VdW interactions. Alternatively, photons can be stored using ground state storage in a Λ-scheme with the benefit of longer storage lifetimes and excited to Rydberg states subsequently [181], offering another possibilty to implement phase gates for photonic qubits.

2.3.3 Interaction-induced phase-shifts

Retrieving stored photons in their original optical mode when the control field is restored, relies on imprinting and conserving the phase of the signal photons in the spin-wave. The light field's phase at position $\vec{r}_j$ of an individual atom j is equivalent to the spatially dependent phase factors in $|R\rangle$ (equation 2.10). Non-uniform evolution of the phases, initially given by $\phi(\vec{r}_j)$, during storage alters the retrieved mode, pulse shape, and directionality of the retrieved light [170, 175, 176]. If two or more photons are stored as collective Rydberg excitations for a storage time t_{st}, individual atoms j and k acquire a pairwise interaction-induced phase $V(\vec{r}_j, \vec{r}_k)t_{st}/\hbar$ as illustrated in figure 2.5 (b). While spatially uniform evolution of the phases in $|R\rangle$ leads to a simple phase shift of the retrieved photons, non-uniform phase shifts arising from non-uniform potentials like for VdW and resonant dipole interctions, lead to dephasing and suppress retrieval in the original signal mode [45, 46, 49, 50].[5] Phase shifts induced in $|R\rangle$ by interactions between Rydberg atoms are of fundamental importance as

[5] Imprinting of well-defined phase gradients may lead to a deflected retrieval mode (figure 6.1).

an interaction mechanism between stored photons for the work in this thesis, in particular the demonstration of effective interactions between non-overlapping optical photons stored in side-by-side atomic ensembles [85].

Formal description

Subsequently, we describe the influence of phase shifts induced by Rydberg interactions during photon storage more formally. This discussion – initally limited to storage and interaction within a single medium – will provide the basis for simulations of the effect of interaction-induced phase-shifts on the retrieved photon statistics in chapters 4 and 5 and extends upon work by Bariani *et al.* [50].

Initially, we consider an ensemble[6] A of $\mathcal{N}_A$ atoms which are all in the individual ground state $|g_j\rangle_A$ and denote the individual position of atom j by $\vec{r}_j$. The collective ground state of the ensemble is given by

$$|G\rangle_A = |g_1\rangle_A \otimes \ldots \otimes |g_{\mathcal{N}_A}\rangle_A . \tag{2.31}$$

Storage of a single photon results in the creation of a collective excitation which is shared amongst all atoms in the ensemble. This process can be described by the creation operator [156]

$$S_A^\dagger = \frac{1}{\sqrt{\sum_j \epsilon_A(\vec{r}_j)^2}} \sum_j \epsilon_A(\vec{r}_j)\, e^{i\phi_A(\vec{r}_j)} |r_j\rangle_A \langle g_j|_A \tag{2.32}$$

where $|r_j\rangle_A$ denotes that atom j is in Rydberg state $|r\rangle$, $\epsilon_A(\vec{r}_j)$ is the electric field amplitude of the signal and $\phi_A(\vec{r}_j)$ the combined phase of the signal and control fields. The control field is treated as uniform across the ensemble by omitting its amplitude from equation 2.32. Storage of ν

[6] The index A is irrelevant for the case of a single ensemble and signal mode discussed here and in chapter 4, but is included to avoid a redefinition of notation when describing interactions between two channels A and B in chapter 5.

photons results in the multiply excited collective state [155–158]

$$|R_A^{(\nu)}\rangle = \frac{1}{\sqrt{\nu!}} \left(S_A^\dagger\right)^\nu |G\rangle_A \,. \tag{2.33}$$

Here, we preserve approximately correct normalisation of the collective state if $\nu \ll \mathcal{N}_A$.[7] Furthermore, we do not account for Rydberg blockade which would impose a minimum spacing between and maximum number of collective excitations, since the incoming signal photon numbers are sufficiently low to avoid saturation of the storage in the experiments we model (compare figure 4.7). This simplified description also neglects interaction and propagation dynamics during the storage process.

Interactions during storage

If the pairwise interaction between two atoms j and k contributing to $|R_A^{(\nu)}\rangle$ is described by $V_{jk} = V(\vec{r}_j, \vec{r}_k)$, the time evolution of $|R_A^{(\nu)}\rangle$ during t_{st} is described by

$$U_A\left(t_{st}\right) = \sum_{j,k>j} e^{-iV_{jk}t_{st}/\hbar} \left|r_j\right\rangle_A \left\langle r_j\right|_A \otimes \left|r_k\right\rangle_A \left\langle r_k\right|_A. \tag{2.34}$$

Here, all photons are stored in the same Rydberg state $|r\rangle$ such that they interact via VdW interactions and

$$V_{jk} = V\left(\vec{r}_j, \vec{r}_k\right) = \frac{C_6}{|\vec{r}_j - \vec{r}_k|^6} \tag{2.35}$$

(section 2.1.1). Obviously, each atom pair acquires a different phase $V_{jk}t_{st}/\hbar$ due to spatial variation of V_{jk} which leads to dephasing and a reduced probability to retrieve the stored signal photons in their original mode from the time-evolved collective state

$$|R_A^{(\nu)}\left(t_{st}\right)\rangle = U_A\left(t_{st}\right)|R_A^{(\nu)}\rangle \,. \tag{2.36}$$

[7] In this limit, the collective state is also referred to as quasi-bosonic spin-wave in literature, see e.g. reference [50].

Here, we only consider dephasing based on the interaction between two or more collective excitations. Phase shifts that are not caused by interactions and independent of ν, i.e. those caused by atomic motion [177] (see below), are ignored since they reduce the probability of retrieval in the original signal mode, but do not affect the retrieved photon statistics.

Description of photon retrieval

The photon retrieval process can be described by reversing the storage process. Hence, retrieval of ν photons in their original mode from $|R\left(t_{st}\right)_A^{(\nu)}\rangle$ corresponds to applying the annihilation operator S_A ν times reverting the ensemble to a collective ground state

$$|G'\left(t_{st}\right)\rangle_A = \left(S_A\right)^\nu |R_A^{(\nu)}\left(t_{st}\right)\rangle \tag{2.37}$$

where the phase relation between the individual atoms has been modified compared the original collective ground state $|G\rangle_A$ as a result of the interaction [155, 157]. The models presented in chapters 4 and 5 will compute the retrieved photon statistics following storage based on the probabilities to retrieve either one or two photons which can be computed from the overlap of $|G'\left(t_{st}\right)\rangle_A$ and $|G\rangle_A$.

2.3.4 Further dephasing mechanisms

Motional dephasing

Due the position dependence of $\phi(\vec{r}_j)$, atomic motion during storage is an important source of phase mismatch [38, 170, 177]. The further an atom moves along the phase grating of the spin-wave, the more dramatic the mismatch. During storage for t_{st}, an atom of mass m in an ensemble with temperature T typically moves by vt_{st} where $v = \sqrt{2k_BT/m}$ is the root mean square thermal velocity of the atoms. Hence, lower ensemble temperatures are desirable. Another important consideration is the period of the spin-wave $\Lambda = 2\pi/(k_S + k_C)$ [177]. Shorter periods entail a larger

phase difference as an atom moves along the imprinted phase grating. Consequently, motional dephasing is less pronounced in ground state storage where signal and control wavelengths are closely matched ($k_S + k_C \approx 0$ for counter-propagating fields) [181] while $\Lambda \approx 1250\,\mathrm{nm}$ for storage in Rydberg states employing signal and control fields with $\lambda_S \approx 780\,\mathrm{nm}$ and $\lambda_C \approx 480\,\mathrm{nm}$ using Rb atoms. Stronger confinement in optical lattices [181–184] helps to suppress motional dephasing. The current time record for atom-based photon storage stands at 16 s [185]. These timescales are impossible to achieve with Rydberg states due to their finite lifetimes.

Density-induced dephasing

Besides the positively charged core of a Rydberg atom, the highly excited valence electron may also interact with ground state atoms if they are found inside the electron orbital [186]. This situation occurs if either the atom density or the principal quantum number n, and thus the electron's orbital, are large. The electron-atom interaction is described by a contact potential with negative scattering length such that the Rydberg electron wavefunction forms an attractive potential for ground state atoms [187]. The thermal energy of ultracold atoms is sufficiently low to create bound states and exotic types of molecules [187] which can observed as a separate spectral line below respective Rydberg transition [188]. While the separation is on the order of several MHz and exceeds the EIT linewidth Δ_{EIT} for low lying Rydberg states, the binding energy reduces as n is increased and electron orbitals becomes larger. Hence, additional resonances appear at multiples of the binding energy corresponding to molecules containing multiple ground state atoms [189]. At high n the binding energy is low enough that atomic and molecular lines overlap leading to asymmetric broadening and a red-shift of the atomic resonance [189, 190]. The magnitude of the shift increases with the probability to find ground-state atoms inside the electron orbital [189].

For typical atomic densities in Rydberg quantum optics experiments, on the order of $10^{12}/\mathrm{cm}^3$, the molecular and atomic lines merge around $n = 80$

where on average one ground state atom is found within the electron orbit [189]. The line shift and broadening of the EIT resonance enhance the dephasing-rate of stored photons which increases linearly with the atomic density [55, 191]. The electron-atom interaction also leads to reduced lifetimes of Rydberg states [28, 192].

3 Experimental setup

In order to exploit the strong interactions between ultra-cold Rydberg atoms [18, 19] for quantum non-linear optics experiments, a range of requirements have to be fulfilled. Some are shared with most other ultra-cold atom experiments, while others extend beyond standard requirements. This chapter describes the design, implementation, and characterisation of a new experimental setup dedicated to Rydberg quantum optics [27, 28].

Besides the usual prerequisites such as ultra-high vacuum (UHV) conditions, various magnetic-fields, light for laser cooling and trapping, or imaging systems for diagnostics, the following key requirements had to be met in the design of the setup:

- **Fast cycle times:** Most experiments in quantum non-linear optics [8] require the acquisition of large datasets to analyse photon counting statistics. The timescale of an individual experiment is on the order of µs and short compared to the preparation of cold atomic ensembles. Hence, a main objective is to speed up the preparation and maximise the number of times an ensemble can be recycled for subsequent experiments.

- **High optical resolution:** Addressing and controlling interactions between Rydberg polaritons or stored photons well below the typical interaction range of Rydberg atoms and blockade [20, 21] requires optical resolution close to 1 µm close to the diffraction limit.

- **Microwave fields:** Microwaves drive transitions between Rydberg states and thus represent a powerful tool to introduce and control strong resonant dipole interactions between excitations [46, 47, 49,

90]. Therefore a means to apply microwave fields in a well-controlled manner is desirable.

- **Electric field control:** The sensitivity of Rydberg atoms to DC electric fields [18, 108] requires measures to minimise and compensate stray fields. At the same time, their controlled application allows to tune Rydberg interactions at Förster resonances [58, 127].

To accomodate all of these, a new experimental setup dedicated to Rydberg quantum optics [28, 29] has been designed and built from scratch thorughout this thesis. Its vacuum chamber (section 3.1) features an in-vacuo assembly (section 3.2) including a pair of high NA aspheric lenses to achieve high optical resolution [93] as well as sets of electrodes, microwave antennae, and anti-Helmholtz coils for the MOT [193]. Alongside the vacuum system, a new laser system (section 3.3) addressing transitions on the ^{87}Rb D2 line for both laser cooling and quantum optics experiments and experimental control (section 3.4) have been set up. A crucial feature to speed up the preparation time of the cold atom ensembles is efficient MOT loading in less than 100 ms from a bright atomic beam generated by a 2D MOT [94] (sections 3.5 and 3.6). Using the in-vacuo lenses, we implement two side-by-side photonic channels (section 3.7) each consisting of a tightly focussed mode for signal photons and an atomic ensemble confined in a microscopic dipole trap [92, 194]. The atoms serve as media for photon storage [45, 46] or Rydberg EIT [26, 33, 40] more generally and can be recycled several 10 000 times to enhance the data acquisition rate. The distance between channels is adjustable at the µm-level. By introducing Rydberg mediated optical non-linearities across channels, the scalable side-by-side geometry paves the way to investigate effective interactions between optical photons in independent, non-overlapping optical modes and media [85] (chapter 5).

The experimental setup presented in this chapter was designed by the author. S. W. Ball and P. Huillery contributed to building, and T. Ilieva maintaining it. All members of the Durham Rydberg quantum optics

group made suggestions on and discussed the design. Work was supervised by C. S. Adams and M. P. A. Jones. K. J. Weatherill, D. Paredes, and D. J. Szwer contributed during the early planning stages.

This chapter is in part based on the following publication [88]:

- H. Busche, S. W. Ball, and P. Huillery, "A high repetition rate experimental setup for quantum non-linear optics with cold Rydberg atoms", Eur. Phys. J. Spec. Top. **225,** 2839–2861 (2016).

3.1 Vacuum system

Maintaining UHV conditions is a fundamental requirement for any cold atom experiment since loss due to collisions with background atoms deteriorates trap lifetimes or prevents trapping altogether. For magneto-optical trapping [193], pressures $\propto 10^{-8}$ mbar or below are required, though $\propto 10^{-11}$ mbar are typically desirable to increase lifetimes to seconds or even minutes and enable evaporative cooling in harmonic traps for the production of degenerate quantum gases [195–197]. To reach the latter, vacuum systems usually are comprised of two separate vacuum regions: a region with high partial pressure of the desired atomic species where atoms can be captured more rapidly and pre-cooled before transfer to a science chamber where experiments take place. Despite relatively relaxed requirements on the background pressure compared to other experiments, a two chamber approach, including a 2D MOT [94] as a switchable high flux cold atomic beam source, was chosen as shown in figure 3.1 to reduce MOT loading times (sections 3.5 and 3.6).

The main science chamber is an octagon[1] made from non-magnetic stainless steel like most other vacuum fittings.[2] It provides access through eight CF40 ports in a plane perpendicular and two CF100 ports parallel to the optical table surface. The 2D MOT is mounted on the top such that the atomic beam propagates downwards along the vertical axis and

[1] Kimball Physics MCF600-SphOct-F2C8.
[2] Mostly grades 316L/LN, otherwise 304.

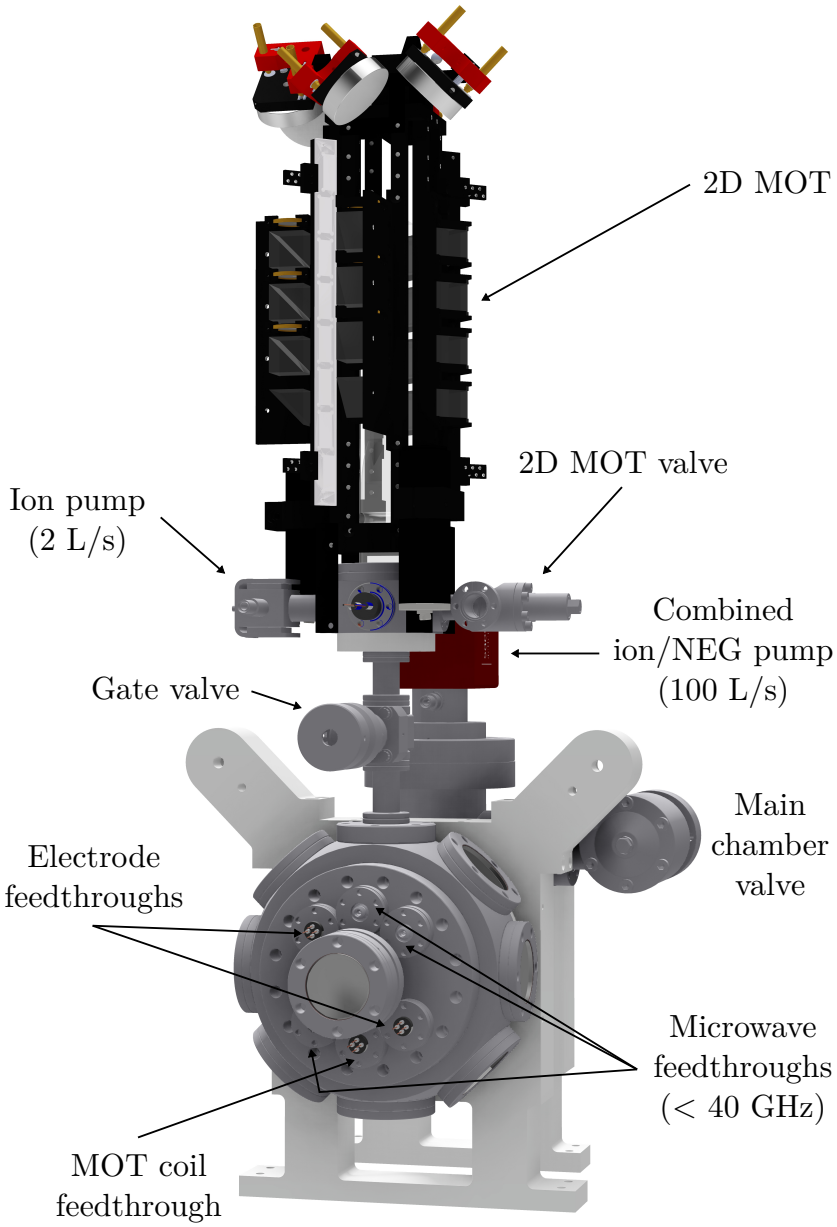

Figure 3.1: Overview of the vacuum system. The main science chamber is on the bottom, below the 2D MOT which is mounted vertically. A gate valve allows separation of both vacuum sections. Various electrical and microwave feedthroughs are attached to a cluster flange. Behind the main chamber a pumping section hosts a combined ion/NEG pump and a valve to connect further pumps during bakeout.

is not deflected by gravity.[3] The two CF40 ports parallel to the table surface provide optical access to the in-vacuo lens pair (section 3.2.1). The corresponding viewports[4] are made from deep-UV fused silica with custom anti-reflection (AR) coatings (wavelengths $450 - 550$ and $750 - 1100\,\mathrm{nm}$) applied to both surfaces and matching the lenses' coatings. An identical viewport is attached to the bottom port opposite the 2D MOT intended for fluorescence imaging or to provide access for low power laser beams which can be safely dumped on the chamber walls. Home-made viewports [198] using AR coated BK7 glass ($700 - 1100\,\mathrm{nm}$) are mounted on the ports at 45° between the lens and 2D MOT axes. These provide access for the radial cooling beams of the MOT. One of the CF100 ports hosts a reducer flange with a CF40 viewport and six additional feedthroughs: A four pin power feedthrough for the MOT coil current, two four pin power feedthroughs for the electrodes, and three coaxial feedthroughs for the microwave antennae (section 3.2). The other CF100 port is used to connect a vacuum pump via CF63 tubing, and also features a CF40 viewport for optical access. Both CF40 viewports are identical to those on the lens axis and provide optical access for the axial MOT beams, absorption imaging, and potentially an additional dipole trap.

UHV is maintained by a combined non-evaporative getter (NEG)/ion pump[5] with a pumping speed of $100\,\mathrm{L/s}$. This pump is significantly more compact than conventional ion pumps of similar speed.[6] A CF40 all-metal valve is used to connect roughing and turbo-molecular pumps during bake-out of the system. Following a bake-out of the entire vacuum system at 160°C for two weeks, the pressure reading of the pump controller is below

[3] The beam pointing is slightly misaligned after the connecting tubing has bent during bake-out, such that part of the beam may not pass through the relatively small capture volume of the MOT and the loading performance is reduced. Consequently, an adjustable bellows would be inserted in a future setup or if a vacuum break became necessary.

[4] MPF A0650-1-CF.

[5] SAES Getters NexTorr D 100-5.

[6] The NEG element acts as a passive pump for the most abundant contaminants and is placed before the ion pump intake which can be significantly smaller due to the reduced load.

its lower limit of 10^{-10} mbar. Unfortunately, we lack a more accurate indication of the pressure since no dedicated ion gauge is attached to the system due to space constraints.

The 2D MOT is realised in a UHV glass-cell (details in section 3.5.1 below). Both chambers are connected via CF16 tubing and a differential pumping tube (length 149 mm, ID 6 mm) with a 0.8 mm aperture. Vacuum can be broken independently in both regions thanks to a CF16 gate valve located between them, as well as a separate ion pump and valve on the 2D MOT.

3.2 In-vacuo assembly

In order to meet the special requirements listed in the introduction of this chapter, it is convenient to mount selected components of the experimental setup inside the vacuum chamber. This is in stark contrast to other experiments where the inside of the vacuum chamber is often kept empty to reduce the in-vacuo surface area and minimise outgassing. Therefore, great care had to be taken in the design and choice of materials for the assembly shown in figure 3.2 and presented subsequently.

Most importantly, high NA aspheric lenses are placed inside the vacuum close to the atom trap region providing optical resolution of $\approx 1\,\mu$m. Eight electrodes to compensate stray and apply well-controlled electric fields are mounted around the lenses. Internal application of electric fields is preferable to external electrodes to avoid polarisation of the viewports [199]. Three microwave antennae are located close to the experimental region significantly reducing the power required to drive transitions between Rydberg states and minimising reflections from metal surfaces such as the chamber walls. Finally, a pair of anti-Helmholtz coils generates the quadrupole magnetic field required for the MOT. Internal coils close to the MOT centre allow generation of strong field gradients at moderate currents without the need for water cooling.

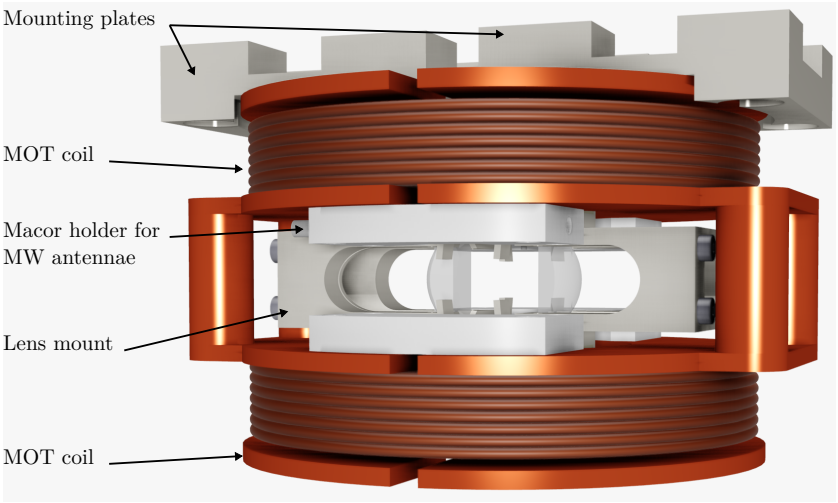

Figure 3.2: Overview of the in-vacuo assembly. High NA lenses and a set of electrodes for electric field control are mounted in a central titantium mount and surrounded by a pair of anti-Helmholtz coils for the MOT. Holders for microwave antennae attach to the coils. The entire assembly is connected to the vacuum chamber (not shown) via a titanium mounting plate.

3.2.1 High numerical aperture lenses

High optical resolution on the order of 1 µm is one of the key requirements for the experimental setup. It allows one to individually address, control storage and propagation of, and Rydberg-mediated interactions between [28, 29] (chapter 2) signal photons in microscopic atomic ensembles confined in tightly focussed optical tweezers [92]. A popular way to achieve sub-µm optical resolution in ultra-cold atom experiments is the use of microscope objectives which allow imaging and addressing of individual atoms in optical lattices with sub-µm spacings [200–202]. This typically requires to trap the atoms close to a vacuum window which can be problematic in the context of Rydberg atoms due to their strong interactions with surfaces [75, 77, 109, 199, 203]. Fortunately, our resolution requirements are somewhat relaxed thanks to the µm length scales of Rydberg interactions [18, 19] and excitation blockade [20, 21] (section 2.1). In our setup, sufficient resolution

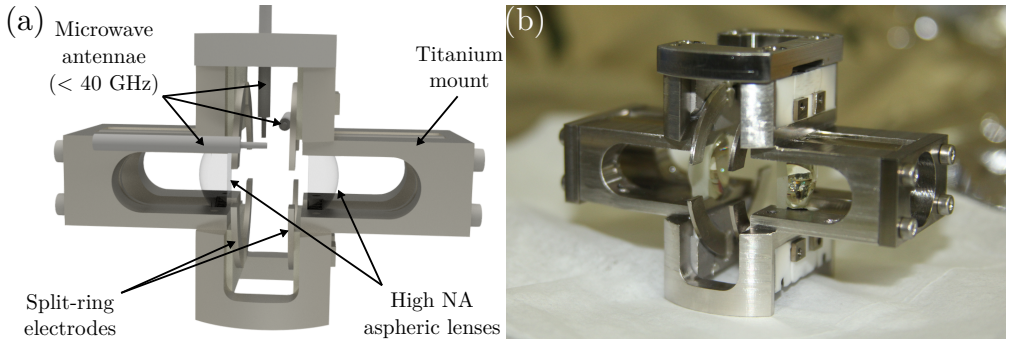

Figure 3.3: Mount for high numerical aperture in-vacuo lenses. (a) Overview of the mount. The two lenses ($f = +10.3\,\mathrm{mm}, \mathrm{NA} \approx 0.5$) are separated by $\approx 14\,\mathrm{mm}$, twice their working distance, and held in place by clamps. Eight electrodes surround the lenses and are clamped into Macor blocks. Three microwave antennae located nearby are made from UHV compatible, open ended semi-rigid coaxial cables. (b) Photograph of the assembled mount. Titanium surfaces coated with platinum for passive electric field control, can be clearly distinguished from darker, uncoated surfaces. Similarly, platinum coated Macor surfaces appear grey instead of white.

of $\lesssim 1\,\mu\mathrm{m}$ is achieved using high NA aspheric lenses mounted inside the main science chamber [93].

The lenses[7] have an effective focal length of $f = +10.3\,\mathrm{mm}$ and a working distance of 7.0 mm. Their clear aperture of 12.5 mm corresponds to a NA of 0.6.[8] As shown in figure 3.3, the lenses are arranged as pair separated by twice their working distance allowing recollimation and imaging of the Rydberg EIT and dipole trap laser beams after focussing (section 3.7). The edges of the lenses are cut[9] at an angle of 30° with respect to the optical axis to provide optical access for the radial MOT beams (figures 3.3 and 3.8). The outer lens surfaces are AR coated for $450 - 550\,\mathrm{nm}$ and $750 - 1100\,\mathrm{nm}$, the surfaces facing the atoms have been coated with

[7] LightPath Technologies 355561.

[8] The lenses were designed by the group of A. Browaeys at the Institute d'Optique, Palaiseau, France who use them (uncut) to holographically generate arbitrary arrays of single atom traps to study Rydberg interactions and many-body dynamics [96, 98, 204, 205].

[9] The lenses have been cut at the Institute d'Optique, Palaiseau, France.

a conductive indium tin oxide (ITO) layer to avoid the build-up of patch charges as Rb atoms are deposited on the lens surface (section 3.2.2). Since index-matching of the ITO coatings to the lenses is impractical due to the required thickness of the layers, transmission through each lens is reduced (measured values $\approx 86\%$ at 780 nm and $\approx 82\%$ at 910 nm).

Focussing a beam of signal light at 780 nm with a $1/e^2$-radius of 3.5 mm we expect a diffraction limited spot size of $\approx 0.9\,\mu$m constrained by the clear aperture of the cut lens. Using a knife-edge placed on a piezo-driven translation stage[10] with nm-resolution, we measure a $1/e^2$-waist radius of $1.0 \pm 0.1\,\mu$m close to the expected value. This value is confirmed when imaging the beam profile in the focal plane onto a camera used to monitor the position of the beams (section 3.7 below).

Lens mount

Figure 3.3 shows an overview (a) and photograph (b) of the assembled lens mount including electrodes for electric field compensation and microwave antennae. The mount has been manufactured from a single block of titanium. Titanium[11] was chosen over stainless steel due to its favourable magnetic properties, lower thermal expansion, and lower outgassing [206].[12] The lenses are mounted in a bore which acts as a 'lens tube' and held in place between facets inside the 'tube' and clamps attaching to the back of the mount. The facets are separated by twice the lenses' working distance. To ensure the optical axes of the lenses coincide, a single bore was initially milled through the entire block (13.0 mm diameter, corresponding to the free aperture). Subsequently, the 'tube' was widened to the full diameter (15.0 mm) of the lenses from each end of the block up to the facets. The mount is extruded around the experimental region defined by the lenses' foci. This reduces the amount of metal and thus reflections of microwave

[10] Physik Instrumente P-611.1S.
[11] Commercially pure Grade 2 titanium.
[12] Since patch charges of adsorbed Rb atoms [75, 77, 203] can build up on dielectric, oxidised titanium surfaces, we would refrain from using titanium again.

fields (section 3.2.3) and provides sufficient space to mount electrodes (section 3.2.2).

The distance between the lenses has been optimised such that signal light at a wavelength of 780 nm is recollimated by the second lens. The correct distance was determined using simplified test mounts before manufacture of the final mount to avoid imprecisions due to repeated re-machining. During final assembly, the beam profile and diameter were monitored over several meters behind the lens pair to ensure collimation and avoid aberrations. Following bake-out of the vacuum system, coupling efficiencies into polarisation-maintaining (PM) single mode fibres for signal beams are well above 80% after focussing to $1/e^2$-radii of 1 µm and recollimation. Since the distance between the lenses has been optimised at a wavelength of 780 nm, the divergence of the dipole trap and EIT control beams need to carefully adjusted to co-locate their foci with the signal light (section 3.7.1).

3.2.2 Electric field control

While the high polarisability of Rydberg atoms [18, 19] is a virtue which gives rise to their strong interactions, high sensitivity to external electric fields and a plenthora of applications in metrology [108–112, 199, 207], it also represents a curse as careful electric field control is needed to shield and compensate stray fields as well as to allow tuning of interactions, in particular at Förster resonances [58, 127]. In practice, two approaches can be distinguished: Passive measures aim at preventing the build up of background fields in the first place while electrodes allow active control of electric fields.

Passive electric field control

A major source of stray electric fields are patch charges of atoms deposited onto non-conducting or ungrounded surfaces [75–77, 109, 208, 209]. Dielectric surfaces in direct line of sight of the atoms are particularly prob-

lematic as new Rb atoms are consistently deposited and create potentials which can vary over typical time scales of experimental runs. Avoiding non-conductive surfaces or placing them far from the experimental region therefore represents a prime design objective. Unfortunately, it cannot be entirely complied with in our setup due to the working distance of the lenses (7 mm). Also, the electrodes are mounted in Macor blocks (see below) for insulation purposes. A viable approach to avoid the build up of patch charges nonetheless, is to apply conductive coatings to all critical surfaces.

The flat surfaces of the aspheric lenses facing the atoms are coated with a ITO layer (sheet resistance 150 Ω/sq, see above). The coated surfaces are grounded as their edge rests directly on the grounded lens mount. The Macor surfaces of the electrode mounts are coated with a 50 nm platinum layer.[13] Before applying the platinum layer, a few nm of chromium was applied since a direct VdW bond between Macor and platinum is very fragile [210]. To ground the coated surfaces, electrically conducting epoxy[14] connects the different blocks of the holder to the grounded lens mount. Even though the electrodes are not directly resting on the Macor, the surfaces underneath are left uncoated to avoid accidental grounding.

Besides the obvious dielectric surfaces discussed above, the surfaces of the titanium components in the atoms vicinity are also troublesome with respect to electric field control as titanium oxidises almost immediately upon contact with air forming thin dielectric patches on the surface. Hence, the deposition of Rb atoms leads to the creation of patch charges in the same manner as on intrinsic dielectrics. Consequently, all titanium surfaces in the atoms' vicinity are also coated with a 50 nm platinum layer.

[13] All platinum coatings have been applied by A. Hindmarch from the Centre for Materials Physics at Durham.
[14] Epotek H21D.

Active electric field control

Well defined electric fields can be applied by eight individually controllable electrodes incorporated into the lens mount assembly as shown in figure 3.3. They are arranged in two rings centred around the lens axis, each segmented into four separate electrodes. This geometry has proven popular in numerous other setups as it allows to apply fields along all three spatial directions, and arbitrary superpositions thereof [101, 211]. The geometry in our setup however differs slightly in two respects. Firstly, the gaps between segments are rather wide at 6.0 mm to maintain good optical access. Secondly, the difference between the inner and outer ring diameters of 12.5 mm and 16.5 mm, respectively is small resulting in a reduced surface area such that the electrode plates are less likely to reflect or form a cavity for microwave fields. These advantages outweigh the disadvantages of a lower field homogeneity and reduced field strength.

The electrodes are made of titanium and are clamped into Macor blocks to insulate them from the remaining metal parts of the in-vacuo assembly (figure 3.3). The blocks attach to the lens mount and clamp around rectangular extrusions extending from the back of each electrode.

3.2.3 Microwave fields

Microwave fields are a convenient tool to drive transitions between adjacent Rydberg states [18, 19] and control dipolar interactions between Rydberg polaritons and stored photons [46, 47, 212–214]. For example, they give access to $|nP_J\rangle$- or $|nF_J\rangle$-states which are inaccessible by two-photon excitation schemes such as two-level EIT [33] due to angular momentum selection rules. Microwaves can be used to introduce resonant dipole interactions (section 2.1.1) by partially transferring Rydberg population to states with orbital angular momentum $\Delta L = \pm 1$. We envision using microwaves and blockade of microwave transitions to apply well-controlled conditional phase shifts to photons stored as Rydberg spin-waves [70] and to study excitation hopping between dipole coupled excitations which is

of great interest for the study of spin-exchange and non-radiative energy transfer [51, 64, 90, 138].

Three microwave antennae are incorporated into the in-vacuum assembly. They are realised as stub antennae made from unterminated UHV compatible, semi-rigid coaxial cable.[15] The cables' shielding and dielectric insulator are removed for the last 4 mm such that the antennae resemble quarter-wave stubs at a frequency of approximately 18.7 GHz. Whilst inefficient, this approach allows to keep the antennae compact and place them close to the experimental region since the microwave field strength is no major concern thanks to the large transition dipole moments between adjacent Rydberg states [18] (section 2.1). This approach also reduces the amount of unwanted reflections from metal surfaces close to the path between the antenna and the experimental region. In total, three antennae (figure 3.3) allow to apply fields with – in principle – linear polarisation parallel and perpendicular to the lens axis, with the potential to superimpose fields to drive $\sigma_{\pm}$-transitions.

The coaxial cable and microwave feedthroughs[16] use SMA-K 2.92 mm feedthroughs and are rated for frequencies of up to 40 GHz which sets a lower limit of $n = 48$ to drive $|nS_{1/2}\rangle \rightarrow |(n-1)P_J\rangle$ transitions. The signal generator[17] used as microwave source is capable of frequencies of up to 65 GHz and allows to switch microwave fields with time resolution of 5 ns (limited by the experimental control system) via a TTL-compatible trigger.

3.2.4 Magnetic field coils

In addition to the high NA lenses, electrodes, and microwave antennae, it is convenient to also integrate a pair of anti-Helmholtz coils into the in-vacuo assembly which generates the magnetic field gradient required for magneto-optical trapping [193]. This avoids the need for water-cooled

[15] Huber+Suhner Sucoflex, supplied by Allectra.
[16] Allectra 242-SMAD40G-C16, custom made.
[17] Anritsu MG3696A.

external coils that operate at higher currents.

The anti-Helmholtz coils surround the lens-mount assembly as shown figure 3.2. They are separated by 25 mm, have an inner radius of 25 mm and each consist of 55 windings of Kapton coated copper wire.[18] The current loops form a rectangular 6×9 array (plus one extra winding around the outside). Using a Hall probe, we measure a field gradient per current of $5.297 \pm 0.009\,(\mathrm{G/cm})/\mathrm{A}$ along the axial direction in good agreement with calculations. To improve heat dissipation, the coil formers are manufactured from oxygen-free high thermal conductivity (OFHC) copper.[19]

The current for the coils is supplied by a DC laboratory power supply[20] and switched and adjusted via its analogue current control input and an analogue output of the experimental control system. Switching times are below 2 ms and limited by the unit's response time.

3.3 780 nm laser system

Any ultracold atom experiment requires laser light stabilised to atomic transitions suitable for laser cooling [91], manipulation, and probing of the atoms. In our experiments, ^{87}Rb atoms are used which have become the workhorse of ultra-cold atomic physics as inexpensive and reliable diode lasers are readily available to drive transitions on the D2-line between the $|5S_{1/2}\rangle$ and $|5P_{3/2}\rangle$ states at 780.24 nm [215]. Figure 3.4 gives an overview of relevant transitions and hyperfine states which are used not only for laser cooling and imaging, but also for signal photons in Rydberg quantum optics [28, 29].

Due to the large hyperfine splitting of the $|5S_{1/2}\rangle$ ground state of

[18] AWG 14, 1.7 mm diameter.

[19] A test using a residual gas analyser following bake-out indicates that noticeable outgassing occurs if the coils run continuously at currents of 9 A and above. During day-to-day operations, vacuum is not affected by short ($\propto 10$ ms every $\propto 100$ ms) pulsing of the current to ≤ 10 A.

[20] Elektro-Automatik EA-PS 3016-20 B.

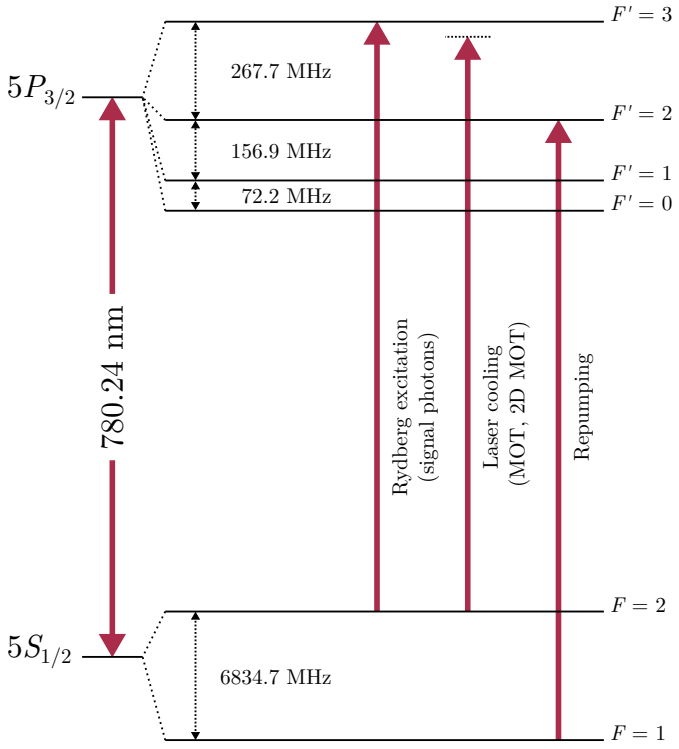

Figure 3.4: Level scheme of ^{87}Rb D2-line and relevant transitions. Laser cooling and repumping for the MOT and 2D MOT occur between the usual $F = 2 \rightarrow F' = 3$ and $F = 1 \rightarrow F' = 2$ transitions. The signal light for Rydberg EIT is usually circularly polarised and thus addresses the closed $F = 2, m_F = \pm 2 \rightarrow F' = 3, m_{F'} = \pm 3$ transition. Data for energy levels taken from D. Steck [215].

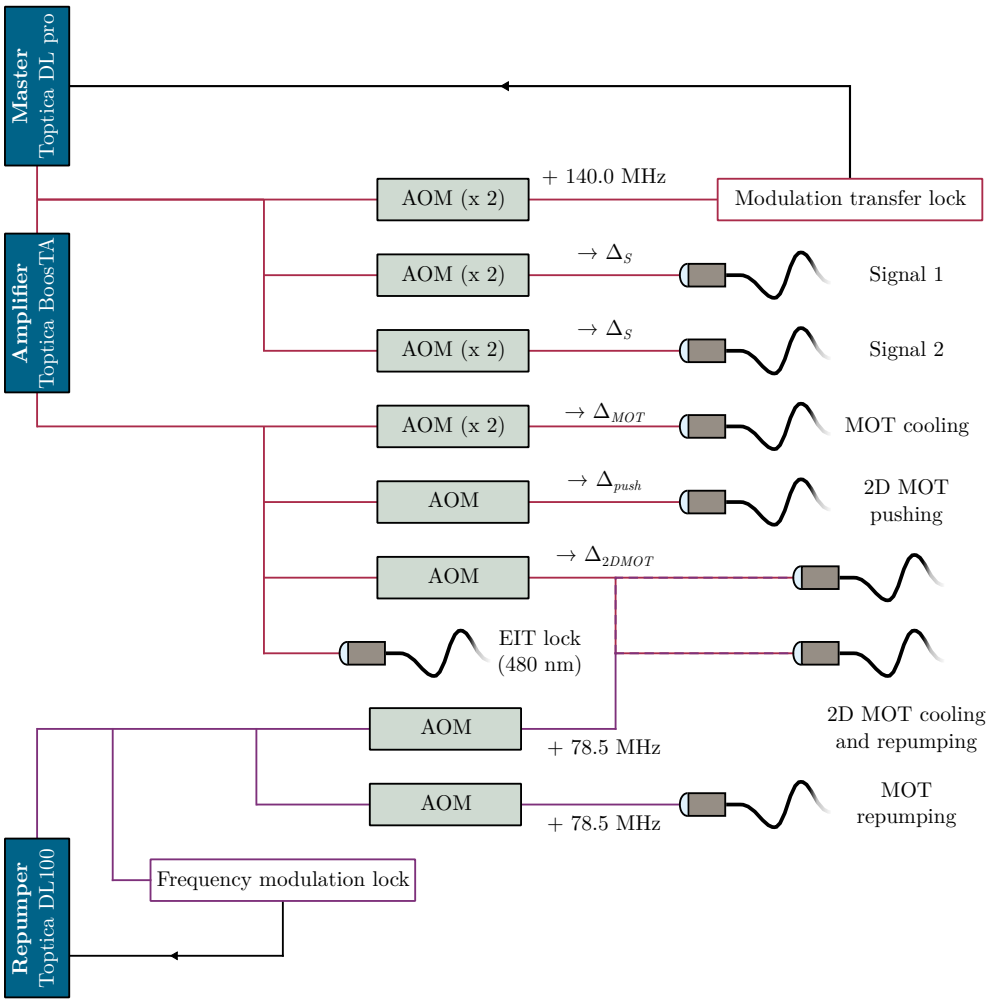

Figure 3.5: Overview of the 780 nm laser system. A master laser is stabilised 140 MHz below the $F = 2 \rightarrow F' = 3$ transistion of the ^{87}Rb D2-line using MT spectroscopy. Signal light for Rydberg EIT and cooling light (amplified by a TA) for the MOT and 2D MOT are shifted to the required detunings using AOMs and transported to the experiment by PM fibres. The corresponding repumping light ($F = 1 \rightarrow F' = 2$) is provided by a separate laser stabilised to a FM spectroscopy signal.

6.8 GHz, two separate lasers are required to provide light for laser cooling, imaging, and signal light on the $|5S_{1/2}, F = 2\rangle \rightarrow |5P_{3/2}, F' = 3\rangle$ and repumping light for the MOT [193] and 2D MOT [94] resonant with the $|5S_{1/2}, F = 1\rangle \rightarrow |5P_{3/2}, F' = 2\rangle$ transition. A simplified schematic of the combined laser systems is shown in figure 3.5.

3.3.1 Master laser

The light required for laser cooling, imaging, and the Rydberg EIT signal on the $|5S_{1/2}, F = 2\rangle \rightarrow |5P_{3/2}, F' = 3\rangle$ transition is provided by a commercial external-cavity diode laser (ECDL) used as a master laser[21] with a typical output power of 80 mW. Approximately 40 mW are used to seed a commercial TA system[22] which provides up to 1.2 W of light for laser cooling. The remaining light emitted by the master laser is used for frequency stabilisation, imaging, and Rydberg quantum optics experiments.

Using half-wave plates (HWPs) and polarising beam splitter (PBS) cubes, this light is split into three branches. The laser is frequency stabilised to an atomic reference generated using modulation transfer (MT) spectroscopy [216, 217] and a fast commercial PID controller[23] to provide feedback to the laser. Before the spectroscopy setup, the light in the first branch is double-passed through an AOM[24] driven at 70 MHz. Hence, locking on resonance in the MT spectroscopy setup shifts the emitted light −140 MHz below resonance such that all other beams in the system can be switched, shifted, and scanned around resonance using either single- or double-passed AOMs. The remaining two branches (signal 1 and 2) both provide signal light detuned by Δ_S for Rydberg EIT. Typically, only weak signal pulses are needed and both beams are tightly focussed through the corresponding AOMs[25] in a double pass configuration to enable fast switching and potentially pulse shaping of the signal light with the rise-/fall-time on the

[21] Toptica DL pro.
[22] Toptica BoosTA.
[23] Toptica FALC110.
[24] Gooch & Housego M080-2B/F-GH1.
[25] Crystal Technology/Gooch & Housego 1080-122.

order of 20 ns. Like all light in the experiment, the signal light is delivered to the experiment via PM optical fibres.

The light used to seed the TA passes a 40 dB optical isolator before the TA unit in addition to another 40 dB isolator placed inside the master laser to protect it from backward emission of the TA chip. At the output of the TA unit which includes a 60 dB optical isolator, up to 1.2 W are available and split into four beams using polarisation optics. The first is double-passed through an AOM[26] to provide cooling light red detuned by Δ_{MOT} for the MOT; the second and third beams are single-passed through AOMs[27] to provide light red detuned by Δ_{push} for the pushing and Δ_{2DMOT} cooling beams of the 2D MOT (section 3.5). The single-passes are not focussed through their respective AOMs as high efficiencies, but no fast switching is required. The cooling light is subsequently overlapped with the 2D MOT repump light and split into two separate beams for each cooling axis of the 2D MOT. Finally, a small amount of light detuned by -140 MHz is split and transferred to the 480 nm laser system to allow frequency stabilisation to an EIT line [218, 219] (section 3.7.5). Again, all light is delivered to its respective destination using PM optical fibres.

3.3.2 Repumping laser

Due to the red-detuning of the cooling light, there is a non-zero probability to off-resonantly excite atoms to the $|5P_{3/2}, F' = 2\rangle$ state such that the cooling transition in a MOT is not perfectly closed and atoms may decay to the lower $|5S_{1/2}, F = 1\rangle$ hyperfine ground state. To keep them in the cooling cycle, they need to be repumped on the $|5S_{1/2}, F = 1\rangle \rightarrow |5P_{3/2}, F' = 2\rangle$ transition [91, 193].

As a consequence of the aforementioned large ground state hyperfine splitting of ^{87}Rb [215], the repumping light has to be supplied by a separate commercial ECDL[28]. Despite its output power below 100 mW, the laser

[26] Crystal Technology/Gooch & Housego 1080-122.
[27] Crystal Technology/Gooch & Housego 1080-125 and 1100-125.
[28] Toptica DL 100.

is protected from back reflections by two 40 dB optical isolators since the 2D MOT repumping and cooling light which is several 100 mW strong, are multiplexed into the same optical fibres (figure 3.5). Behind the isolators, a small fraction of light is branched off to stabilise the laser to the crossover between the $F = 1 \rightarrow F' = 1$ and $F' = 2$ resonances, -78.5 MHz below the repump transition, via frequency modulation (FM) spectroscopy [220] and a fast commercial PID controller.[29] The remaining light is split into two branches for the MOT and 2D MOT. Both are single passed through AOMs[30] to switch and shift them by $+78.5$ MHz onto resonance. Like the cooling light, only the repumping light for the MOT is focussed through the AOM as fast switching is not required for the 2D MOT. Subsequently, the MOT repumping light is directly coupled into a PM optical fibre, while the 2D MOT light is overlapped with the cooling light before transfer to the experiment.

3.4 Experimental control and diagnostics

The preparation of and experiments on cold atomic ensembles require the ability to switch and control various laser beams, magnetic, electric, or radio frequency (RF) fields with a time resolution of just a few µs. In Rydberg quantum optics [28, 29], even better timing resolution of a few ns is required to switch laser pulses on time scales of 10 ns and record photon detection events. This section summarises the experimental control system. The single photon detection setup which is the most important diagnostic tool for experiments in Rydberg quantum optics, will be introduced in conjunction with the implementation of individual 'photon channels' in section 3.7.3.

The various components of the experiment are controlled by a system based on a field-programmable gate array (FPGA).[31] To program the FPGA

[29] Toptica FALC110.
[30] Crystal Technology/Gooch & Housego 3080-125.
[31] National Instruments PCIe 7842R.

for each experiment, we use Durham Experimental Terminal (DExTer), a control software developed locally by T. Wiles [221] in the group of S. Cornish. Before each experimental run, the entire timing sequence programmed in the graphical user interface of DExTer is uploaded to the FPGA which subsequently sends and records control signals to 8 analogue in-, 8 analogue out-, and 96 digital in-/outputs synchronised to its internal clock.

Typical experiments in Rydberg quantum optics happen on timescales much faster than other cold atom experiments, i.e. tens or hundreds of ns. DExTer has hence been substantially modified by D. J. Szwer and S. W. Ball in order to achieve a timing resolution of 5 ns for 16 digital in/-outputs such that no external pulse generators are necessary to control singal and dipole trapping light, and no photon counting module is required to record the time of photon counting events. An arbitrary function generator (AFG) is used for pulse shaping of the control light (section 3.7.5 below) and triggered by one of the fast digital outputs.

The analogue outputs control various laser frequencies and intensities via the corresponding inputs on the AOM driver units and the MOT magnetic field gradient within a single experimental run, i.e. during the various stages of the MOT and evaporative cooling (section 3.7.4). Eight additional analogue outputs on a separate control card[32] and the frequency and power settings of the microwave signal generator which are controlled via General Purpose Interface Bus (GPIB), are not synchronised with the FPGA clock. These can only be changed in between experiments to scan parameters which remain constant within an experimental run, e.g. detunings of the Rydberg EIT light.

3.5 Two-dimensional magneto-optical trap

Typical experiments in Rydberg quantum optics work on time scales of a µs [28, 29] and may be repeated many times by recycling the same ultra-cold

[32]National Instruments PCI 6713.

atomic ensemble. Therefore, the time to load a MOT [193] as a first step in the ensemble preparation – typically on the order of hundreds of ms to tens of s – represents a major contribution to the overall time budget. The MOT loading rate depends on the density of trappable atoms within the MOT trapping volume and to reduce it, either the atom density or trapping volume have to be increased. In our case, the latter is infeasible due to spatial constraints imposed by the in-vacuo optics (section 3.2.1) while increasing the partial pressure of Rb inside the vacuum chamber is also problematic as an increasing number of atoms above the MOT capture velocity deteriorates trap lifetimes due to increased background collisions. Even more importantly, an increased Rb background leads to atom deposition on the aspheric lenses reducing their transmission.

Therefore, a two chamber approach including a 2D MOT [94] as a switchable high flux cold atomic beam source, was chosen to reduce the loading time as the directed nature of the atomic beam prevents the deposition of rubidium on the lenses. A 2D MOT offers the following advantages over the most common alternative approach, a Zeeman slower [222]: The beam is switchable without a mechanical in-vacuo shutter, a lower beam divergence thanks to transverse cooling, and a more compact setup. The main disadvantages compared to a Zeeman slower are the need of significantly higher laser power for cooling and a more involved optical and mechanical design.

Briefly summarised, a 2D MOT works by magneto-optically confining atoms in two dimensions to form a bright atomic beam along the zero field line of an elongated quadrupole magnetic field [94]. This occurs in a vacuum region with a comparatively high Rb background pressure and in a large, elongated cooling volume to capture a large number of atoms. The beam is directed straight at the location of the MOT passing through a differential pumping tube with a small aperture into the main science chamber kept at a much lower pressure. Atoms with a low velocity along the beam axis are subjected to the cooling light for longer time than fast ones and thus more strongly confined around the beam centre such that the

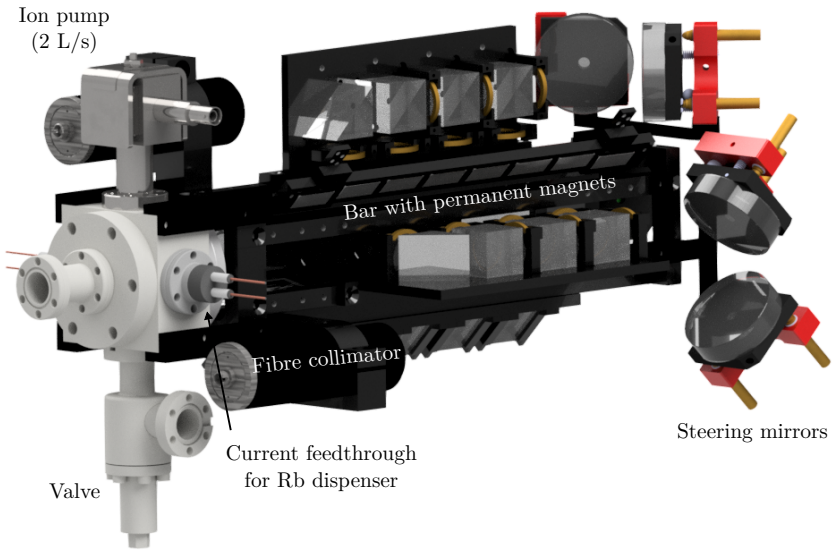

Figure 3.6: Overview of the 2D MOT setup. The 2D MOT is realised in a UHV glass cell which attaches to a rectangular block also hosting feedthroughs for the Rb dispensers, an ion pump and a valve for roughing pumps. A cage surrounding the vacuum system mounts the optics for the cooling light and bars with permanent magnets to generate an elongated quadrupole field.

aperture acts as a velocity filter, ideally with a 'cut-off' near the capture velocity of the MOT.

The implementation of a 2D MOT in our setup including a cage surrounding a UHV glass cell (figure 3.6) to house the required optics and using permanent magnets [223] to implement the quadrupole field, is inspired by a design implemented at Heidelberg University, Germany [101, 224–227]. However, several modifications have been made, i.e. to minimise the amount of optomechanics required and increasing the length of the cooling volume to reduce the beam divergence. This is important due to the highly constrained capture volume of our setup compared to other MOTs where beam diameters of 2 cm or more are not uncommon.

3.5.1 Vacuum system

The 2D MOT is realised in a quasi-autonomous vacuum system shown partly in figures 3.6 and 3.7 which permits independent vacuum breaks for maintenance. At the heart is a custom made rectangular UHV glass cell[33] with inner dimensions 25 mm × 25 mm × 150 mm. The outer surfaces of the cell are AR coated for 780 nm. The inner surfaces were left uncoated since the coating performance can deteriorate when Rb atoms are adsorbed and the index matching breaks down. The differential pumping tube (length 149 mm, inner diameter 6 mm) is welded to a CF40 to CF16 reducing flange which also connects to the main chamber. Its 0.8 mm aperture is located at the end of the cooling volume (figure 3.7) in the rectangular part of the cell[34] and its conical tip prevents reflections of a co-propagating pushing beam (see below) into the atomic beam.

Two alkali metal dispensers[35] each containing 0.25 g of Rb at natural abundance serve as atom source and are mounted parallel to the pumping tube emitting atoms directly into the cooling volume. A compact 2 L/s ion pump[36] permits pumping the 2D MOT vacuum section independently.[37] The glass cell and the flange with the differential pumping tube attach to opposing CF40 ports of a rectangular block while the ion pump, current feedthroughs for resistive heating of the dispensers, and an angle valve attach to the remaining four CF16 ports at the side of the block. The 2D MOT vacuum section attaches to the main chamber via CF16 tubes and a gate valve to isolate both sections if necessary.

[33] Japan Cell Co., manufactured from Tempax borosilicate glass.
[34] This minimises atom loss on the aperture due divergence of the atomic beam.
[35] Alvatec Alvasource AS-3-Rb-250-F.
[36] Gamma Vacuum Titan 3S-CV-1V-5K-N-N.
[37] The pump is not used during day-to-day operation as we are unsure about its correct operation and suitable vacuum conditions can be maintained through the differential pumping tube.

3.5.2 Optical Setup

To maximise the number of atoms captured in the atomic beam and cool them sufficiently, a large, elongated cooling volume of several centimetres is essential [228, 229]. Cooling occurs on the same transition, $|5S_{1/2}, F = 2\rangle \rightarrow |5P_{3/2}, F' = 3\rangle$ in ^{87}Rb, and with a similar red-detuning as in a conventional MOT. The elongated volume is typically created by two elliptical beams intersecting at 90° on the atomic beam axis [94, 223, 228–230] which requires large, often custom-made optics. Instead, we chose a more compact arrangement of four smaller, consecutive circular cooling regions [101, 224, 231] (figure 3.7). Cooling and repumping light for each axis are delivered via the same optical fibres. The cooling beams with a $1/e^2$-diameter of 18 mm are distributed by polarisation optics set to achieve approximately equal intensities for each region. The regions' centres are separated by 37.5 mm and no significant loss in atomic flux occurs due to the discontinuity in the cooling volume [231]. As in a conventional MOT, the cooling light is circularly polarised by quarter-wave plates (QWPs) behind each PBS. The beams are retro-reflected using rectangular prisms instead of mirrors, preserving the polarisation's helicity and omitting the need of QWPs for retroreflection. The beams can be aligned using a mirror pair located behind a homebuilt fibre collimator (figure 3.6). Following completion of the setup, optical guiding along the beam axis has been reported as an interesting method to further reduce beam divergence [232, 233] in addition to long cooling volumes.

Purely two-dimensional confinement does not cool the atoms along the beam axis such that two counter-propagating atomic beams are created if no additional force is applied. Two approaches are typically taken to reverse atoms moving in the wrong direction and thus increase the flux. Either a red-detuned pushing beam [101, 223, 228, 230], or an imbalanced optical molasses in a so called 2D$^+$ MOT [94, 229] can be applied coaxially with the beam. We chose a pushing beam with a $1/e^2$-diameter of 9 mm because it requires less optics. Its red-detuning is typically large compared

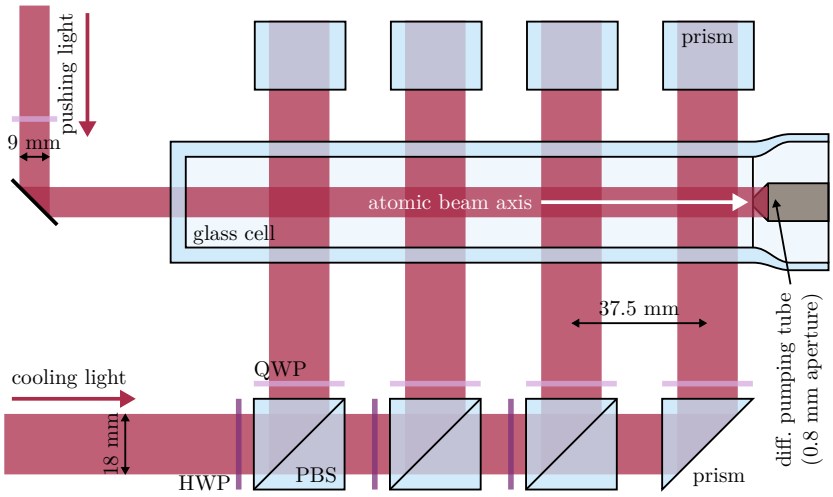

Figure 3.7: Optical setup of the 2D MOT. The cooling light is split into consecutive cooling regions using polarisation optics. Another four cooling beams are intersecting perpendicular on the atomic beam axis (not shown as out of the plane of the page). A pushing beam co-propagates along the atomic beam axis to increase atom flux. Both cooling light and pushing beam are circularly polarised and delivered by PM optical fibres.

to the cooling light in order to address and reverse atoms over a wide range of velocity classes.

3.5.3 Magnetic field

Besides laser cooling, a 2D MOT requires an elongated magnetic quadrupole field whose zero line defines the beam axis [94]. Because the operation can be controlled entirely by switching the cooling lasers, it can be generated by permanent magnets [101, 223, 224] which offer several advantages over electromagnets. Their magnetisation remains constant such that resulting stray fields are not subject to fluctuations, no heat is dissipated in the vicinity of the experiment, strong yet small off-the-shelf neodymium magnets enable a very compact design, and finally no supply and control electronics are needed.

Permanent magnets have been used by various research groups before

[101, 223]. Their arrangement is adapted from the same design as the entire 2D MOT setup [101]. Sixteen rectangular permanent magnets[38] are held in two bars. The distance between both bars is adjustable using different mounting holes on the 2D MOT cage. The only modification compared to the original Heidelberg design [101, 224–227] is the addition of further magnet pairs to elongate the array and ensure a constant field gradient along the additional fourth cooling region. We typically operate the 2D MOT with a field gradient of approximately 16 G/cm.

Background fields, i.e. the earth magnetic field, cause a shift of the magnetic field zero line with respect to the aperture in the differential pumping tube such that the atomic beam can partially or fully miss the aperture. The shift is compensated by applying weak compensation fields using two pairs of rectangular coils which surround the 2D MOT cage (not shown in figure 3.6).[39]

3.6 Efficiently loaded magneto-optical trap

In the previous generation of the experiment [104, 234], the performance of the MOT [193], both in terms of loading speed and overall atom number, represented a major bottleneck limiting cycle times and the number of atoms in and thus optical depth of the microscopic optical dipole trap. This was a consequence of closely spaced aspheric lenses used to achieve high resolution which imposed small beam diameters and a narrow intersection angle for the radial beams. In this generation, we return to a 'standard' configuration where larger beams intersect at angles of 90°. This is made possible thanks to the improved optical access resulting from the longer focal length and cut edges of the in-vacuo aspheric lenses, see figure 3.8 (a) and section 3.2.1. In combination with loading from the atomic beam generated by the 2D MOT, $2.5 \pm 0.2 \cdot 10^7$ atoms can be trapped in less than

[38] Eclipse Magnets N750-RB.

[39] The original idea of moving one of the two bars holding the permanent magnets on a compact translation stage was discarded due to spatial contraints.

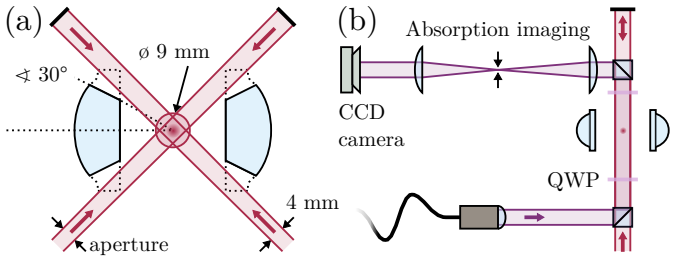

Figure 3.8: Realisation of the MOT and constraints imposed by in-vacuo lenses. (a) The in-vacuo lenses are cut at the edges to allow the radial MOT beams to intersect at an angle of 90°. To avoid reflections on the lenses, the radial beam diameter is truncated to 4 mm in the radial plane. (b) Due to limited optical access the axial MOT and an absorption imaging beam are overlapped using polarisation optics.

150 ms. Details on the implementation of the MOT and characterisation of the loading process are presented below.

3.6.1 MOT setup

The optical geometry of the MOT is shown in figure 3.8. The quadrupole magnetic field which provides the field gradient for the MOT is produced by the in-vacuo anti-Helmholtz coils described in section 3.2. The MOT is realised in a standard configuration using three retro-reflected cooling beams intersecting at 90°. Cooling and repumping light are delivered from the laser system (section 3.3) to the experiment by PM optical fibres, and multiplexed by overlapping and coupling them into a 1:3 fibre beam splitter.[40] The three outputs provide light for circularly polarised cooling beams with $1/e^2$-diameters of 9 mm. The radial cooling beams are both truncated at 4 mm in the radial plane by masks on the vacuum viewports as shown in figure 3.8 (a) to avoid reflections from the in-vacuo lenses.[41] The axial beam is overlapped with an imaging beam with opposite polarisation and separated again by a PBS cube placed between the QWP

[40] Schäfter + Kirchhoff.

[41] Reflections from the lenses can affect MOT performance and even prevent trapping altogether.

and retroreflecting mirror for the cooling light, see figure 3.8 (b).

3.6.2 Absorption imaging

Imaging of ultra-cold atoms is not only an important diagnostic tool, but their position and momentum distribution also convey further information, e.g. to identify the phase transition between thermal and degenerate quantum gases [195–197]. We use absorption imaging [235] to determine atom numbers and density distributions in the MOT and infer further parameters, i.e. temperature. The imaging setup is shown in figure 3.8 (b). The imaging light originates from one of the branches in the 780 nm laser system otherwise supplying signal light (section 3.3). The imaging beam has a $1/e^2$-diameter of 7 mm and passes horizontally through the vacuum chamber via the same viewports as the axial MOT beams (section 3.6). The beams are overlapped with opposite polarisation and separated by a PBS after passing thorugh the science chamber. At the position of the trapped atoms, the imaging light is circularly polarised. A quantisation field is applied along the beam axis. A telescope of two achromatic lenses[42] in a $4f$-configuration images the atoms onto a charge-coupled device (CCD) camera,[43] demagnified by a factor of 0.5. The imaging beam is aligned at a slight angle relative to the MOT beam to prevent leakage of MOT cooling light through the PBS from building up unwanted charge on the CCD before imaging.

3.6.3 Characterisation of MOT loading

In the following, the loading performance achieved by the MOT-2D MOT combination is investigated. The discussion is limited to parameters which are characteristic for our setup and excludes parameters for which characterisation reveals similar optima as in other ^{87}Rb setups. All optimal parameters are summarised in table 3.1. The trap loading rates are inferred

[42] Thorlabs AC508-400B (+400 mm) and AC508-200B (+200 mm).
[43] Andor Luca.

Table 3.1: Optimal parameters for MOT loading.

Parameter	Value
2D MOT cooling power	140 mW
2D MOT cooling detuning	−8.5 MHz
2D MOT repumping power	3 mW
2D MOT pushing power	20 mW
2D MOT pushing detuning	−35.0 MHz
2D MOT magnetic field gradient	16 G/cm
MOT cooling power	30 mW
MOT cooling detuning	−12.0 MHz
MOT repumping power	300 µW
MOT field gradient (axial)	34.4 G/cm

by fitting saturation curves to the number of trapped atoms measured as function of different loading times. The atom numbers are determined using absorption imaging (section 3.6.2). Note that in most of the following figures, the errorbars[44] are obscured by size of the corresponding markers and dominated by larger systematic errors resulting from the absorption imaging.

2D MOT: cooling volume

The size and specific geometry of the 2D MOT cooling volume are important as they determine how many atoms are captured into the atomic beam and its divergence (section 3.5.2). Figure 3.9, presents values for the MOT loading rate when between two and all four of the circular cooling regions are in use, both with and without the use of a red-detuned pushing beam along the atomic beam axis. To reduce the number of regions, cooling beam pairs are blocked starting with the one furthest away from the differential pumping tube to minimise beam divergence before the aperture. Increasing from three to four regions, the loading rate increases from $6.2 \pm 0.3 \cdot 10^7$

[44]Statistical standard errors obtained from the fit results of typically four to five curves fitted with eleven data points each.

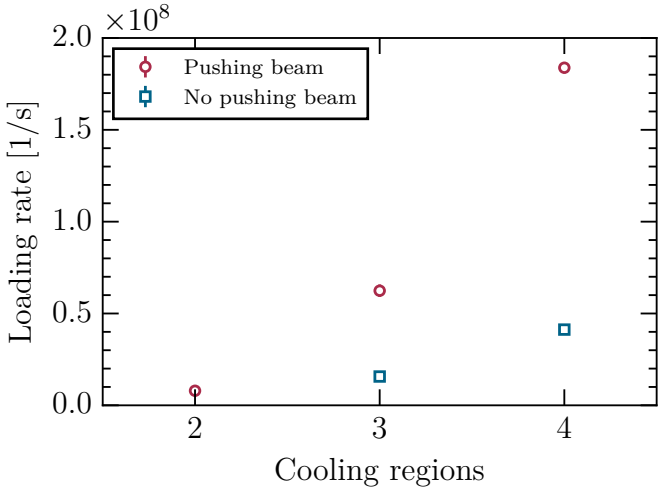

Figure 3.9: Influence of 2D MOT cooling volume on MOT loading rate. The loading rate increases substantially with the size of the cooling volume as more cooling regions are unblocked. The addition of a pushing beam copropagating with the atomic beam enhances the performance by a factor of ≈ 4.5.

to $1.8 \pm 0.3 \cdot 10^8$ atoms/s. This emphasises the importance of good beam collimation in combination with a small MOT cooling volume.[45]

Besides the length of the cooling volume, the pushing beam greatly improves MOT loading as atom flux is enhanced by reversing atoms that initially move in the wrong direction as discussed in section 3.5. When all four cooling regions are in use, the loading rate increases by a factor of approximately 4.5. Considering that the overall atom number in both beams is initially similar, one might expect the loading rate to double at most. However, measurements of the velocity distribution in other setups [224, 225, 228] show that additional atoms have a very low velocity in the beam direction. Due to the comparatively small MOT cooling volume and

[45] Using a photodiode to detect MOT flourescence, we measure atom numbers and loading rates which are significantly higher (typically more than a factor of 5) possibly due to reflections on the in-vacuo lenses. In addition, absorption imaging results might underestimate the atom number due to the relatively small diameter of the imaging beam resulting in low intensities and thus a low dynamic range in the wings of the imaging beam, and due to potential charge built up on the CCD caused by leaked MOT light (compare section 3.6.2).

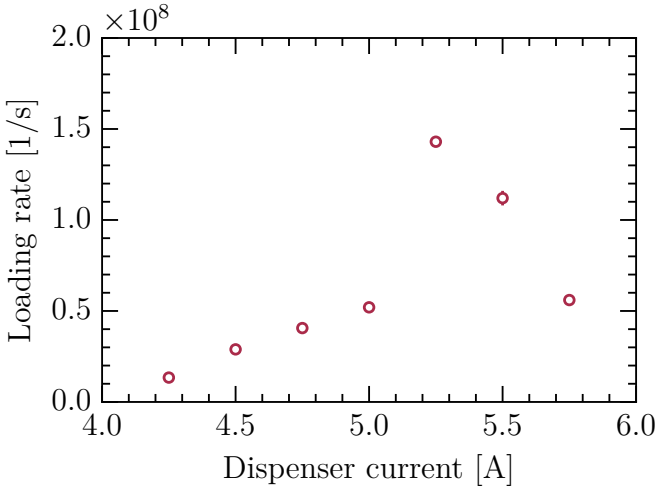

Figure 3.10: Influence of Rb partial pressure in 2D MOT on MOT loading rate. As the actual pressure cannot be directly measured, the loading rate is shown as a function of the current applied to heat the Rb dispensers.

thus low capture velocity of our MOT, the lower end of the longitudinal velocity distribution is particularly critical, i.e. because the cooling volume is shortest along the atom beam axis due to the truncation by the lenses.

2D MOT: Rb partial pressure

Considering the fundamental principle of a 2D MOT [94] – generating an atomic beam in a well separated, higher pressure vacuum region – the ^{87}Rb partial pressure inside the 2D MOT glass-cell necessarily has a strong influence on its performance. If the pressure is low, fewer atoms are captured into the beam. If it is too high, atoms are lost due to background collisions. The partial pressure can be controlled by adjusting the current applied to resistively heat the Rb dispensers. Since we cannot directly measure the pressure inside the glass cell, we measure the MOT loading rate as a function of the dispenser current.[46]

The results of the measurement are presented in figure 3.10. The highest

[46] While it is found that the optimal current remains the same day-to-day, it may change over time, e.g. due to degradation of the dispenser.

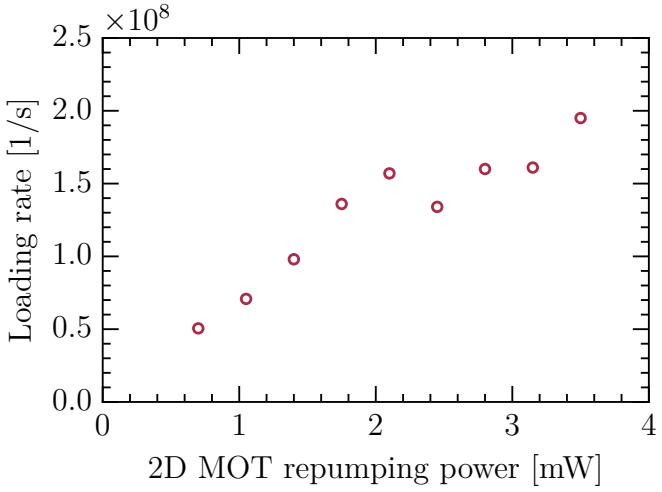

Figure 3.11: Influence of 2D MOT repumping power on MOT loading rate. The loading rate increases with the repumping power.

loading rate is measured for a current of 5.25 A. At the highest current applied, 5.75 A, a pressure increase above 10^{-10} mbar can be measured inside the science chamber.

2D MOT: Repuming power

2D MOTs rely on good repumping to achieve good performance due to high densities in the atomic beam which lead to enhanced loss from hyperfine changing collisions [91]. This and the large cooling volume imply that significantly more repumping power is required compared to a conventional MOT. Figure 3.11 shows the MOT loading rate measured for different repumping powers. Best performance is achieved for a power of 3.5 mW yet no clear saturation is observed, increasing the power further is difficult as it would negatively affect the repumping power in the MOT.

MOT: Field gradient and detuning

Besides the diameter of the cooling beams, the size of a MOT's volume is also determined by the combination of the magnetic field gradient

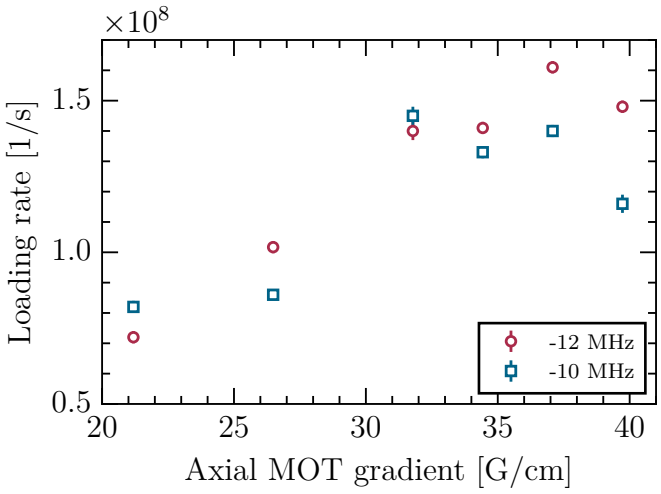

Figure 3.12: Influence of MOT magnetic field gradient on MOT loading rate. The loading rate is shown for MOT detunings of −10 and −12 MHz. The values correspond to the axial gradient, the radial field gradient is half.

and cooling light detuning. The force experienced by the atoms scales approximately linearly with the field gradient [91] implying that a high field gradient is beneficial. However, in combination with large cooling beams optimal values are typically of order 20 to 30 G/cm (for the axial gradient) in combination with a red detuning below −10 MHz for Rb [226] due to strong Zeeman shifts in the wings of the cooling beams. Figure 3.12 shows the loading rate for different magnetic field gradients between ≈ 20 and 40 G/cm. We find that the loading rate is best for steeper gradients which is presumably a consequence of the reduced size of our MOT beams. To avoid excessive heating of the in-vacuo anti-Helmholtz coils, we do not exceed gradients of 34.4 G/cm during MOT loading.

3.7 Side-by-side photonic channels

The experimental setup described in this chapter is built with the intention of studying effective interactions between photons propagating through or

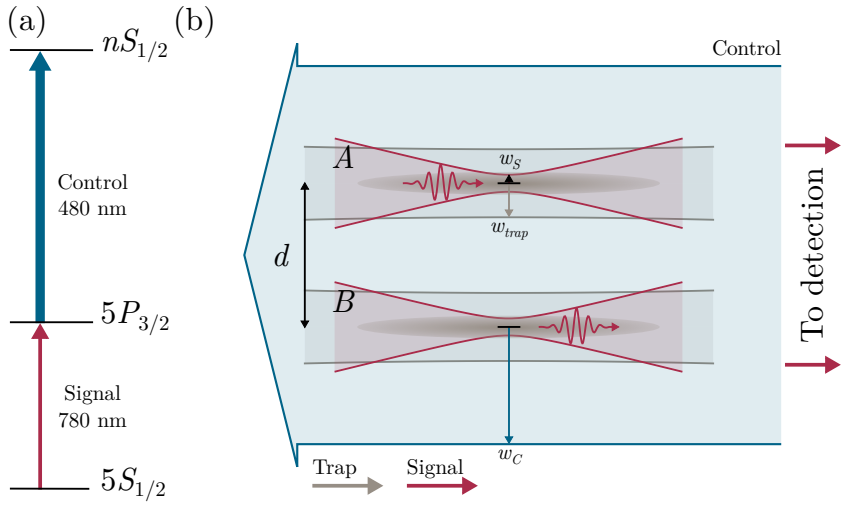

Figure 3.13: Realisation of side-by-side photonic channels. (a) Transitions for Rydberg EIT in ^{87}Rb. The signal light typically couples $|5S_{1/2}, F = 2, m_F = 2\rangle \rightarrow |5P_{3/2}, F = 3, m_F = 3\rangle$ and the control field is resonant with $|5P_{3/2}, F = 3, m_F = 3\rangle \rightarrow |nS_{1/2}\rangle$. Both are usually circularly polarised. (b) Channel geometry. Both channels A and B consist of a signal beam tightly focussed ($1/e^2$-radius w_S) into an elliptical cloud of cold ^{87}Rb atoms which is confined in a far red-detuned (910 nm) optical tweezer with $1/e^2$-radius w_{trap}. The distance d between channels is adjustable and the propagation of signal photons is controlled by a common control field with $1/e^2$-waist radius w_C.

stored in microscopic ensembles of ^{87}Rb atoms. In particular, the goal is to realise individual, spatially separated photon channels between which µm-ranged Rydberg mediated interactions [65] take place without spatial overlap of the signal light, e.g. to realise photonic quantum gates [70, 71], to study spin models and energy transfer [64, 90, 138], as well as other strongly interacting many body systems. Our approach to realise such channels is illustrated in figure 3.13. Using EIT and/or photon storage, the dipolar interactions between collective Rydberg excitations are mapped onto signal photons either by storing them as spin-waves [45, 46] or while propagating as Rydberg polaritons [26, 40, 54] (chapter 2).

Within the context of this thesis, we realise two interacting channels for signal photons separated by an adjustable distance d of the order of 10 µm.

This is comparable to the range of the dipolar interactions [18, 19] and blockade [20, 21] between Rydberg atoms and allows to spatially resolve non-local, Rydberg mediated photon interactions, e.g. to implement gates between dual-rail encoded optical qubits [70]. Each channel consists of a tightly focussed optical mode in which the signal light propagates and a microscopic cloud of optically trapped ^{87}Rb atoms acts as optical medium. A single counter-propagating control field couples the signal photons and atomic media to a Rydberg state in a EIT configuration and addresses both channels simultaneously. The current implementation includes two side-by-side channels, but is in principle extendible to larger arrays, for example by adapting techniques employed to generate arbitrary arrays of individual atoms using a spatial light modulator (SLM) [96, 205]. Individual aspects of the channel setup are subsequently described, including the optical setup, detection of signal photons, the microscopic cold atom ensembles, and generation and delivery of the control light.

3.7.1 Optical setup

The setup to realise two photonic channels A and B is shown in figure 3.14. Each channel consists of a signal mode and a trapping beam for the microscopic optical dipole trap which confines the corresponding atomic medium. Using the in-vacuo lenses (section 3.2.1), signal and trapping light are focussed to $1/e^2$-waists of $1.0 \pm 0.1\,\mu$m and $4.5 \pm 0.3, \mu$m, respectively.[47] The distance d between channels can be measured by imaging the signal beams in the focal plane of the aspheric lens pair onto a CMOS camera[48] at $\approx$ 39-fold magnification using a telescope consisting of the second in-vacuo lens and a subsequent achromat[49] ($f = +400\,$mm) which is also used for fluorescence imaging of the microscopic ensembles (section 3.7.2 and figure 3.15).

[47] These focal spot sizes are measured using a knife-edge mounted on a piezo-controlled translation stage in the focal plane of a reference lens placed outside the vacuum chamber (section 3.2.1).
[48] Thorlabs DCC1545M.
[49] Thorlabs AC508-400-B.

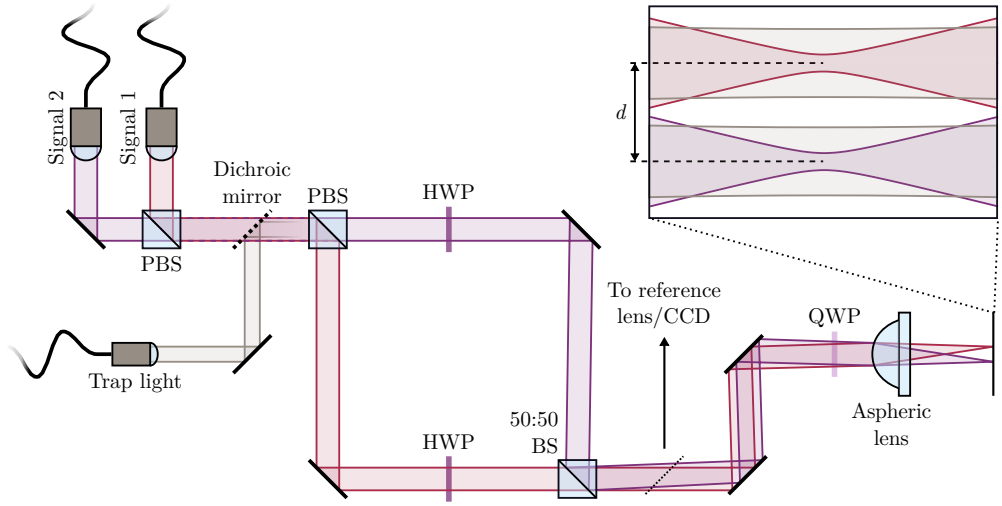

Figure 3.14: Optical setup for side-by-side photonic channels. Both signal beams are initially overlapped with the trap light on a dichroic mirror. The two channels are separated in a Mach-Zehnder like setup before recombination on a non-polarising beamsplitter. The channel separation d can be adjusted by changing the beams' incident angle on the aspheric lens using a mirror in the Mach-Zehnder path of channel B.

After delivery to the experiment by PM optical fibres,[50] signal and trapping light are initially overlapped on a dichroic mirror and subsequently separated again into two separate channels A and B on a PBS. The light for the individual channels passes through different arms of an arrangement resembling a Mach-Zehnder interferometer. Afterwards, the channels are recombined on a 50:50 non-polarising beam splitter (NPBS).[51] The inter-channel separation d is adjusted by tilting and translating the mirror in one of the arms to adjust the angle at which the beams for that channel are incident on the aspheric lens.

[50] The quality of the signal mode after outcoupling from the fibre is crucial to achieve near diffraction limited performance when focussing with the in-vacuo lens. Consequently, precision commercial fibre collimators (Thorlabs F810APC-780) are used to achieve a clean beam profile for the signal light.

[51] Despite the loss of trap light, a NPBS is preferred instead of a PBS to allow independent adjustment of the signal polarisation in each channel.

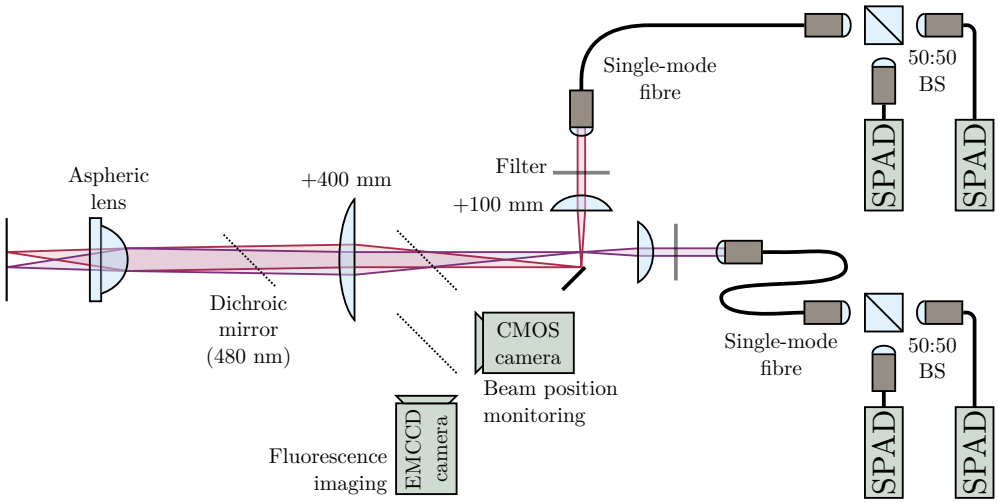

Figure 3.15: Single photon detection setup. Both signal modes are separated with an edge mirror at the focus of a 4:1 telescope and coupled into single mode fibres. Behind each fibre two SPADs are arranged in a HBT setup. Using flip mirrors the signal beam foci can be imaged onto a camera to monitor their position during alignment. Similarly, flip mirrors can be used to image the fluorescence of the microscopic cold atom clouds onto a EMCCD camera.

3.7.2 Fluorescence imaging

Due to their small size, imaging of microscopic atomic ensembles confined in dipole traps is challenging and requires high resolution and good detection efficiencies. Since we create cigar shaped, elongated ensembles along the lens axis (section 3.7.4 below), imaging perpendicular to the lens axis, e.g. using the absorption imaging setup described above (section 3.6.2) or via fluorescence imaging through the bottom viewport (figure 3.1), is desirable, but difficult to implement with reasonably high magnification due to the distance between the atoms' position and vacuum viewports. Instead, we implement fluorescence imaging along the axis of the in-vacuo lenses as shown in figure 3.15.

The field of view of the asphere covers approximately 10% of the solid angle and its short focal length, $f = +10.3\,\mathrm{mm}$ allows imaging at ≈ 39-fold magnification in combination with the subsequent $f = +400\,\mathrm{mm}$

achromat placed outside the vacuum chamber (see above). During imaging, the atoms are illuminated by the MOT light and their fluorescence is imaged onto a EMCCD camera.[52] During typical exposure times of a few 10 µs, the microscopic ensembles expand to multiples of their original size and out of the focal plane of the imaging system in the axial direction. Consequently, the ability to infer quantitative information about the traps beyond their position is limited and fluorescence imaging is mainly used to obtain qualitative information, and as an alignment tool.

3.7.3 Single photon detection

As the experimental setup is dedicated to Rydberg quantum optics [28, 29], it was decided to focus on all-optical, EIT-based detection schemes for Rydberg excitations [26, 33, 62–64] and to forgo more common detection schemes via field-ionisation and a micro-channel plate (MCP) or channeltron [101, 211]. Detecting optical non-linearities at the level of individual photons and identifying non-classical states of light, requires the ability to not only detect, but also to measure correlations between single photons [163]. Investigating interaction effects, both within the same and between spatially separate channels, requires correlation analysis within each and across channels. Consequently, signal photons are detected independently in each channel and correlations are analysed in software post processing. As shown in figure 3.15, the detection setups for each channel consist of two SPADs arranged as HBT interferometers [236].

The foci of the individual signal modes inside the vacuum chamber are imaged at ≈ 39 fold magnification (see above and section 3.7.2). This allows to separate them with a translatable edge mirror. Subsequently, the individual signal modes are recollimated and coupled into PM single mode optical fibres. These are aligned onto the original signal modes and thus act as a mode filter to distinguish photons in their original mode from those emitted elsewhere, e.g. as a result of motional or interaction-induced

[52] Andor iXon.

dephasing [49, 50, 177] during photon storage (section 2.3). The PM fibres can be replaced by multi-mode fibres e.g. to detect fluorescence in addition to signal light retrieved in the original signal modes. Filter pairs[53] placed before each fibre block the dipole trap at 910 nm and other background light.[54]

Behind each fibre, SPAD pairs[55] and a 50:50 NPBS are arranged as HBT interferometers to detect signal photons and enable the analysis of photon counting statistics. Due to imperfect NPBS cubes and imbalances in the detection efficiencies of the individual detectors, the effective splitting ratios of the setups are not precisely 50:50.[56] This is taken into account when analysing photon statistics. Typical overall detection efficiencies including the quantum efficiencies of the detectors and transmission loss between the focal plane of in-vacuo lens pair to the detectors are slightly above $\gtrsim 20\%$. Besides the SPAD quantum efficiencies ($\approx 60\%$), the detection efficiency is mostly limited by the ITO coatings of the in-vacuo collection lens, the filters, and fibre coupling ($\gtrsim 80\%$ efficiency).

Individual detection events are recorded independently using the fast digital inputs of the FPGA based experimental control system (section 3.4) with a time resolution of 5 ns. Correlations are analysed in software post-processing providing the flexibility to investigate different correlations in the same data set, e.g. single- or cross-channel, or single-channel conditional on the detection of a photon in the second channel.[57] In the following chapters all errors stated for detected photon numbers and derived quantities generally exclude systematic errors. The latter predominantly arise from the calibration uncertainty ($\pm 3\%$ at 780 nm) of the power meter

[53] Semrock MaxLine LL01-780-25 and Comar 780 IH 25.

[54] Two filters are required since the MaxLine filters only partially block back-reflected control light at 480 nm.

[55] Perkin-Elmer/Excelitas SPCM-AQRH-14-FC.

[56] Following completion of the experiments presented in this thesis, the single-mode fibres and HBT setups have been replaced by single-mode fibre beam splitters (OZ Optics) to simplify the setup and reduce transmission loss.

[57] The software that interprets the photon detection time tags was implemented by P. Huillery.

heads[58] used to determine the loss in the photon detection setup and are relevant when absolute rather than normalised photon numbers are stated.

3.7.4 Microscopic optical dipole traps

Red-detuned optical dipole traps [92, 194] are well suited to strongly confine cold atoms in a well localised volume defined by the optical mode of a single (or several overlapping) focussed laser beams. Using the in-vacuo aspheres (section 3.2.1), we can tightly focus trapping beams and thus strongly confine microscopic ensembles of atoms well below the range of Rydberg interactions [18, 19] (section 2.1). The individual traps are realised as simple single beam far off-resonance traps (FORTs) whose trapping potentials are proportional to the intensity profile of the Gaussian beams [92, 237]. The trap light has a wavelength of 910 nm. This provides good compromise between the suppression of off-resonant Raman transitions and the ability to achieve reasonable trap depth at moderate powers [92]. The general implementation is very similar to our previous setup (with slightly different beam powers and sizes) which has been discussed in detail in the thesis of D. Maxwell [234].

Laser system

The dipole trap laser system is kept very simple. The trap light originates from a homebuilt ECDL[59] and is amplified by a homebuilt TA. Both have been described in the thesis of D. Maxwell [234].[60] The light is switched by a single-pass AOM[61] which also controls the trap light intensity. The diffracted light is coupled into a PM optical fibre and transferred to the experiment. While a significant fraction of trapping light is lost due to the finite coupling efficiency, the fibre acts as mode filter which is of

[58] Thorlabs S120C and S121C.
[59] Following completion of the experiments presented in this thesis, the laser has been replaced by a commercial ECDL (Toptica DL pro).
[60] See references [238] and [239] for the original designs.
[61] AA Optoelectronics MT-200A0,5-800

fundamental importance to achieve near-diffraction limited performance to generate tightly focussed, microscopic optical dipole traps in combination with in-vacuo lenses.

Optical setup and trap parameters

The optical setup to realise the individual traps shown in figure 3.16 (a) is straightforward. Using the in-vacuo aspheric lens, the trapping light is focussed to a $1/e^2$-waist radius of $4.5 \pm 0.3\,\mu m$. In order to co-locate the foci of the signal and trapping light, the trapping beam has to converge upon incidence onto the lens to compensate for the focal length mismatch between wavelengths. Consequently, the lens for fibre outcoupling is translatable to adjust the beam divergence. The focus of the signal light is located at the centre of the lens pair whose separation is chosen to re-collimate a signal beam. To match its position, the size and con-/divergence of the trapping beam are measured and adjusted symmetrically before and after the vacuum chamber. The Mach-Zehnder-like optical setup shown in figure 3.14 allows to realise separate side-by-side traps for each signal channel.

The resulting potential is shown in figure 3.16 (b). Based on the equations above, we obtain a trap depth of $U_0/k_B \approx 428\,\mu K$ and trapping frequencies of $\omega_z/2\pi = 0.65\,kHz$ (axial) and $\omega_r/2\pi = 13\,kHz$ (radial) for a single beam trap at 910 nm with $w_0 = 4.5\,\mu m$ at a typical beam power of 50 mW at the trap position.[62].

Dipole trap loading

The number and temperature of atoms loaded into an optical dipole trap can be optimised by increasing the density and lowering the temperature of the atoms which are held in the MOT following the loading process. The entire sequence employed to load the microscopic dipole traps is presented in figure 3.17. Initially the MOT is loaded by the 2D MOT for 100 ms

[62]The potentials were calculated using a dipole trap simulator software developed by the group of S. Cornish, see e.g. the thesis of T. Wiles for details [221]

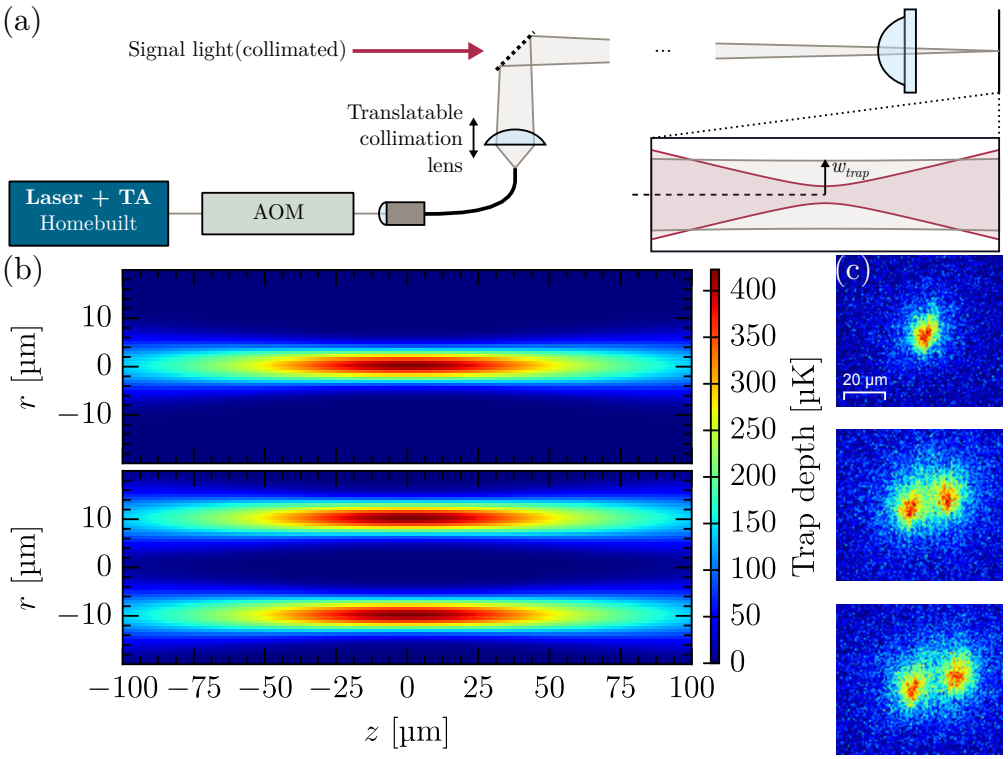

Figure 3.16: Side-by-side microscopic optical traps. (a) The 910 nm trap light originates from an amplified diode laser, is switched by an AOM, and delivered by optical fibre. Using the in-vacuo lens, the trap light is focussed to $\approx 4.5\,\mu$m. The convergence of the trapping beam is adjustable via the collimation lens behind the fibre to adapt the focal planes of the traps to the signal light. (b) Calculated trap potentials for a single and two tweezers separated by $d = 20\,\mu$m at a beam power of 50 mW per trap. (c) Fluorescence images of a single and two side-by-side tweezers with different separations d taken through the in-vacuo lens at ≈ 39-fold magnification. Due to expansion during imaging, the clouds are larger than during typical experiments.

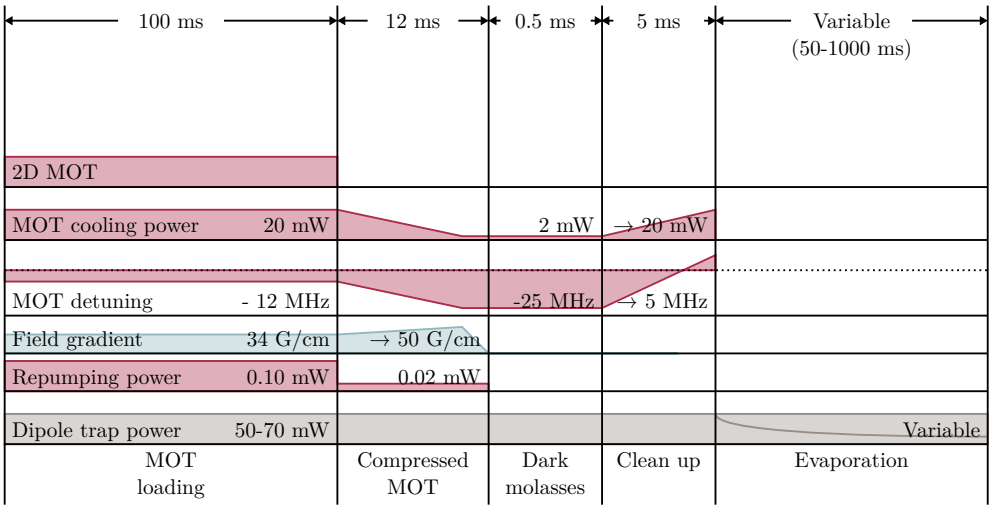

Figure 3.17: Sequence for preparation of ultra-cold microscopic atomic ensembles. Following loading for typically 100 ms, the MOT is compressed to increase the atom density. Subsequently, the temperature is reduced during a dark molasses phase. The dipole trap power remains constant throughout these stages. An optional evaporation stage allows to reduce the dimensions of the atomic ensemble. If no evaporation is applied, untrapped background atoms are pushed out of the experimental region during a 'clean up' stage (see text).

until the atom number in the MOT almost saturates. Parameters such as beam powers, detunings, and the magnetic field gradient are stated in the figure. The dipole trap is switched on at full power during the loading since the AC Stark shift induced by the trap light shifts the repumping light off resonance at the trap position creating an effective dark spot [240]. This confines atoms in the lower $F = 1$ hyperfine level of the ground state where they are no longer subject to light-induced collisions leading to an increase in density.[63] Subsequently, we compress the MOT during 12 ms by increasing the field gradient from 34.4 to 50.3 G/cm (axial) to enhance the atomic density [241]. To reduce light assisted collisions, the intensities of the cooling and repumping light are decreased and the cooling

[63] In practice, it is not necessary to fully load the MOT due to the small size of the dipole traps and we find that the optical depth of the microscopic ensembles is similar even for loading times below 50 ms.

light red detuning is increased during the compression. To further benefit from sub-Doppler cooling [242] the atoms are finally subjected to a dark optical molasses for 0.5 ms. At the end of the molasses stage, we measure temperatures below 50 µK using time of flight imaging [243].

Untrapped atoms that leave the experimental region too slowly following release from the MOT, can lead to unwanted absorption of signal light outside the atomic ensembles confined in the dipole traps. Due to the large size of the collimated signal beams away from their tight foci (see above), it takes several tens of ms until untrapped atoms drop sufficiently far under gravity and no longer scatter signal light. Therefore, we apply a 5 ms 'clean up' stage during which background atoms are pushed out of the experimental region by reactivating the MOT cooling beams and ramping them to a blue detuning. This does not affect atoms trapped in the dipole traps since the blue detuning does not exceed the AC Stark shift they experience due to the trap light. Optionally, an additional stage of free or forced evaporative cooling [244] in the dipole trap can be applied to reduce the temperature and thus the volume occupied by the atomic ensembles to avoid absorption cross-talk between separate channels. In this case, the 'clean up' stage is omitted.

Dipole trap characterisation

In most experiments, properties of optically trapped cold atomic ensembles like their size, atom number, or density, are determined via absorption or fluorescence imaging [235]. However, most experiments also work with much larger ensembles. Microscopic ensembles like in our experiment are more difficult to image. They require high optical resolution and if they cannot be confined during the imaging, short exposure times on the order of µs due to rapid thermal expansion of the ensembles relative to their original size, result in bad signal-to-noise ratios. Currently, imaging the microscopic ensembles is only feasible through the in-vacuo lenses using the fluorescence imaging setup described in section 3.7.2. Figure 3.16 (c) shows fluorescence images of both an individual and two side-by-side

atomic ensembles. It is immediately noticeable that the diameter of the atom distributions exceeds the trap beam waist as the spatial extent of the cigar-shaped ensemble extends beyond the depth of field of the in-vacuo lens and due to expansion during the exposure time of 20 µs. Therefore, we refrain from inferring any parameters of the ensembles from fluorescence imaging beyond an estimate of atom numbers of order a few 10^3 based on the amount of fluorescence detected.

In Rydberg quantum optics [28, 29] however, one is rather interested in an ensemble's response as an optical medium for signal light which can be readily detemined by measuring transmission spectra of signal light. This only provides limited information on the spatial properties, but nonetheless some estimates can be made. Firstly, the resonant absorption of signal light reduces dramatically if the signal waist exceeds $1/e^2$-radii of $w_S \approx 3\,\mu\text{m}$ and is strongest for waists of 2.5 µm when no evaporative cooling is applied. Second, the length of the cigar-shaped ensemble can be estimated based on the approximate width and ratio of the trap frequencies. Without evaporation, we therefore estimate the standard deviations of the Gaussian atomic density distribution at $\approx 2.5\,\mu\text{m}$ (radial) and $\approx 40\,\mu\text{m}$ (axial). Following 400 ms of free evaporation at a constant trap light intensity [244], we estimate 1.5 µm (radial) and 20 µm (axial) based on similar arguments. These parameters also achieve the best agreement with experimental results for the counting statistics of signal photons retrieved after storage as Rydberg spin-waves based on a dephasing model [50]. The model will be introduced in section 4.3.2 and is sensitive to the geometry of the atomic cloud.

Recycling of atomic ensembles

As highlighted in the introduction of this chapter experiments in Rydberg quantum optics [28, 29] rely on the acquisition of large datasets to analyse photon statistics. Besides optimising the preparation of the atomic ensembles (section 3.6), effective cycle times also decrease strongly if the ensemble can be recycled many times before a new one needs to

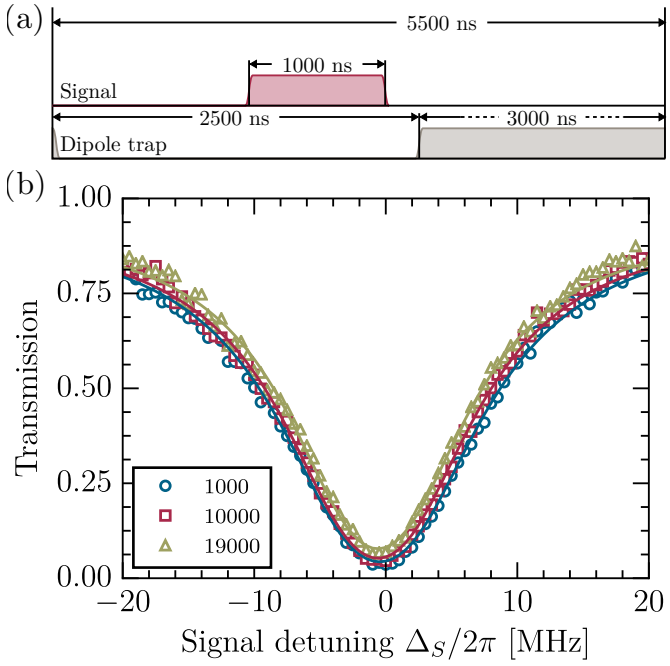

Figure 3.18: Recycling of microscopic atomic ensembles. (a) Experimental sequence to measure signal transmission through microscopic atomic ensemble. The trapping light is switched off while probing the ensemble to avoid AC Stark shifts. (b) Transmission spectrum of the signal transmission measured after 1000, 10 000, and 19 000 repetitions of the above sequence and averaged over 1000 subsequent shots for incoming signal pulses containing a mean of ≈ 3.1 photons. There is no strong change in the optical depth of the atomic ensemble as it is recycled. No errorbars are shown due to the density of datapoints.

be prepared. A typical experimental sequence is shown in figure 3.18 (a). To avoid AC Stark shifts, the trapping light is switched off during experiments. Between each individual experiment, here with duration 2.5 µs, the dipole trap potential is restored, here for 3 µs, to avoid atom loss due to thermal expansion of the ensemble. We repeat the sequence 20 000 times and measure signal transmission spectra as we probe a typical atom cloud with signal pulses of duration 1 µs and mean photon number ≈ 3.1 to investigate whether there is a strong change in optical depth. Here, the waist radius of the signal mode is $w_S \approx 2\,\mu\text{m}$ instead of $1.0 \pm 0.1\,\mu\text{m}$ as

stated above and used in all measurements presented subsequently in this chapter. Figure 3.18 shows typical spectra averaged over 1000 subsequent experiments (2000 measurements per datapoint in total) after the cloud has been recycled 1000, 10 000, and 19 000 times, respectively, in which no strong change in optical depth is observed. Adding up a preparation time of 72.5 ms (using a shorter MOT loading time of 50 µs compared to 3.17) and $20\,000 \cdot 5.5\,\mu s = 110\,ms$ to perform typical experiments an effective cycle rate of $20\,000/182.5\,ms \approx 110\,kHz$ can be deduced providing a good starting point for Rydberg quantum optics experiments.

Cross-talk and evaporative cooling

An important consideration for the realisation of two side-by-side photonic channels is whether there is cross-talk between them in the sense that signal photons in channel A are scattered by atoms belonging to channel B or vice versa, or even worse stored in the wrong channel. Such cross-talk could lead to the observation of interaction effects that originate from effective interactions between photons that are detected in and thus attributed to different channels but interact within the same medium. The tight foci of the signal modes of $1.0 \pm 0.1\,\mu m$ (compare also figure 3.13) imply that they are strongly diverging and cross-talk may occur if the cigar shaped ensembles are sufficiently long to overlap with the wings of the signal mode of the wrong channel. Figures 3.19 compares transmission spectra for signal light when the ensembles are prepared without the addition of an evaporative cooling stage (evaporation time in figure 3.17 set to 15 ms) and either the correct or only the medium of the wrong channel is present, for a channel separation of $d = 10\,\mu m$. Here, the duration of the signal pulses is 1 µs and the ensembles are probed 20 000 times before reloading the traps (40 000 measurements per datapoint in total).

The volume occupied of a thermal cold atomic gas confined in a harmonic potential is determined by its temperature which defines the fraction of atoms that occupy higher lying eigenstates. Hotter atoms are more likely to be found further away from the trap centre due to the larger spatial extent

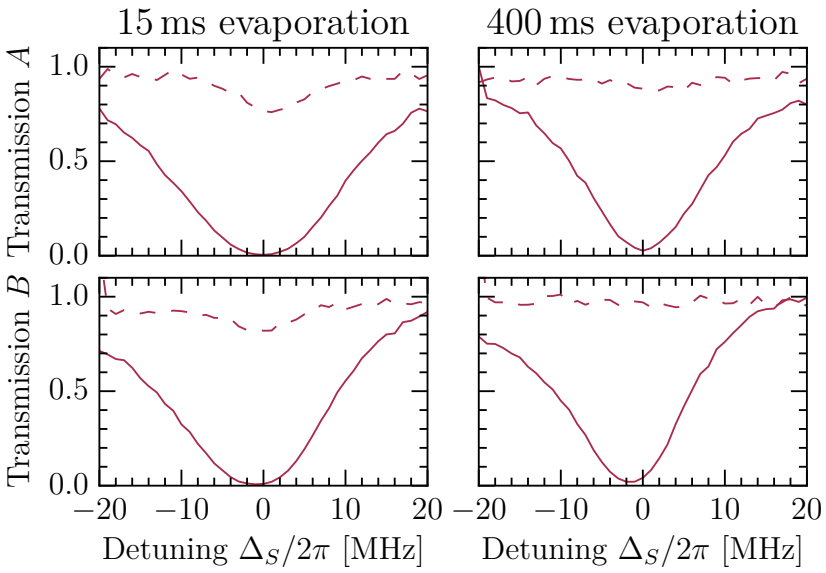

Figure 3.19: Effect of evaporative cooling on cross-talk in signal transmission for $d = 10\,\mu\text{m}$. The solid lines correspond to spectra which are taken when the corresponding medium is present. The dashed spectra are recorded with the medium of the corressponding channel absent.

of their wavefunctions. Consequently, reducing the atoms' temperature provides a handle to improve their confinement and thus reduce cross-talk between the two channels. An obvious route to cool the atoms and enhance their confinement in the dipole trap is evaporative cooling [244]. This can be seen in figure 3.19 which also shows signal transmission spectra taken after a 400 ms stage of free evaporative cooling (maintaining a constant trap light intensity) has been introduced before the ensembles are probed.[64] While there is significant cross-talk for evaporative cooling lasting only 15 ms, cross-channel scattering of signal light can be significantly reduced if the atomic ensembles are subjected to evaporative cooling for 400 ms.

Finally, figure 3.20 shows the cross-talk in resonant signal transmission as the evaporation time is varied. For evaporation times increased to several

[64] The evaporation process can be accelerated using forced evaporation by exponentially lowering the trapping potential during the evaporation time. However we refrain from using forced evaporation as we found that the resulting reduction in cross-talk is more sensitive to drifts in experimental parameters.

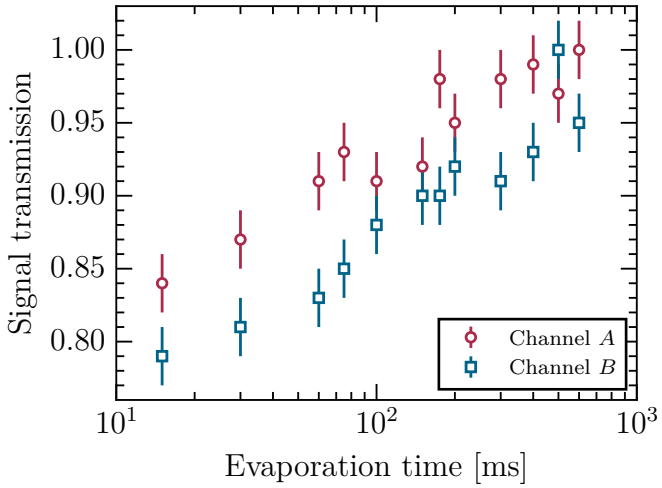

Figure 3.20: Cross-talk in resonant signal transmission as function of evaporation time. Scattering of signal light by atoms in the adjacent trap reduces as the ensembles shrink as a result of lower temperatures.

100 ms, a regime can be reached where cross-talk in signal transmission is almost absent. In order to avoid excessive prolongation of the ensemble preparation and still achieve reasonable cycle times, we typically apply evaporative cooling for 400 ms. For this choice, there is still slight cross-talk in signal transmission for $d = 10\,\mu\text{m}$, but we do not observe any cross-talk in photon storage (section 5.4) and transmission cross-talk vanishes entirely for slightly large separations $d \geq 11\,\mu\text{m}$. The signal pulse has a duration of 1 µs and a mean photon number of ≈ 1.3.

3.7.5 Coupling to Rydberg states

Experiments in EIT [32] based Rydberg quantum optics [28, 29] (chapter 2) in a single or in spatially separated signal channels as introduced above, require a control field that couples the intermediate state $|e\rangle = |5P_{3/2}, F' = 3\rangle$ to a Rydberg state $|r\rangle$ as shown in figure 3.13 (a). For Rb atoms, the corresponding optical transitions have wavelengths around 480 nm. A

single control field addresses both channels A and B simultaneously.[65] The control field and signal photons have opposing circular polarisation and are counter-propagating to increase the spin-wave period during photon storage (section 2.3) to reduce the impact of motional dephasing [177] and minimise the effect of optical Doppler shifts.

Due to the short control wavelength and focal length of the in-vacuo lenses, focussing of a collimated control beam would result in foci with $1/e^2$-radii of no more than a few µm. Ensuring a reasonably constant control intensity over the entire ensembles and addressing both channels simultaneously requires a much larger and spatially more uniform control field. Therefore, the control light is focussed using a $f = 400\,\text{mm}$ achromat[66] placed immediately after the fibre outcoupler. The focal point can moved slightly before the first in-vacuo lens by translating the achromat. Theoretically, the chosen geometry results in a $1/e^2$-radius of $\approx 25\,\mu\text{m}$ for a focus located exactly between the two lenses. Due to the sensitivity of the spot size on the focus before the lens, measuring the control beam using a reference lens is unreliable. Instead, the achromat is translated until the con-/divergence of the control light is symmetric around the lens pair to ensure the focus is centred. As a consequence of the arising uncertainty in the control beam size, any control Rabi frequencies Ω_C stated for the experiments presented subsequently are not calculated, but determined by measuring Autler-Townes spectra [32, 164] (section 4.1.1).

480 nm laser system

Coupling the intermediate state $|e\rangle = |5P_{3/2}, F' = 3\rangle$ to a Rydberg state $|r\rangle = |nS_{3/2}, F' = 3\rangle$ requires control light with wavelengths around 480 nm. This is provided by a commercial laser system[67] which frequency-doubles the output of an amplified ECDL via second harmonic generation (SHG).

[65] Implementation of individual control fields for individual addressing of each channel is currently under way.
[66] Thorlabs AC254-400-A.
[67] Toptica TA-SHG 110.

Figure 3.21 shows a schematic of the laser system.

Immediately after the output, the laser beam is tightly focussed through a Rb vapour cell where it is overlapped with a counter-propagating probe beam resonant with the $|g\rangle = |5S_{1/2}, F = 2\rangle$ to $|e\rangle = |5P_{3/2}, F' = 3\rangle$ signal transition to generate an EIT spectrum and stabilise the laser directly on resonance with the control transition (see below). The windows of the cell are Brewster-cut to maximise transmission of the 480 nm light.

The control light is switched by a polarisation switching electro-optical modulator (EOM)[68] placed between two crossed Glan-Taylor (GT) polarisers. Subsequently, the control light is coupled into a PM optical fibre for transfer to the experiment. The EOM introduces some leakage of the wrong polarisation component which cannot be filtered by the second polariser. Nonetheless, extinction ratios exceeding 46 dB can be achieved in combination with the fibre as the residual light propagates in a different, slightly displaced optical mode. The pulse shape of the control light is controlled by a 25 MHz AFG[69] whose signal is amplified by a high voltage amplifier.[70][71] The switching rise and fall times are approximately 100 ns.

Frequency stabilisation: Electromagnetically induced transparency

Generating a dispersive reference from a EIT spectrum generated in a thermal vapour cell provides a simple and cost-effective technique to stabilise a laser to an excited state transition, e.g. to Rydberg states [218, 219]. The probe light for the EIT lock is split-off in the 780 nm laser system (figure 3.5). Since it is initially −140 MHz below the probe transition, the probe light is switched onto resonance by a double-passed AOM. This configuration allows to slightly vary the probe frequency by

[68] Leysop EM200K-AR480.
[69] Tektronix AFG2022B.
[70] Leysop Series 250.
[71] Due to dynamical effects in the EOM, it can be necessary to dynamically change the voltage applied between pulses to maintain good extinction, i.e. to avoid premature retrieval of stored photons triggered by leaked control light.

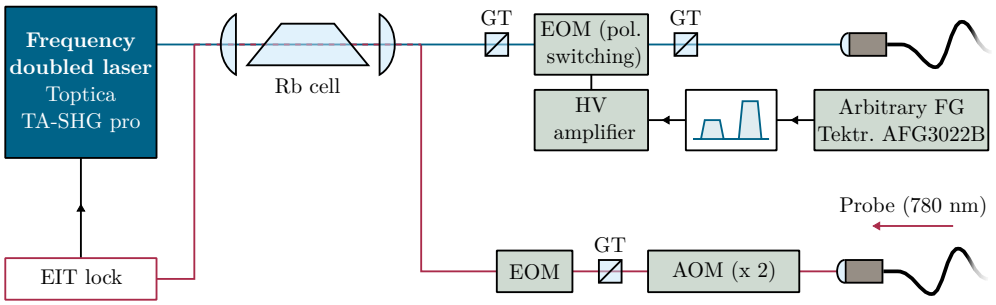

Figure 3.21: Overview of the 480 nm laser system. The output of a frequency doubled diode laser is overlapped with counter-propagating probe light in a Rb cell to generate an EIT signal for stabilisation to Rydberg transitions. A polarisation switching EOM placed between two crossed GT polarisers is used for switching. An arbitrary function generator controls the pulse shape. The probe light for the EIT lock is delivered by fibre and modulated by an EOM. A double-passed AOM allows to shift the lock point.

a few MHz, e.g. to compensate for stray electric fields or to scan the control detuning Δ_C near a Rydberg transition. A homebuilt EOM [217] modulates sidebands onto the probe light and a GT polariser before the EOM cleans the polarisation.[72] After passing through the vapour cell, the probe light is detected on a fast amplified photodiode.[73] A homebuilt lock-in circuit [245] and a commercial PID controller[74] provide feedback to the laser.

The peak-to-peak voltage and slope of the error signal depend on the contrast of the EIT transmission feature. To achieve strong transmission, high coupling Rabi frequencies Ω_C are required. Unfortunately, these decrease rapidly when increasing the principal quantum number n of $|r\rangle$ since the transition dipole moment is reduced as a consequence of the increased orbital radius of the Rydberg electron ($\propto n^2$, section 2.1).

[72] This is necessary to avoid drifts in the offset of the error signal caused by small fluctuations in the polarisation.
[73] Hamamatsu CI10508-01 (10 MHz bandwidth).
[74] Toptica FALC110.

Therefore the entire output of the laser passes through the reference cell where it is overlapped with the probe light to generate the EIT spectra. In combination with tight focussing inside the cell, this leads to error signals sufficient for locking even at comparatively high principal quantum numbers $n \approx 110$. A disadvantage of this approach is that Δ_C can only be scanned in a small window around resonance. However, excitation far off resonance from the intermediate state is typically not required in EIT based Rydberg quantum optics [27, 28].

4 Rydberg non-linear optics: Experiments

To demonstrate the capability of the new experimental setup presented in the preceding chapter to perform experiments in Rydberg quantum optics [27–29] at high repetition rates, a series of fundamental experiments and techniques is presented below. Rydberg EIT [33] is demonstrated as a fundamental tool to map the long-range dipolar interactions between Rydberg atoms [18, 19] onto photons to generate optical non-linearities at the few photon level (section 4.1) [26, 40]. It allows to store photons as strongly interacting collective Rydberg excitations [45, 46, 89] (section 4.2) resulting in the generation of highly non-classical states of light (section 4.3).

All experiments presented in this chapter are carried out with signal photons in a single channel as introduced in section 3.7. However, the experiments also represent fundamental prerequisites for the main result of this thesis presented subsequently in chapter 5, the study of contactless effective interactions between photons in two spatially separated, non-overlapping channels. Conceptually, both series of experiments are highly related as the non-local aspect inherently emerges from the long-range character of the dipolar interactions between Rydberg excitations independent of the channel geometry.

Besides the author, P. Huillery, S. W. Ball, and T. Ilieva contributed to the experiments presented in this chapter. The work was supervised by C. S. Adams and M. P. A. Jones.

This chapter is in part based on the following publications [85, 88]:

- H. Busche, S. W. Ball, and P. Huillery, "A high repetition rate experimental setup for quantum non-linear optics with cold Rydberg atoms", Eur. Phys. J. Spec. Top. **225,** 2839–2861 (2016).
- H. Busche, P. Huillery, S. W. Ball, T. V. Ilieva, M. P. A. Jones, and C. S. Adams, "Contactless non-linear optics mediated by long-range Rydberg interactions", Nat. Phys., to appear (2017).

4.1 Electromagnetically induced transparency

Besides the interacting Rydberg excitations themselves, EIT [32] (section 2.2.3) is the most important tool of the trade to map the strong interactions between Rydberg atoms [18, 19] onto both classical light fields and single photons. Non-linear effects can be either directly observed in the transmission of a signal field as Rydberg interactions shift the control field off-resonance and revert the transparent three-level to an opaque two-level system [26, 40], or by temporarily storing photons as strongly interacting collective Rydberg excitations which relies on EIT to convert optical photons into Rydberg spin-waves [45, 46].

Figure 4.1 presents a typical experiment to measure Rydberg EIT spectra [33, 117]. The signal and control light, resonant with the $|g\rangle = |5S_{1/2}, F = 2, m_F = 2\rangle$ to $|e\rangle = |5P_{3/2}, F' = 3, m'_F = 3\rangle$ and $|e\rangle$ to $|r\rangle = |30S_{1/2}\rangle$ transitions, are counter-propagating with opposing circular polarisation. A quantisation field is applied along the beam axis. For the data presented in this section, the $1/e^2$-radius of the signal light is $\approx 2.5\,\mu m$ at the focus and the estimated extent of the cigar-shaped atomic ensemble is $2.5\,\mu m$ in the radial and $40\,\mu m$ in the axial direction (standard deviations of Gaussian density distribution, see section 3.7.4). Following preparation of the microscopic atom cloud, the timing sequence shown in figure 4.1 (c) is carried out 20 000 times. The dipole trap light is switched off every

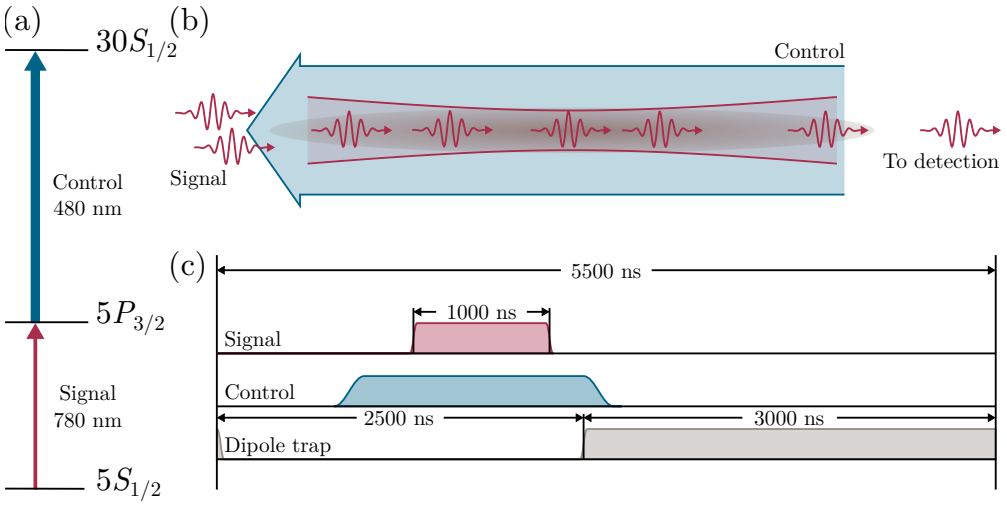

Figure 4.1: Experimental setup and sequence for Rydberg EIT. (a) Level scheme of transitions used for Rydberg EIT. Signal light: $|g\rangle = |5S_{1/2}, F = 2, m_F = 2\rangle$ to $|e\rangle = |5P_{3/2}, F' = 3, m'_F = 3\rangle$, control field: $|e\rangle$ to $|r\rangle = |nS_{1/2}\rangle$. (b) Experimental geometry. The signal ($1/e^2$-waist radius $\approx 2.5\,\mathrm{mm}$) and control modes are counter-propagating along the cigar-shaped atomic medium with standard deviations of 2.5 µm (radial) and 40 µm (axial) for the atoms' Gaussian density distribution. (c) Timing sequence for the EIT fields and the optical trap.

5.5 µs for 2.5 µs. During this time the atoms are probed with a 1 µs pulse of signal light. The control light is switched on and off well before and after the signal pulse to ensure its Rabi frequency Ω_C intensity remains constant throughout the entire duration of the signal pulse.

As discussed in the previous chapter (section 3.7), the ability to perform several hundreds or thousands of experiments on the same microscopic ensemble is crucial in Rydberg quantum optics to obtain good photon statistics on reasonable timescales. In analogy to the absorption experiment presented in figure 3.18 which shows that atom loss from the ensemble is low for signal pulses containing only few photons, we perform a similar experiment to ensure there is no strong trap loss under Rydberg EIT conditions. Rydberg atoms in $|nS_{1/2}\rangle$ states are anti-trapped by a dipole trap beam of wavelength 910 nm such that loss may arise if the Rydberg

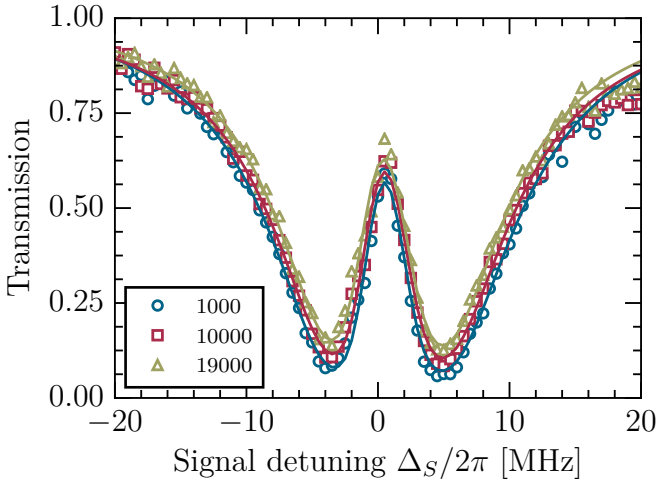

Figure 4.2: Observation of Rydberg EIT. Here, the control field couples to $|r\rangle = |30S_{1/2}\rangle$. The data points represent an average of 1000 subsequent repetitions without reloading the optical trap and are taken immediately after loading (blue circles), 10 000 (red squares), and 19 000 (yellow triangles) repetitions on the same ensemble. No strong reduction in optical depth or EIT transmission due to atom loss is observed as the experiment is repeated. Errorbars are not shown due to the high density of data points.

state is significantly populated when the trap is turned back on. To avoid any influence of interactions on the spectra, the control field couples to a Rydberg state with comparatively low principal quantum number $|30S_{1/2}\rangle$. Figure 4.2 shows EIT spectra taken for 1000 subsequent after the 1000, 10 000, and 19 000 repetitions on the same ensemble and each data point is averaged over 2000 repetitions in total. The signal pulses contain a mean photon number of ≈ 2.6. The absence of a strong decrease in the optical depth or EIT transmission as the ensemble is recycled represents a promising starting point for further experiments at high repetition rates.

4.1.1 Autler-Townes splitting

The Rabi frequency of the control light Ω_C represents an important quantity. It determines, for example, the group velocity at which Rydberg polaritons [38] (section 2.3.1) propagate through the atomic medium and

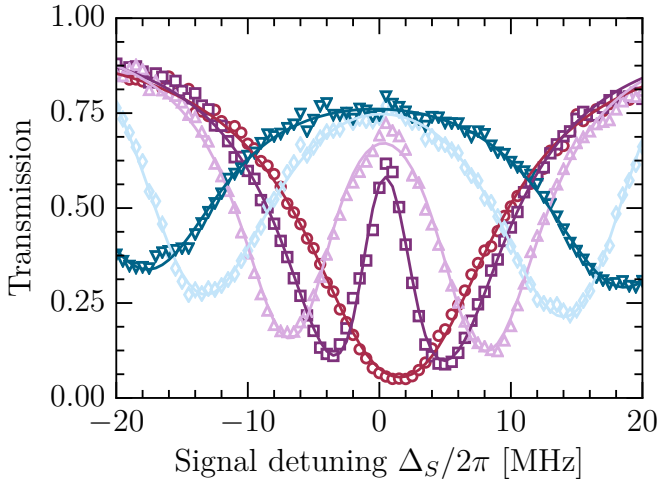

Figure 4.3: Rydberg EIT/Autler-Townes spectra at $|r\rangle = |30S_{1/2}\rangle$. An absorbative two-level medium (red circles) transitions into a transparent three-level EIT medium as Ω_C is increased, finally resulting in Autler-Townes splitting. When fitting the spectra, we obtain $\Omega_C/2\pi = 7.9 \pm 0.1$ (purple squares), 14.6 ± 0.1 (pink triangles), 28.6 ± 0.2 (light blue diamonds), and 35.8 ± 0.3 MHz (dark blue triangles). Errorbars are not shown due to the high density of data points.

well-controlled adaption of Ω_C is required for photon storage and retrieval [38, 176] (section 2.3). Due to the alignment sensitivity of the control light setup (section 3.7.5), inferring Ω_C from beam size estimates is unreliable. Instead, Ω_C can be directly calibrated by measuring Autler-Townes splittings [164] at different control intensities which are proportional to Ω_C.[1] Figure 4.3 shows typical Autler-Townes spectra measured under the same conditions as the EIT spectra above. Each data point represents an average of 40 000 individual measurements. Again, $|30S_{1/2}\rangle$ is used for $|r\rangle$ to minimise the influence of Rydberg interactions. At higher principal quantum numbers n interaction effects become important and the splitting is less pronounced due to the reduced transition dipole moment between $|e\rangle$ and $|r\rangle$. Therefore, the splitting for a specific intensity is typically

[1] As Ω_C is not perfectly uniform across the atomic medium, the obtained values represent an average over the entire EIT medium.

measured at $n = 30$ and rescaled accordingly for higher n.

4.1.2 Suppression of Electromagnetically induced transparency

The first observation of a strong non-linear optical response in cold Rb atoms induced by Rydberg interactions was an intensity dependent breakdown of EIT in a ladder scheme including a Rydberg state [26]. For sufficiently dense media and states exhibiting strong Rydberg blockade [20, 21], this can lead to anti-bunching and the generation of a train of single photons [40].

The underlying effect has been illustrated in figure 2.4 and discussed in section 2.2.4. For low signal intensities and thus low rates of incoming photons, the polaritons' large average temporal spacing translates into a large spatial separation while they propagate through the three-level atomic medium. At high intensities however, the spatial separation is reduced as the incoming rate of incident photons increases. Thus it becomes more likely for two polaritons to be separated by less than the EIT Rydberg blockade $r^{(6)}_{b,EIT}$. Within a blockaded sphere of radius $r^{(6)}_{b,EIT}$, the control field is shifted off-resonance due to VdW interactions. Consequently, the three-level EIT medium reverts to a two-level system inside the blockaded volume and is no longer transparent for resonant signal light as its susceptibility is changed. As more polaritons propagate through the medium, a larger fraction is affected by the breakdown of EIT and overall transmission reduces.

To provide a first demonstration of Rydberg non-linear optics in the new experimental setup (section 3), we measure transmission spectra for different signal intensities under EIT conditions where the control light couples to the Rydberg state $|r\rangle = |80S_{1/2}\rangle$. In this regime, strong interaction effects are expected as $r^{(6)}_{b,EIT} \approx 9\,\mu\text{m}$, well above the average interatomic spacing at densities on the order of $10^{12}/\text{cm}^3$. The experimental sequence remains as in figure 4.1. The control Rabi frequency is $\Omega_C/2\pi =$

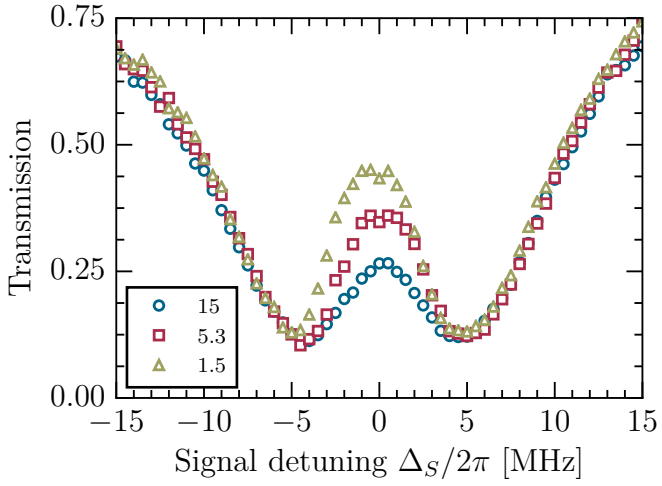

Figure 4.4: Non-linear response of a Rydberg EIT medium at $|r\rangle = |80S_{1/2}\rangle$. The spectra correspond to coherent signal pulses with mean photon numbers 15 ± 1 (blue circles), 5.3 ± 0.4 (red squares), and 1.5 ± 0.1 (yellow triangles) and duration 1 µs. As number of incoming signal photons increases, the average spacing of polaritons is reduced in the EIT medium leading to stronger interaction induced-level shifts. A break down of resonant transmission occurs as an increasingly larger fraction of the medium is subject to dipole blockade.

7.3 ± 0.6 MHz and the signal pulse duration 1 µs. Figure 4.4 shows the results for incoming signal pulses with mean photon numbers 15 ± 1, 5.3 ± 0.4, and 1.5 ± 0.1 where each datapoint represents the average of 40 000 transmission measurements. The expected suppression effect is clearly visible. Stronger suppression can be achieved working with larger and thus optically denser media [40, 56, 57, 89]. Since we typically use photon storage to enhance interactions [45, 46, 89], this poses no limitation at this point and the dipole trap geometry could easily be adapted to achieve a higher optical depth. In a related fashion, one can also alter the non-linear response by changing the atomic density and thus number of scatterers per blockaded sphere [41].

4.2 Photon storage

The strength of optical non-linearities for photons propagating as Rydberg polaritons under EIT conditions [26, 40, 54] depends on the path length inside the atomic medium which determines the interaction time. The limited control over the relative positions of the polaritons can also limit control over the interaction. Photon storage [38, 39] (section 2.3) allows us to temporarily convert signal photons into stationary collective Rydberg excitations [45, 46] in a coherent manner. The stationary nature enhances the effect of Rydberg mediated interactions by increasing the interaction time to induce dephasing [45, 89] (section 2.3.3), enables a single gate photon to locally modify for optical switches [55], transistors [56, 57], and phase shifters [59], and opens perspectives to study many-body dynamics, e.g. of interacting spins [138] or non-radiative energy transfer [133] in analogy to individual Rydberg atoms. In addition, both the phase of photons and the interactions between them can be manipulated by microwave fields [46, 47] when stored, e.g. to implement controlled qubit rotations [70]. The enhanced localisation also facilitates the investigation of the non-local character of Rydberg-induced non-linearities in the following chapter.

Figure 4.5 shows the experimental geometry and protocol employed. The storage protocol [38, 39, 170] uses the same states and transitions for signal and control light as in figure 4.1. The geometry of the optical modes and optically trapped, cigar-shaped ^{87}Rb ensemble also remain unchanged from the EIT experiments in section 4.1. While a coherent pulse of signal photons propagates through the atomic medium, the control field Rabi frequency Ω_C is reduced to zero, thereby converting signal photons into collective Rydberg excitations in the form of atomic spin-waves as their group velocity is reduced to zero. Following a variable storage time t_{st}, photons are retrieved by restoring the control field. When stating t_{st}, this refers to the time the control field is actually extinguished as observed by a fast photodiode, i.e. excluding the fall and rise times which are of order 100 ns and limited by the response time of the polarisation switching EOM

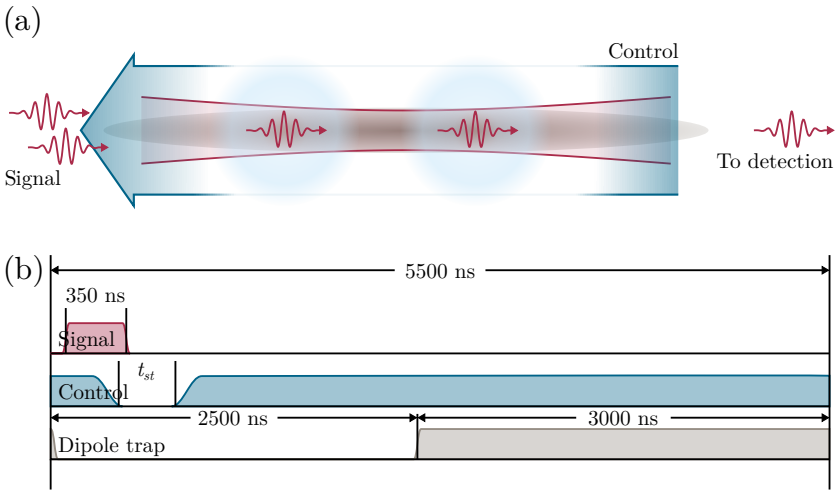

Figure 4.5: Experimental implementation of photon storage. (a) Signal photons ($1/e^2$-waist radius 2.5 µm) and control light are counter-propagating in optical modes focussed into a microscopic, cigar-shaped storage medium (standard deviation of Gaussian atom distribution: ≈ 2.5 µm and 40 µm). (b) Timing sequence. While a square pulse of signal photons (duration 350 ns) propagates through the medium, the control field is reduced to zero to store them. The photons are retrieved after t_{st} by restoring the control field. The optical trap is turned off during storage experiments.

and its amplifier used for extinction (section 3.7.5).

Figure 4.6 (a) shows a histogram of signal photon detection events (using the detection setup described in section 3.7.3 in combination with a multi-mode fibre to collect the retrieved light) for a typical storage-and-retrieval experiment acquired over 20 million repeated cycles. Here, the photons are stored in a low-lying Rydberg state $|r\rangle = |30S_{1/2}\rangle$ where no significant interaction is expected. The incoming signal pulse has a mean photon number of ≈ 11 and duration 350 ns and the photons are stored for $t_{st} \approx 450$ ns using a control Rabi frequency of $\Omega_C/2\pi = 18 \pm 1$ MHz. For retrieval $\Omega_C/2\pi = 44 \pm 3$ MHz is increased to the maximal possible value resulting in a narrow retrieved pulse. The atomic cloud has an optical depth of ≈ 2.5 containing an estimate of a few 10^3 atoms.

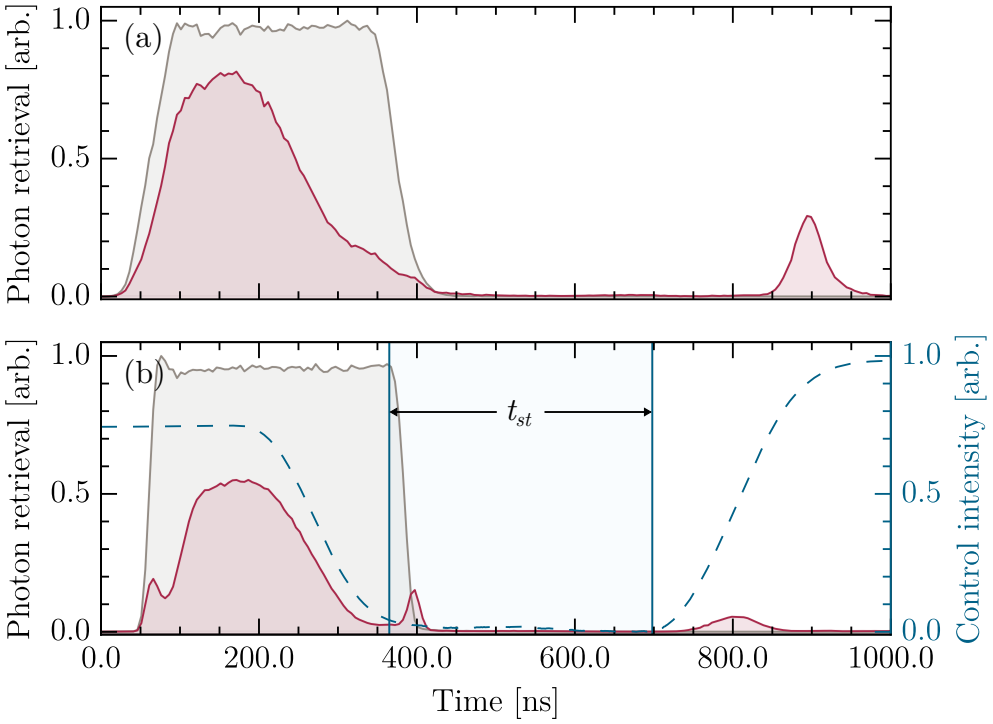

Figure 4.6: Detected photons during storage-and-retrieval sequence. (a) Incoming signal pulse (grey) and signal photons detected during storage and retrieval (red). (b) The detected number of retrieved photons is reduced when using a single-mode instead of a multi-mode fibre as in (a). The blue line corresponds to the control intensity recorded on a photodiode, the shaded area corresponds to t_{st}. Faster switching of the signal light (≈ 25 ns fall time in panel b) leads to the observation of a flash of signal light emitted in the forward direction following the extinction of the signal field around 400 ns [246].

When starting to reduce Ω_C at $\approx 200\,\text{ns}$, a reduction in signal transmission can be observed as photons are stored and the resonant transmission reduces. As the efficiency of the storage process is limited, the retrieved photon number is only a fraction of the incoming pulse. The following processes contribute to the loss: a significant number of photons is scattered by the atoms due to imperfect transparency during the storage process; some signal photons are transmitted as the optical depth of the medium is insufficient to compress the entire signal pulse inside the medium while the control field is turned off; stored photons are retrieved outside their original optical mode due to dephasing effects 2.3.4, i.e. motional dephasing; and due to the lacking ability to shape both signal and control pulses at this stage, the storage and retrieval sequence does not correspond to the ideal, adiabatic scenario [38, 170, 176, 178].

Figure 4.6 (b) shows a similar experiment, where the switching time of the signal field is reduced to $\approx 25\,\text{ns}$ and the multi-mode fibre before the detection setup is replaced by a single-mode fibre. The lower signal transmission and increased width of the retrieved pulse are the result of a lower control Rabi frequency. Panel (b) also shows the control intensity throughout the storage sequence as recorded on a fast photodiode and the time window defined as t_{st}.[2] Two interesting effects can be observed. Firstly, fewer photons are retrieved and detected as the single-mode fibre represents a more restrictive filter for the original mode of the signal light. This is despite a shorter storage time which should result in less motional dephasing. Secondly, an increased number of signal photons is observed at $\approx 400\,\text{ns}$ as the signal field is extinguished which exceeds the intensity of the original signal field at the same time.

This 'flash' is a consequence of the rapid extinction of the signal field which is comparable to the lifetime of $|e\rangle$, $\tau_e = 26.24\,\text{ns}$ [215]. In the

[2] As a result of different delays between the photodiode and SPAD signals, the relative timing of the signal and control field shown is only approximate. Unlike most other storage experiments in this thesis, this example employs different control Rabi frequencies for storage and retrieval and the rise/fall times exceed the typical value of $\approx 100\,\text{ns}$ due to imperfect alignment through the EOM used for switching.

steady state before extinction of the signal light, the light field scattered by the atoms and the incident signal field interfere destructively in the forward direction [246]. If the extinction of the signal field is faster than the response time of the excited atoms, the field radiated in the forward direction from the excited atoms no longer cancels with the incident field leading to phase-shifted emission of light in the forward direction [246]. This effect is more pronounced on transitions to extremely long-lived states such as the intercombination line in Sr [247, 248] where the intensity of the emitted flash can exceed that of the incoming pulse by up to a factor of 4.

The highest efficiencies for photon storage exceeding 96% [180] have been achieved for very high optical depths > 1000 and a Λ-scheme between ground states which is much less sensitive to motional dephasing [177]. The most obvious handles to improve the storage efficiency in our experiment are increasing the optical depth via an improved dipole trap geometry (the record for Rydberg-based photon storage stands at $\approx 20\%$ [59]), reducing the atoms' temperature, e.g. by implementing Raman sideband cooling [249], and optimising the pulse shapes to achieve a fully adiabatic transfer [178] of the polaritons' photonic components into spin-waves.

4.2.1 Saturation of photon storage

As introduced in section 2.1.2, dipole blockade [20, 21] between Rydberg excitations can prevent storage of signal photons as collective Rydberg excitations provided the interactions are sufficiently strong to blockade a significant fraction of the storage volume [45, 46]. In addition, interaction-induced dephasing [45, 46, 49, 50] (section 2.3.3) enhances the suppression of photon retrieval in the original signal mode when multiple photons are stored. The influence of both effects depends strongly on the interplay between the number of incoming signal photons and the geometry of the excitation volume defined by the storage medium and optical modes of the EIT fields. An increasing number of incoming photons increases the number of collective excitations and should eventually result in a saturation

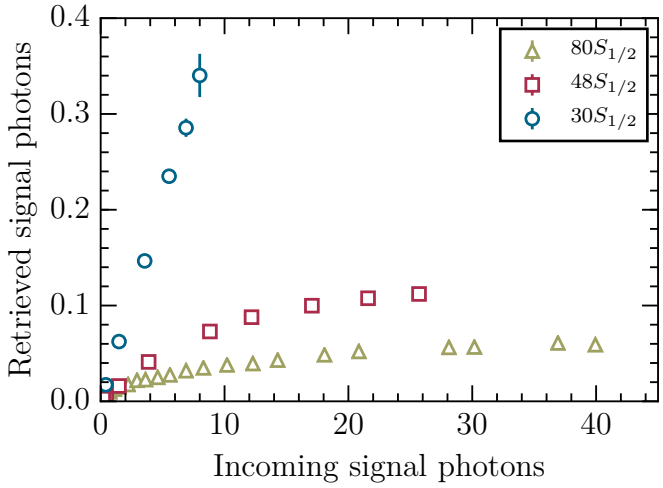

Figure 4.7: Saturation of photon storage at different $|r\rangle = |nS_{1/2}\rangle$. For $n = 30$ (blue circles), the relation between the incoming and retrieved photon numbers is linear indicating the absence of interaction during storage. For $n = 48$ (red squares) and $n = 80$ (yellow triangles), the relation becomes non-linear leading to increasingly strong saturation as a result of the dramatic scaling of the VdW interaction $C_6 \propto n^{11}$ between the stored photons. For most data points, the errorbars corresponding to statistical standard errors are smaller than the markers.

of the storage if the entire medium is blockaded. It also decreases the mean spacing between interacting excitations leading to stronger dephasing. Below, the number of retrieved signal photons is investigated as a function of the mean number of signal photons in the incoming coherent pulse for storage using Rydberg states $|r\rangle = |nS_{1/2}\rangle$ with $n = 30$, 48, and 80 ranging from weak to strong VdW interactions.

The approximately square and coherent pulse of incoming signal photons has a duration of 350 ns (400 ns for $n = 80$). The photons are stored for $t_{st} \approx 170$ ns (again excluding the fall and rise times of the control field) using control Rabi frequencies of $\Omega_C/2\pi = 18 \pm 1$ MHz for $n = 30$, 15.6 ± 0.9 MHz for $n = 48$, and 9.0 ± 0.7 MHz for $n = 80$.

Figure 4.7 presents the experimental results. For $n = 30$, the number of retrieved signal photons increases linearly with the number of incoming

photons as expected in absence of significant interactions.[3] The overall storage-and-retrieval efficiency corresponding to the ratio of retrieved and incoming photons is of the order of 4%. For $n = 48$ and $n = 80$, an increasingly strong suppression and saturation of signal retrieval is observed. As the result of the increasingly large VdW blockade $r_b^{(6)} \propto n^{11/6}$, fewer photons are required to saturate the storage, while increasingly strong interaction-induced phase-shifts $\propto C_6 \propto n^{11}$ also lead to stronger dephasing. The observed saturation of the retrieved photon number represents an analogy to early experiments on atomic Rydberg blockade [22, 23] where a saturation in the number of Rydberg excitations was observed via ion detection. It is noted that the contributions of interaction-induced dephasing and blockade cannot be distinguished here as we neither measure the time dependence of the retrieval nor the Rydberg population in general which would require ion detection. Moreover, photon-number dependent scattering of signal photons, as observed in figure 4.4, before storage also contributes to the dissipation. Recent work by Distante *et al.* [89] carried out in a much larger and thus optically thicker ensemble investigates the enhancement of Rydberg mediated optical non-linearities via photon storage in more extensive detail.

On a side note, the benefits of the high repetition rate achieved in our experimental setup are highlighted by the small errorbars (statistical standard error) [250] of the data which are invisible for most datapoints in figure 4.7, with all relative errors on the order of a few and many below 1%. Overall, the number of storage-and-retrieval cycles carried out for each datapoint within a few minutes is 2 million for $n = 30$, 4 million for $n = 48$, and 6 million for $n = 80$.[4]

[3] Note that both $r_b^{(6)}(30S_{1/2})$ and the average interatomic spacing for a density of $10^{12}/\mathrm{cm}^3$ are $\approx 1\,\mu\mathrm{m}$ such that blockade effects are weak at best.

[4] Note that the systematic errors in the photon numbers are larger due the calibration uncertainty of the detection efficiency.

4.2.2 Dephasing

To efficiently retrieve stored photons in their original optical mode, it is crucial that the phase imprinted in the collective excitation or spin wave is maintained during storage [38, 49, 50, 176]. As introduced in section 2.3.3, dipolar interactions between collective Rydberg excitations can introduce significant non-uniform phase shifts [49, 50]. These lead to a suppression in the read-out of multiple photons and can be employed to generate non-classical states of light [45, 46]. In addition, atomic motion due to the finite temperature of the storage medium represents another important dephasing mechanism (section 2.3) as the atoms move relative to the stationary spin wave during the storage time t_{st} [38, 177]. Photon storage involving Rydberg states and a ladder scheme is inherently more susceptible to motional dephasing: The wavelength difference between the signal and control light results in a much shorter period the spin-wave compared to ground-state based storage employing a Λ-scheme where the wavelengths of the EIT fields are approximately equal [38, 177].

The influence of dephasing can be observed experimentally by measuring the number of retrieved photons as a function of the storage time t_{st} (again excluding the rise and fall times of the control light). Importantly, the photons are detected behind a PM single-mode fibre which is aligned onto the optical mode of the incoming signal photons to distinguish between retrieved photons and decay of collective excitations via spontaneous emission. The incoming signal pulses have a duration of 250 ns, contain a mean of ≈ 3.7 photons and the control field couples to $|r\rangle = |80S_{1/2}\rangle$.

The results are shown in figure 4.8 and have been normalised to retrieval after $t_{st} \approx 115$ ns. With increasing t_{st}, fewer photons are retrieved as a result of both motional and interaction induced dephasing which cannot be distinguished based purely on the number of retrieved photons if the mean of the incoming signal pulse remains constant. However, the low incoming photon number in combination with overall storage-and-retrieval efficiencies of the order of $< 5\%$ (see above) suggests that in many instances

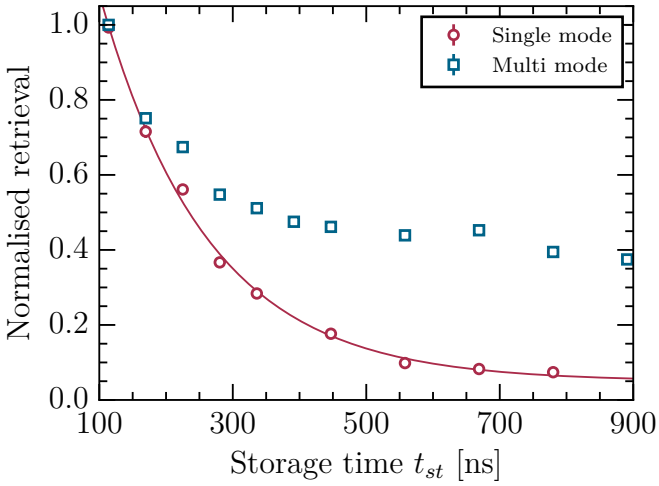

Figure 4.8: Dephasing of stored photons as function of storage time. As t_{st} increases, fewer photons are retrieved following storage due to motional and interaction induced dephasing, When using a multi- (blue squares) instead of a single-mode fibre (red circles) before the detection setup, the fraction of signal photons detected upon retrieval does not decay to zero as fluorescence from dephased Rydberg excitations is coupled into the fibre. For most data points, the errorbars are smaller than the markers.

only a single Rydberg excitation is created such that motional dephasing plays a major role. By fitting an exponential decay, we extract a storage lifetime of $1.6 \pm 0.1 \cdot 10^2$ ns.

Even though dephasing processes lead to a depletion of retrieval in the original signal mode, the Rydberg excitations are still present in the medium as the lifetime of $|r\rangle$ exceeds the storage time, $\tau_r > t_{st}$. Consequently, they are transferred to the intermediate state $|e\rangle$ when the control field is restored upon retrieval. From here they decay via spontaneous emission of a photon at the signal wavelength. Since the recollimating in-vacuo aspheric lens covers $\approx 10\%$ of the overall solid angle, a significant fraction of this perturbed retrieval can be observed by replacing the single-mode fibre before the detection system by a multi-mode fibre. A corresponding measurement of the retrieved photon number is also shown in figure 4.8. Here, the mean photon number in the signal pulse is ≈ 9.9. Again a

reduction of the retrieval with increasing t_{st} can be observed due to the increasingly strong phase mismatch. In contrast to the single-mode fibre, the normalised number of detected photons approaches a constant value significantly larger than zero. This is in agreement with the assumption that a significant fraction of the detected photons originates from perturbed retrieval and fluorescence collected into the multi-mode fibre rather than retrieved photons and highlights the importance of a single-mode fibre if one is only interested in retrieval in the unperturbed signal mode.

4.3 Non-classical states of light

One of the major motivations in Rydberg quantum optics [28] and quantum non-linear optics more generally [8] has been the creation of non-classical states of light, in particular the implementation of – ideally deterministic – narrow band single photon sources. Strong anti-bunching has been observed both via the breakdown of EIT [40] (section 4.1.2) in ensembles with very high optical depth and as a consequence of blockade [20, 21] and interaction-induced dephasing [49, 50] in photon storage [45, 46]. In the following section, we demonstrate the capability of our new setup to investigate interactions at the level of individual photons and adapt a model to simulate the effect of interaction-induced dephasing on photons stored as collective Rydberg excitations [50] which will be extended to the study of spatial correlations arising from Rydberg mediated non-local interactions between non-overlapping photons, the central result of this thesis, in the following chapter.

4.3.1 Experiment

In order to create highly non-classical states of light via Rydberg-based photon storage, it is useful to shrink the size of storage medium. This decreases the number of collective excitations that can be created inside the medium and thus number of photons which can be stored as a result

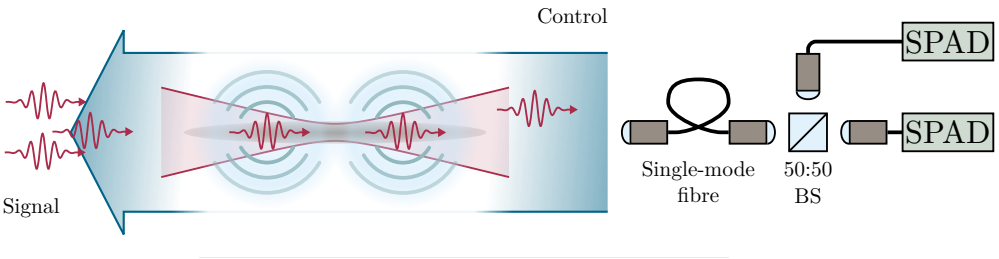

Figure 4.9: Experimental setup to measure photon statistics of retrieved light. Counter-propagating signal and control fields are focussed (signal $1/e^2$-waist radius $\approx 1.0\,\mu m$) into an elongated atomic storage medium (estimated standard deviation of Gaussian density distributions $\approx 1.5\,\mu m$ radial and $\approx 20\,\mu m$ axial) which is shrunk by evaporative cooling compared to previous measurements. A single-mode fibre aligned onto the incoming signal mode acts as a mode filter. The photons are detected using two SPADs in a HBT setup for correlation analysis.

of dipole blockade [20, 21]. It also reduces the average spacing between excitations leading to enhanced interaction-induced dephasing [45, 46, 49, 50]. The subsequent experiments are therefore carried out using a smaller ensemble of Rb atoms which is achieved by introducing 400 ms of free evaporative cooling (section 3.7.4) [244] before performing storage-and-retrival experiments to reduce the atoms' temperature and the volume they occupy. Based on the observation that signal absorption reduces significantly for $1/e^2$-waist radii exceeding $2\,\mu m$, the results of the dephasing model presented below, and the trapping frequencies, we estimate standard deviations of $\approx 20\,\mu m$ (axial) and $\approx 1.5\,\mu m$ (radial) for the cigar-shaped Gaussian atom distribution and atom numbers of order $\propto 10^3$. In addition, the signal light is focussed more strongly to a $1/e^2$-radius of $\approx 1\,\mu m$ as shown in figure 4.9.

The incoming signal pulses contain a mean of 2.2 ± 0.2 photons and have a duration of 350 ns (figure 4.10). To minimise the impact of motional dephasing on the storage-and-retrieval efficiency, the photons are stored as collective excitations to $|r\rangle = |nS_{1/2}\rangle$ for $t_{st} \approx 170\,ns$ (excluding rise/fall-time) using a control Rabi frequency of $\Omega_C/2\pi = 9 \pm 1\,MHz$. The photon

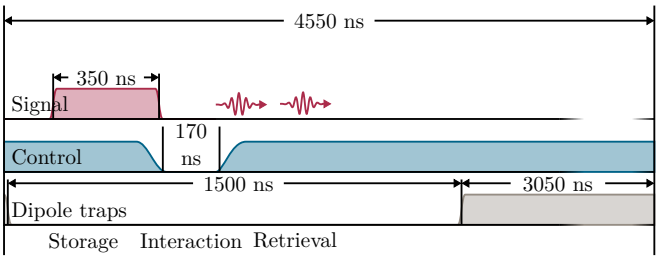

Figure 4.10: Experimental sequence to measure photon statistics of retrieved light. The coherent incoming signal pulse has a duration of 350 ns and photons are stored for $t_{st} \approx 170$ ns while the dipole trap confining the atomic storage medium is switched off. This sequence is repeated 25 000 times before a new medium is prepared in the dipole trap.

statistics of the retrieved light are analysed via HBT interferometry [236] using the photon detection setup described in section 3.7.3. All datapoints presented are obtained over 25 million storage-and-retrieval cycles where each atomic cloud is recycled 25 000 times. The cycles are repeated every 4.55 µs and the traps are turned off for 1.50 µs to perform a single cycle. Including the time required to prepare the atomic ensembles, an effective cycle rate of 33.5 kHz is achieved. In total, a single $g^{(2)}$ measurement is carried out in ≈ 13 min. Omitting the evaporation stage, $g^{(2)}$ measurements with similar statistical standard errors can be obtained in less than 5 min thanks to the high repetition rate achieved by the experimental setup.

We measure the second order correlation function

$$g^{(2)}_{A(B)} = \frac{\langle N_{A(B)} \cdot (N_{A(B)} - 1) \rangle}{\langle N_{A(B)} \rangle^2} \tag{4.1}$$

of the retrieved light [163] in a HBT measurement as we vary the interaction strength via the principal quantum number. The indices $A(B)$ indicate measurements in two distinct channels A and B (section 3.7.1) which will be used to investigate spatial correlations emerging from the non-local character of the long-range Rydberg interaction in the following chapter and are therefore investigated independently.[5] In the absence

[5]For the measurements presented here, only one channel is used at a time to avoid

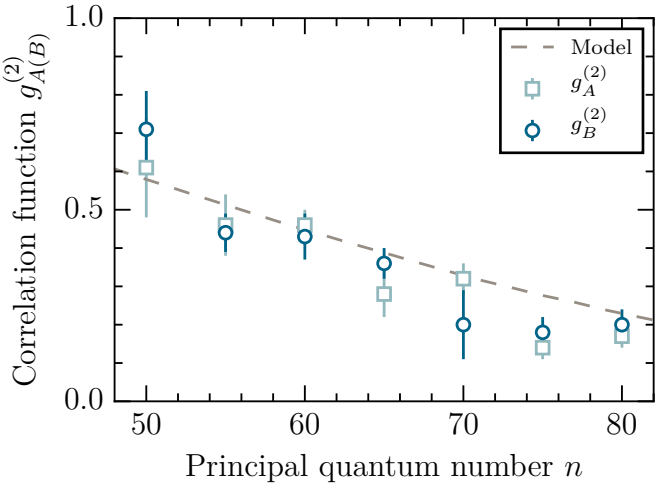

Figure 4.11: Photon statistics of retrieved signal light for storage in different $|r\rangle = |nS_{1/2}\rangle$. The correlation function $g^{(2)}_{A(B)}$ is measured independently in two different channels A and B following storage for $t_{st} \approx 170\,\text{ns}$. The suppression below 1 indicates the retrieval of non-classical light for all n investigated. The grey dashed line shows the results of the model presented in section 4.3.2.

of interactions, $g^{(2)}_{A(B)} = 1$ as the coherent nature and Poissonian photon statistics of the signal light are maintained during storage. If the blockade radius $r_b^{(6)}(nS_{1/2})$ is sufficiently large and interaction-induced dephasing is sufficiently strong, photon retrieval is limited to close to one photon and $g^{(2)}_{A(B)} < 1$ indicates the retrieval of non-classical light with sub-Poissonian photon counting statistics. If the retrieval is strictly limited to no more than a single photon, no coincidences are observed and $g^{(2)}_{A(B)} = 0$. In the correlation analysis, the entire retrieval window of a single cycle is treated as a single time bin ignoring potential correlations within the retrieved pulse. Therefore, $g^{(2)}_{A(B)}$ is equivalent to the commonly used correlation function $g^{(2)}(\tau = 0)$ [163] with a timing resolution equal to the width of the retrieval window.

The resulting suppression of higher photon numbers leads to sub-Poissonian counting statistics of the retrieved light which is indicated by

any influence of cross-channel interactions.

$g^{(2)}_{A(B)} < 1$. As shown in figure 4.11, we observe an increasingly strong suppression with n as the strength of the VdW interactions increases $C_6 \propto n^{11}$. While anti-bunching is already observed at $n = 50$, $g^{(2)}_A = 0.17 \pm 0.03$ and $g^{(2)}_B = 0.20 \pm 0.04$ for $n = 80$ indicating the retrieval of highly non-classical light, i.e. a strong suppression of simultaneous retrieval of more than one photon. Errors in the second order correlation functions $g^{(2)}$ are obtained by splitting each dataset into multiple subsets, computing $g^{(2)}$ for each subset, and finally the statistical standard error over all subsets [250].

The single photon regime could be reached by further increasing n as demonstrated by Dudin and Kuzmich [45], however we refrain from further investigating this regime as we observe a strong reduction of the retrieval efficiency for $n \geq 90$, possibly due to density induced dephasing [55, 189] as the size of a Rydberg atom's valence electron orbital becomes equivalent to the inter-atomic spacing inside the medium.

4.3.2 Dephasing model

In order to simulate the experiments above, we build on a model by Bariani *et al.* [50] which was developed to simulate the results of the first experiments on interaction-induced dephasing of photons stored as collective Rydberg excitations [45]. In principle, the model follows the description of interaction-induced dephasing given in section 2.3.3 while taking the actual experimental conditions into account. These include the spatial distribution of the cold atom ensemble, the coherent nature and thus Poissonian photon number distribution of the incoming signal pulse, and a spatially non-uniform signal mode. The latter extends beyond the work of Bariani *et al.* [50] since the signal photons cannot be considered as plane waves due to the tight (1 µm) focus of the signal mode. For comparison, Dudin and Kuzmich [45] used a much larger signal beam ($1/e^2$-waist radius 9 µm in a shorter storage medium (15 µm). More complex spatial geometries are also included in anticipation to simulate interaction-induced phase shifts across adjacent, spatially independent photon channels described in the

subsequent chapter (section 5.6). The simulations have been implemented in joint work with P. Huillery and T. Ilieva.

Effect of interaction-induced dephasing on photon statistics

The underlying approach of the model is to calculate $g^{(2)}_{A(B)}$ by comparing the overlap between the initial collective ground state $|G\rangle_A$ of the ensemble (equation 2.31) and the collective ground state after a photon storage-and-retrieval cycle $|G'(t_{st})\rangle_A$ (equation 2.37) where the phase relations between individual atoms have been modified following interaction. The overlap following storage of exactly ν photons is given by

$$\begin{aligned} D_A^{(\nu)} &= \frac{\langle G|_A G'(t_{st})\rangle_A}{\langle G|_A \left(S_A\right)^\nu \left(S_A^\dagger\right)^\nu |G\rangle_A} \\ &= \frac{\langle G|_A \left(S_A\right)^\nu U_A\left(t_{st}\right) \left(S_A^\dagger\right)^\nu |G\rangle_A}{\langle G|_A \left(S_A\right)^\nu \left(S_A^\dagger\right)^\nu |G\rangle_A}. \end{aligned} \tag{4.2}$$

For two stored photons, $\nu = 2$, we consequently obtain

$$D_A^{(2)} = \frac{\sum_{j,k>j} \left(\epsilon_A\left(\vec{r}_j\right)\epsilon_A\left(\vec{r}_k\right)\right)^2 e^{-iV_{jk}t_{st}/\hbar}}{\sum_{j,k>j} \left(\epsilon_A\left(\vec{r}_j\right)\epsilon_A\left(\vec{r}_k\right)\right)^2}. \tag{4.3}$$

The overlap $D_A^{(\nu)}$ determines the probability to retrieve signal photons in the original mode, i.e. $D_A^{(\nu)} = 1$ in absence of interaction induced dephasing,[6] and can be related to an experimentally accessible quantity, such as $g_A^{(2)}$, via the probabilities to find $\nu = 1$ or 2 photons in the incoming signal pulse. So far, we have considered storage of exactly ν photons. Since the incoming signal pulses are classical and represent not Fock, but coherent states, the number of incoming photons follows a Poisson distribution [163]. Furthermore, the number of signal photons stored in an individual experiment varies as a result of imperfect storage.

[6] Motional dephasing also reduces the overlap, but is independent of the stored photon number ν. It is therefore ignored as its effects cancel when calculating $g_A^{(2)}$ according to equation 4.6.

Therefore, the ensemble is considered in a superposition of collective states with different numbers of stored photons ν,

$$|R\rangle_A = \sum_\nu c_\nu \, |R^{(\nu)}\rangle_A \tag{4.4}$$

where the coefficients c_ν describe their distribution. Since the number of photons which can be detected simultaneously in a HBT interferometer, is limited to two, we only investigate second order correlations and consider storage of up to two photons as collective excitations

$$|R\rangle_A = \sum_{\nu \leq 2} c_\nu \, |R^{(\nu)}\rangle_A. \tag{4.5}$$

This truncation which ignores detection of e.g. two photons when three are stored, is further justified by the low mean of incoming photons and overall efficiencies which are of orders 2 and a few 0.01, respectively. This thus suggests that storage of three or more photons represents a rare and negligible event.

By describing the state of the ensemble using a coherent superposition state rather than a density matrix [50, 251], it is assumed that a signal pulse which contains ν photons with probability $|c_\nu|^2$, is mapped into $|R\rangle_A$ and no decoherence occurs during the storage process. Neglecting decoherence due to Rydberg mediated interactions during the process, e.g. scattering of a photon within the volume blockaded by another which would lead to stronger localisation of the excitation [172], is reasonable because the number, and consequently spatial density, of excitations considered in the model is low (Poissonian distribution with $\langle\nu\rangle = 0.01$, see below). We also neglect decay of Rydberg excitations as their lifetime is long compared to t_{st}. Any processes that are independent of ν, i.e. those responsible for the finite efficiency of the storage protocol, are accounted for by a reduced mean $\langle\nu\rangle$ of excitations compared to photon numbers in the experiment. To model the influence that the interaction phase acquired during t_{st} has on $g_A^{(2)}(B)$, only the reduction in the probability for phase matched retrieval

of two photons compared to the non-interacting case given by $|D_A^{(2)}|^2$ is required.

The probabilities to store one or two photons initially are respectively given by $|c_1|^2$ and $|c_2|^2$. While a single stored photon is not affected by interaction-induced dephasing, the probability to retrieve two stored photons in the original signal mode is given by $|D_A^{(2)}|^2$. Therefore, we obtain the second order correlation function $g_A^{(2)}$ as [50]

$$g_A^{(2)} = \frac{2|D_A^{(2)}|^2|c_2|^2}{\left(|c_1|^2 + 2|D_A^{(2)}|^2|c_2|^2\right)^2}. \tag{4.6}$$

Simulation procedure

In practice, the simulation process can be broken up into the following steps:

1. Create a cigar-shaped ensemble of $\mathcal{N}_A$ randomly positioned cold Rb atoms with a Gaussian density profile based on experimentally determined cloud parameters to obtain a set of atom positions $\{\vec{r}_1, \ldots, \vec{r}_{\mathcal{N}_A}\}$.

2. Calculate $D_A^{(2)}$ for the given set of positions and the interaction potential V_{jk} ($V_{jk} = C_6(|nS_{1/2}\rangle)/r_{jk}^6$ for VdW interactions and $|r\rangle = |nS_{1/2}\rangle$).

3. Using equation 4.6, determine $g_A^{(2)}$ based on the result for $D_A^{(2)}$ and the coefficients c_ν for a specific initial photon number distribution.

4. Repeat the previous steps for multiple randomly generated ensembles and average the results to obtain $g_A^{(2)}$.

Simulation parameters and results

In principle, the model does not include any free parameters. Some experimental parameters however are not precisely known and are subsequently treated as adjustable. This concerns, in particular, the number of atoms

$\mathcal{N}_A$ in and dimensions of the atomic ensemble, as well as the storage time t_{st} which is chosen to exclude transient effects during the rise-/fall-time of control field. In addition, we can only measure the number of signal photons that are retrieved or the mean of the incoming signal pulse rather than the number of photons that is initially stored.

The results presented in figure 4.12 (a), are obtained using the following parameters. The atomic ensemble contains $\mathcal{N}_A = 1000$ atoms and has radii of 21 µm along and 1.5 µm perpendicular to the propagation axis of the signal and control light fields. The signal light has a $1/e^2$-waist radius of 1 µm at the centre of the ensemble. The initial signal photon number follows a Poissonian distribution with mean $\langle\nu\rangle = 0.01$ such that the probabilities correspond to

$$|c_\nu|^2 = \frac{1}{\nu!} e^{-\langle\nu\rangle} \langle\nu\rangle^\nu. \tag{4.7}$$

The storage time is varied between $t_{st} = 100\,\text{ns}$ and $t_{st} = 1070\,\text{ns}$. For each datapoint, 10 instances of the simulation are taken into account. As expected, the anti-correlation in the photon retrieval increases with increasing interaction strength and for longer storage and thus interaction times. The results for $t_{st} = 170\,\text{ns}$ are also in good agreement with the data in figure 4.11.

Figure 4.12 (b), shows simulation results for the correlation function $g^{(2)}_{A(B)}$ for different lengths (standard deviation of the Gaussian atomic density distribution along the lens axis) of storage medium between 5 and 41 µm. The atom number $\mathcal{N}_A = 1000$ remains fixed. The anti-correlations become stronger as the medium becomes more compact and the average inter-atomic spacing decreases. Consequently, the effect of interaction-induced dephasing increases due to the $1/r^6$-dependence of the VdW-potential. Since we cannot directly image the length of the atomic medium, the results of these simulations are an important indication of the length of the storage medium.

As both $\langle\nu\rangle$ and $\mathcal{N}_A$ are varied to verify whether our assumptions are

reasonable, we find that the results for $g_A^{(2)}$ are robust against changes in both values as long as the condition $\langle\nu\rangle \ll 1 \ll \mathcal{N}_A$ is satisfied. This implies that the geometry of the atomic ensemble and signal beams are the most important factors affecting the results, besides, of course, the interaction strength itself set by the choice of $|r\rangle$.

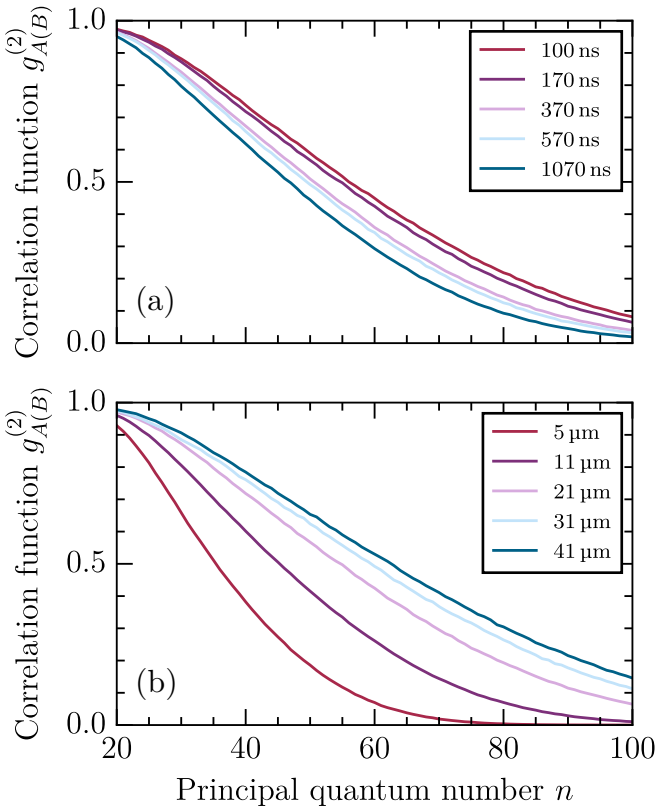

Figure 4.12: Simulation of photon statistics of retrieved light. (a) Correlation function $g^{(2)}_{A(B)}$ as a function of the principal quantum number of $|nS_{1/2}\rangle$ for different storage times $t_{st} = 100$ to 1070 ns. The length of the storage medium is fixed at 21 µm (standard deviation of Gaussian atom distribution). (b) Correlation function $g^{(2)}_{A(B)}$ for different lengths of the storage medium length and $t_{st} = 170$ ns.

5 Contactless quantum non-linear optics

The ability of dipolar Rydberg interactions to strongly modify the optical response of a cold atomic medium as demonstrated in the previous chapter and by a plethora of other experiments to date [26, 40, 41, 45–47, 53–57, 59, 89, 90, 181, 252, 253], results from their long-range character [18, 19]. The arising highly 'non-local' or long-range optical non-linearity [42–44] enables few or even single photons mapped into Rydberg excitations to modify the optical response over µm-sized volumes encompassing many atoms [28, 29]. To date, experiments in Rydberg non-linear optics use overlapping optical modes and a common medium.[1] However, the underlying concept to coherently and reversibly map photons into strongly interacting quanta removes the need for a common medium if the interaction can be mediated through free space. Dipolar interactions between Rydberg excitations are mediated by virtual microwave photons and can thus occur as long as the dipoles and media are confined within the microwave near-field. This is of the order of 1 cm and thus four orders of magnitude larger than the sub-µm optical diffraction limit which defines the minimum diameter of the optical modes.[2]

The following chapter describes the experimental demonstration of effective photon interactions mediated through free space. The photons

[1] An exception is the work by Thompson *et al.* [90] which demonstrates photon hopping between two parallel modes which was published after completing the work presented in this thesis.

[2] In order to achieve significant interaction strength, separations on the order of 10 µm are realistic.

are stored as collective Rydberg excitations in media separated by more than 10 µm and propagate in non-overlapping optical modes. This chapter discusses the underlying concept (section 5.1), interaction mechanisms (section 5.2) and their effect on photon correlations (section 5.3), as well as details on the experimental procedure (section 5.4). The non-local interactions manifest themselves in a modification of cross-correlations between modes in the retrieved photon statistics (section 5.5). They are tunable by changing either the Rydberg state used for storage or the channel separation. An adapted version of the dephasing model presented in section 4.3.2 (section 5.6) shows good agreement with the data.

Besides the author, P. Huillery, S. W. Ball, and T. Ilieva contributed to the experiments presented in this chapter. The work was supervised by C. S. Adams and M. P. A. Jones.

This chapter is in part based on the following publications [85, 88]:

- H. Busche, S. W. Ball, and P. Huillery, "A high repetition rate experimental setup for quantum non-linear optics with cold Rydberg atoms", Eur. Phys. J. Spec. Top. **225,** 2839–2861 (2016).
- H. Busche, P. Huillery, S. W. Ball, T. V. Ilieva, M. P. A. Jones, and C. S. Adams, "Contactless non-linear optics mediated by long-range Rydberg interactions", Nat. Phys., to appear (2017).

5.1 Concept

Our approach to implement interactions between photons in spatially separated media is illustrated in figure 5.1. Two strongly interacting photonic quantum channels are realised side-by-side separated by an adjustable distance d in analogy to experiments studying interactions between individual Rydberg atoms [24, 25, 72, 73, 86, 254] and collectively encoded ensemble qubits [87] in optical tweezers. The experimental setup is presented in section 3.7 and duplicates the geometry used in the previous chapter: The channels each consist of a cigar-shaped ensemble of ultra-cold atoms serving

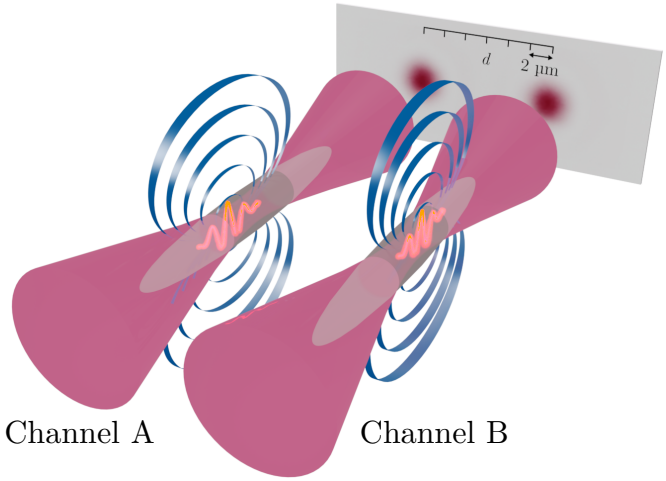

Figure 5.1: Implementation of spatially separated, strongly interacting photon channels. Two modes of signal light are tightly focussed into microscopic atomic media where photons are stored as collective Rydberg excitations. During storage the strong dipolar interactions (in this work VdW interactions) between Rydberg atoms are mapped onto the photons.

as media in which signal photons propagating in tightly focussed optical modes are stored as collective Rydberg excitations using EIT [32]. While stored, the photons effectively interact via dipolar Rydberg interactions [18, 19, 27, 28, 45, 46] (section 2.3). In the context of this thesis, a common EIT control field used for both channels only permits simultaneous storage and retrieval in the same Rydberg state $|r\rangle$ for a proof of principle experiment. However, the setup can be easily adapted for independent storage using different Rydberg states in each channel by addressing them with individual, more tightly focussed control beams. The concept could also be scaled to more than two channels, e.g. using freely configurable optical tweezer arrays [96, 98, 204, 255], or even cold atoms interfaced with integrated optical waveguides [74] or optical fibres [256, 257].

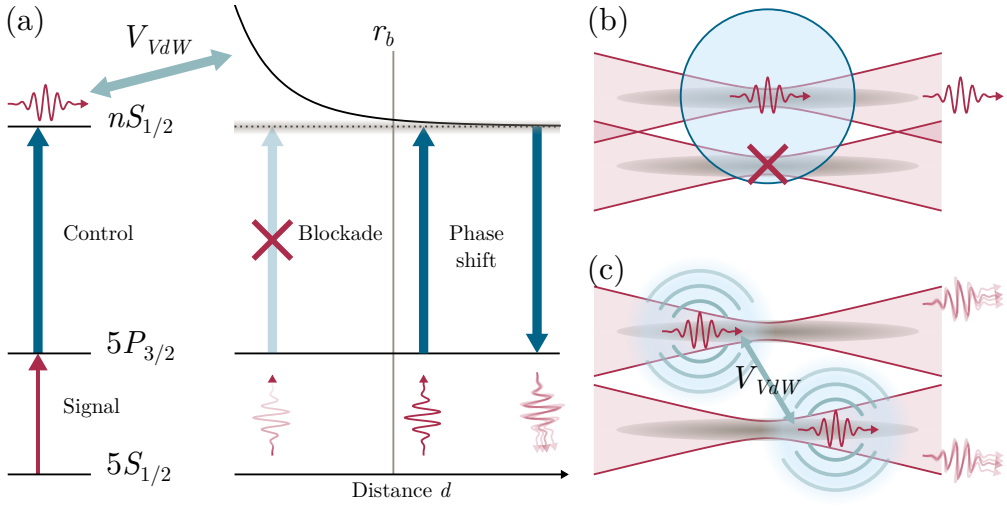

Figure 5.2: Effective long-range interactions between photons. (a) Two regimes can be distinguished. For a channel separations $d < r_b$, simultaneous storage of photons as collective Rydberg excitations in both channels is prevented (b). For $d > r_b$, the atoms contributing to the collective excitation acquire interaction-induced phase shifts which distort the photons' retrieval modes (c).

5.2 Long-range interactions between photons

When photons are stored as collective Rydberg excitations in spatially separated channels and using states that exhibit VdW interactions, two different interaction mechanisms can be distinguished as illustrated in figure 5.2. If the blockade radius asscociated with the storage process [122] exceeds the channel separation, $d < r_b$, excitation blockade [20, 21] directly translates into 'storage blockade' (sections 2.1.2 and 2.3.2) and prevents simultaneous photon storage in analogy to experiments between two spatially separated individual atoms [24, 25] and within a single channel [45, 46] (section 4.2.1). However, at channel separations $d > r_b$, the effect of interactions changes profoundly compared to the single atom case. The storage protocol imprints the phase of the signal photons (or more generally the EIT light fields) in the collective spin-wave which is crucial to ensure

retrieval in the original mode [38, 175, 176] (section 2.3). Hence, stored photons have a well-defined phase and are sensitive to interaction-induced phase shifts. Within a single channel, this results in dephasing [49, 50] and reduced retrieval of multi-component states of the light field [45, 46] as discussed and observed in sections 2.3.3 and 4.2.2. Similarly, VdW-interactions also induce phase-shifts between stored photons in spatially separated channels whose effect can be more subtle as will be shown below.

The interaction mechanisms discussed above, blockade and interaction-induced phase shifts, would also apply if the photons were stored as collective excitations in two different, dipole-coupled Rydberg states which interact via resonant dipole interactions [46, 51] (section 2.1.1). However, an additional interaction mechanism needs to be taken into account: Excitation hopping where excitations switch states via the exchange of virtual microwave photons. This has been directly observed between both individual atoms [138] and polaritons [90]. A similar process occurs at Förster resonances [130, 131] where non-radiative energy transfer enables pairs of Rydberg atoms to flip between pair states of the same energy [133, 137, 139]. A non-local change in the optical response of a Rydberg EIT medium has been observed as the result of FRET [132] between Rydberg excitations in the EIT medium and a background of Rydberg impurities [64]. Resonant dipole interactions are not considered below as they are beyond the scope of this thesis, but offer exciting prospects for future experiments. Exchange interactions enable quantum simulation of spin systems [138] and non-radiative energy transfer [64, 133], as well as robust, symmetry-protected $\pi/2$-phase shifts [90] in Rydberg quantum optics. Conditional blockade of a microwave 2π-rotation applied to a stored photonic qubit induced by resonant dipole interactions constitutes the fundamental interaction mechanism of a proposal to implement gates for optical QIP [70].

5.2.1 Storage blockade

The effect of excitation blockade between Rydberg atoms [20, 21] on photon storage is trivial in the simple case where the spatial extend of the media and channel separation d are small enough such that a single excitation in one medium entirely blockades both: Only one photon can be stored in either of the channels. This behaviour has been observed between collectively encoded ensemble qubits [87], but not stored photons.

If the channel separation is $d < r_b$, yet the length of the storage media exceeds r_b, storage of multiple photons cannot be entirely prevented. Instead, the number of photons stored in each channel is only reduced by partial blockade. The ability to store multiple photons as collective Rydberg excitations has important implications with regard to the interaction mechanisms at play. While their interaction strength does not exceed the storage bandwidth [122], two collective excitations still experience interactions beyond r_b which introduce position dependent phase shifts as explained in section 2.3.3 for a single and below for multiple channels. This regime could be of interest to investigate the emergence of spatial correlations between stored photons [48, 51] along the media, in analogy to those observed between collective excitations [98, 149].

In this thesis, interactions in the regime $d < r_b$ are not investigated for the following reasons. Firstly, the elongated atomic density distribution of the storage media implies that we cannot explore the fully blockaded regime. Hence, simultaneous storage may occur in both ensembles and interaction-induced phase shifts still have an important influence. Secondly, we start to observe increased cross-talk in signal absorption between channels if the channel separation is below $d < 10\,\mu\text{m}$ (section 3.7.4). If we increase r_b via the principal quantum number of $|r\rangle = |nS_{1/2}\rangle$, density-induced dephasing (section 2.3.4) reduces the storage efficiency [55, 189]. The blockaded regime is, however, of particular interest for technical applications since it allows a discrete change the optical response of the blockaded volume conditional on the presence or absence of a single stored photon in quantum

optical devices such as switches [55], transistors [56, 57], or phase shifters [59]. Its exploration is therefore an important objective for future work.

5.2.2 Interaction-induced phase shifts

Unlike collective Rydberg excitations more generally [52, 87, 98, 99, 152, 154], photons stored as collective excitations $|R^{(\nu)}_{A(B)}\rangle = (S^{\dagger}_{A(B)})^{\nu}\,|G\rangle_{A(B)}$ are inherently sensitive to interaction induced phase shifts. Imprinting the signal field amplitude $\epsilon_{A(B)}(\vec{r}_{j(k)})$ and phase $\phi_{A(B)}(\vec{r}_{j(k)})$ in the spin-wave can be described by the creation operator (ignoring interaction and propagation dynamics during the storage process)

$$S^{\dagger}_{A(B)} = \frac{1}{\sqrt{\sum_{j(k)} \epsilon_{A(B)}(\vec{r}_{j(k)})^2}} \sum_{j(k)} \epsilon_{A(B)}(\vec{r}_{j(k)}) e^{i\phi_{A(B)}(\vec{r}_{j(k)})}\,|r_{j(k)}\rangle_{A(B)}\,\langle g_{j(k)}|_{A(B)} \tag{5.1}$$

which converts photons into collective excitations (compare equation 2.32). This ensures that photons are retrieved in their original modes in absence of interactions. If multiple photons are stored, interactions induce spatially non-uniform phase-shifts which alter the retrieval modes and reduce retrieval in the unperturbed mode [45, 46] (sections 2.3.3 and 4.2.2).

Conceptually, interaction-induced phase shifts between stored photons in adjacent channels can be described in a similar fashion as within a single channel by considering the influence of pairwise interactions between the individual atoms on the time evolution of the collective states and photon retrieval. However, the spatial separation of the channels requires a modified description of the two-channel collective state as geometry imposes a minimum spacing slightly below d between interacting atom pairs.

Since storage itself is independent in each channel, we consider the initial collective states $|R^{(\nu)}\rangle_A$ and $|R^{(\mu)}\rangle_B$ (equation 2.33) following storage of ν photons in channel A and μ photons in channel B separately, thereby

neglecting potential blockade effects.[3] The combined collective state of both channels is thus

$$|R^{(\nu,\mu)}\rangle_{AB} = |R^{(\nu)}\rangle_A \otimes |R^{(\mu)}\rangle_B \,. \tag{5.2}$$

The time evolution of $|R^{(\nu,\mu)}\rangle_{AB}$ in the presence of a pairwise VdW interaction $V_{jk} = V_{VdW}(\vec{r}_j, \vec{r}_k) = C_6/|\vec{r}_j - \vec{r}_k|^6$ during a storage time t_{st} is described by

$$U_{AB}(t_{st}) = U_A(t_{st}) + U_B(t_{st}) + \sum_{j\in A, k\in B} e^{-iV_{jk}t_{st}/\hbar} |r_j\rangle_A \langle r_j|_A \otimes |r_k\rangle_B \langle r_k|_B. \tag{5.3}$$

Here, $U_{A(B)}(t_{st})$ remain the same as in the single channel case (equation 2.33) as interactions within a channel are not affected by the presence of another, and absent if only one photon is stored per channel. Accordingly, the collective two channel state evolves as

$$|R^{(\nu,\mu)}(t_{st})\rangle_{AB} = U_{AB}(t_{st}) \, |R^{(\nu,\mu)}\rangle_{AB} \,. \tag{5.4}$$

The cross channel interaction induces an additional phase $V_{jk}t_{st}/\hbar$ between individual atoms $j \in A$ and $k \in B$ and entangles the atoms in the collective state since V_{jk} is spatially non-uniform. The fraction of photons retrieved in the original signal modes decreases as t_{st} increases as increasingly strong phase shifts reduce the overlap of $|R^{(1,1)}(t_{st})\rangle_{AB}$ with the initial state $|R^{(1,1)}\rangle_{AB}$. Figure 5.3 shows the phase acquired as a result of interactions between individual ^{87}Rb atoms per 100 ns as a function of their separation $r_{jk} = |\vec{r}_j - \vec{r}_k|$ for a selection of Rydberg states $|r\rangle = |nS_{1/2}\rangle$ with principal quantum numbers between $n = 50$ and 90.

[3] Neglecting Rydberg blockade is justified if the channel separation does not fall below the blockade radius, $d > r_b$, and/or if the number of signal photons stored in each channel is sufficiently low to avoid saturation of the storage medium.

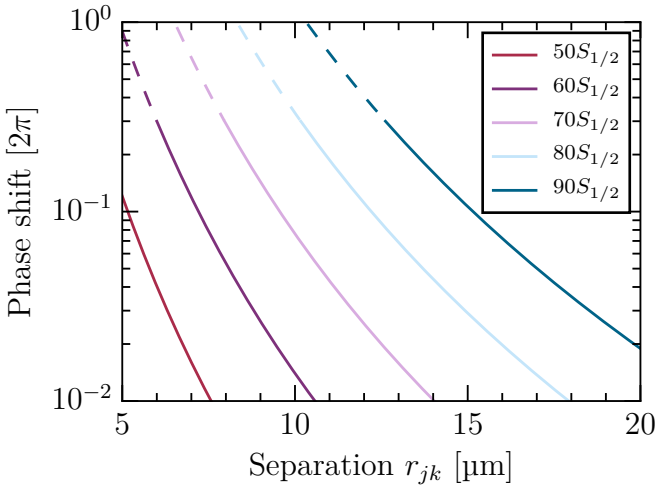

Figure 5.3: Interaction induced phase shift between two individual atoms separated by r_{jk}. VdW-induced phase shifts accumulated per 100 ns interaction time are shown for atom pairs in $|nS_{1/2}\rangle$. The dashed lines indicate where $r_{jk} < r_b^{(6)}(nS_{1/2})$ for a linewidth of 7 MHz.

5.3 Spatial photon correlations

Since interaction-induced phase-shifts lead to reduced photon retrieval [45, 89] (section 4.2.1), one might expect that cross-channel interactions can be observed straightforwardly as fewer photons are retrieved per channel. However, as the number of retrieved and detected photons per storage cycle is low (of order 0.001) no more than a single photon is detected in most instances. The number of storage cycles where at least one photon is stored in both channels pales in comparison such that the reduction in overall retrieval does not exceed fluctuations between datasets.

Therefore, it is important to analyse statistical correlations instead of comparing absolute numbers or rates. Without cross-channel interactions, photon retrieval in both signal modes is expected to be uncorrelated. That is, the probability to simultaneously detect at least one photon in each channel per storage cycle corresponds to the product of the probabilities to detect at least one photon in each of the individual channels independently. If cross-channel interactions suppress simultaneous retrieval in the

unperturbed modes, the probability for simultaneous detection drops.

In order to quantify the correlations, we use a second order temporal inter-channel (or spatial) correlation function which is in its most general form

$$g^{(2)}_{AB}(\tau) = \frac{\langle N_A(t_A) N_B(t_B)\rangle}{\langle N_A(t_A)\rangle \langle N_B(t_B)\rangle} \tag{5.5}$$

where $N_A(t_A)$ and $N_B(t_B)$ are the photon numbers detected at times t_A and t_B and $\tau = t_A - t_B$. It can be interpreted as a variant of the common, general definition of the second order correlation function $g^{(2)}(t_A, \vec{r}_A, t_B, \vec{r}_B)$ [163] where the two detector positions $\vec{r}_{A(B)}$ correspond to suitable locations in channels A and B. The averages are taken over all store-and-retrieve cycles within a dataset. In this work, we are only interested in whether photons are retrieved in both channels over the entire retrieval window, but not more detailed temporal correlations within the retrieved pulses. Hence, the entire retrieval window is treated as a single time bin. Since we are neither interested in determining $g^{(2)}_{AB}$ across independent storage cycles which are intrinsically uncorrelated, the time-dependence can be dropped from the notation altogether:

$$g^{(2)}_{AB} = \frac{\langle N_A N_B\rangle}{\langle N_A\rangle \langle N_B\rangle}. \tag{5.6}$$

Here, N_A and N_B are the number of photons retrieved in each channel over the entire retrieval window.

The values which $g^{(2)}_{AB}$ takes, are analogous to the single channel function $g^{(2)}_A$ (section 4.3.1): For anti-correlated retrieval, fewer coincidences are observed than expected and $g^{(2)}_{AB} < 1$ with $g^{(2)}_{AB} = 0$ if simultaneous retrieval in both channel is fully suppressed. For correlated retrieval, more coincidences are observed than expected based on the single channel retrieval probabilities and $g^{(2)}_{AB} > 1$. Finally, one obtains $g^{(2)}_{AB} = 1$ if retrieval is uncorrelated between channels.[4]

[4]Note that unlike in the single channel case, these values alone do not necessarily

In future experiments, temporal correlations between channels within the retrieval window may give insights into spatial correlations between stored photons, similar to experiments with individual atoms [98, 149]. Equally, it could be of interest to map out the modified retrieval modes by searching for correlations ($g^{(2)}_{AB} > 1$), i.e. for deflected modes as shown in figure 6.1.

5.4 Experimental implementation

In principle, the experimental procedure for dual-channel experiments does not differ from single channel experiments presented in section 4.2. Figure 5.4 shows the relevant EIT transitions in ^{87}Rb (a), the storage sequence employed in all experiments presented subsequently (b), and the experimental geometry (c). The steps – preparation of the atomic media, storage-and-retrieval experiments, and photon detection – are summarised below.

Production of the atomic media

The most important difference in the preparation of two side-by-side atomic ensembles in dual-channel experiments compared to a single channel is to ensure the absence of cross-talk between channels. That is to avoid overlap of the signal mode of channel A with the medium of channel B or vice versa. Consequently, strong spatial confinement of the atoms is necessary as the channel separation d is imposed by the interaction strength between Rydberg excitations and the diffraction limited size of the signal foci. To reduce the temperature and thus the volume occupied by the atoms, a 400 ms stage of free evaporative cooling [244] is applied as outlined in section 3.7.4. Figure 5.5 compares the transmission of signal light for $d = 10\,\mu$m and 11 µm in both channels when either both media or only

contain information whether the nature of the retrieved light is classical or quantum. To obtain this information, simultaneous measurements of $g^{(2)}_{A(B)}$ are needed in addition.

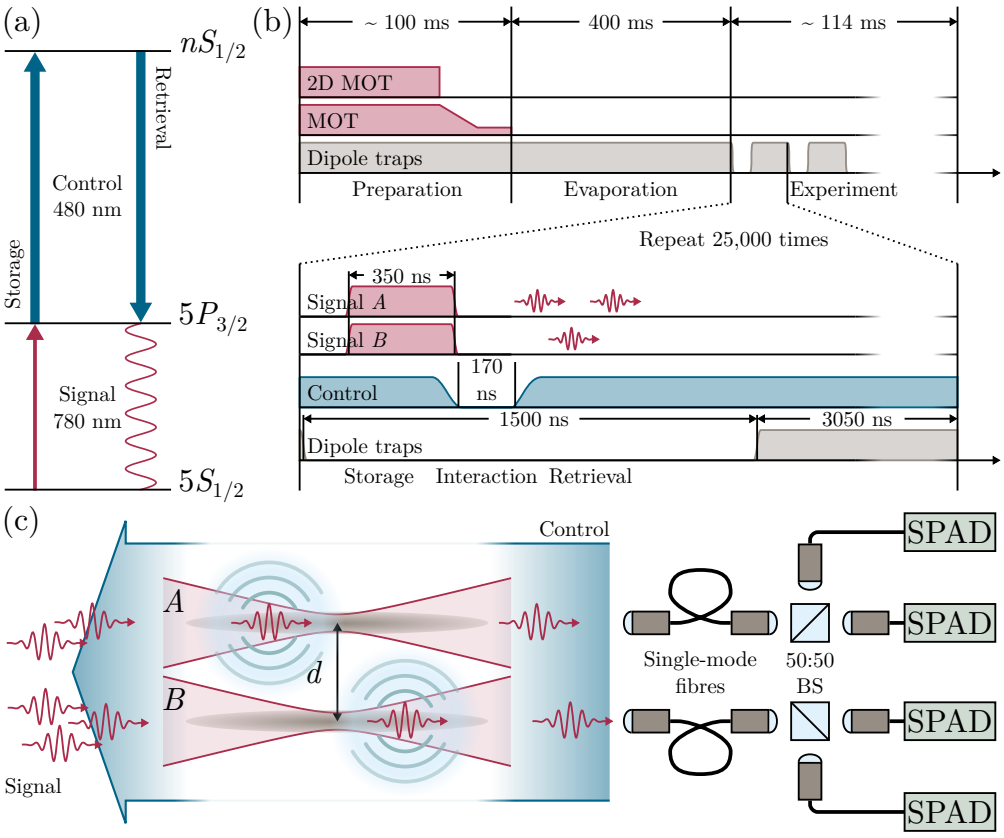

Figure 5.4: Experimental approach to observe photon interactions between non-overlapping channels. (a) Level scheme of ^{87}Rb transitions relevant for EIT based photon storage. (b) Sequence for preparation of the atomic media and the photon storage/retrieval protocol. (c) Overview of experiment. The signal modes are focussed into the atomic media with waist radii ($1/e^2$) of 1 µm. The control field is counter-propagating and addresses both channels. Photons retrieved in the original signal modes are detected using SPADs in HBT configuration located behind single mode fibres.

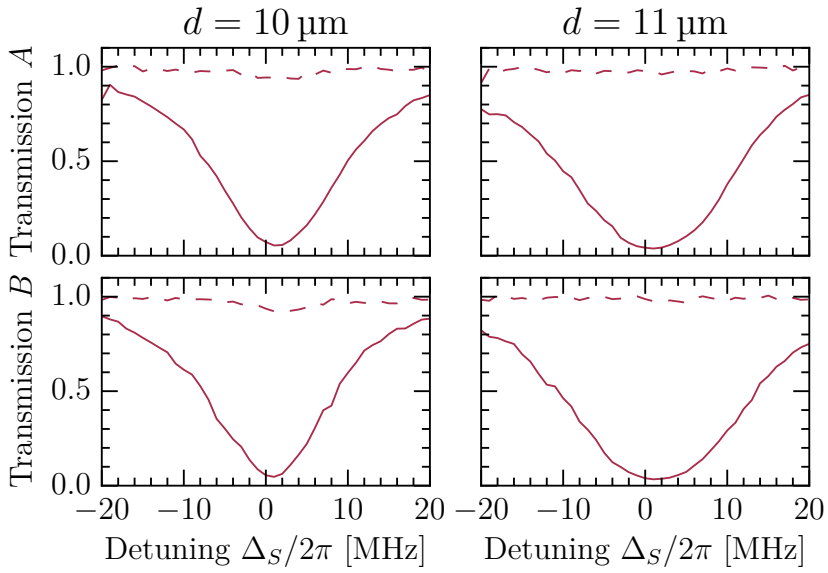

Figure 5.5: Cross-talk between photon channels. Transmission of signal light in channels A (top) and B (bottom) for separations of $d = 10\,\mu m$ (left) and $11\,\mu m$ (right). For the spectra shown as solid lines, both atomic media are present. For the dashed spectra, only the medium of the other channel is present. Minimal cross-talk is observed for $d = 10\,\mu m$, but absent for $d \geq 11\,\mu m$.

the medium of the other channel is present. While a slight reduction of transmission $< 5\%$ is observed for $d = 10\,\mu m$,[5] cross-talk typically vanishes for $d \geq 11\,\mu m$. This emphasises that both channels are spatially independent in the experiments presented below.

Following evaporation, on the order of $\propto 10^3$ atoms are contained in each of the cigar shaped, thermal atomic ensembles with estimated radii (standard deviations of Gaussian atom distribution) of $\approx 20\,\mu m$ along and $\approx 1.5\,\mu m$ perpendicular to the lens axis. As mentioned in section 3.7.4, these values are estimates.

[5] Cross-absorption is likely to occur far away from the foci in the wings of the atom clouds due to the strong divergence of the tightly focussed signal beams.

Photon storage

Like the preparation of the atomic media, the EIT-based photon storage protocol [32, 38, 39, 170] itself remains the same as in the single channel case (figure 5.4 b): While signal pulses propagate through the media under EIT conditions, the Rabi frequency Ω_C of the control field is reduced to zero to store signal signal photons and subsequently restored to its original value for photon retrieval (sections 2.3 and 4.2). The signal photons are resonant with the $|g\rangle = |5S_{1/2}, F = 2, m_F = 2\rangle \rightarrow |e\rangle = |5P_{3/2}, F' = 3, m'_F = 3\rangle$ transition in ^{87}Rb and the control field couples $|e\rangle$ to a Rydberg state $|r\rangle = |nS_{1/2}\rangle$, see figure 5.4 (a). The experimental geometry is shown in figure 5.4 (c). The signal modes of both channels, focussed to $1/e^2$-radii of 1 µm, are counter-propagating with a common control field which is aligned such that both channels are addressed simultaneously and experience approximately the same Rabi frequency Ω_C. Signal and control fields have opposite circular polarisation and a magnetic field is applied along the lens axis to define the quantisation axis (section 3.7).

The control Rabi frequency Ω_C is calibrated by measuring Autler-Townes spectra [164] (compare section 4.1.1). To ensure Ω_C is approximately equal in both channels, the control field is aligned such that the splitting is equal in both channels. Since insufficient control power is available to observe strong Autler-Townes splitting for calibration at high n, the calibration is carried out at $n = 30$ and values for Ω_C at higher principal quantum numbers are obtained by rescaling the values accordingly.

The details of the experimental sequence shown in figure 5.4 (b) can be summarised as follows. Following initial preparation of the atomic ensembles, they are optically pumped into $|g\rangle$. Subsequently, 25 000 storage and retrieval experiments are carried out before reloading the optical traps. A single cycle lasts 4.55 µs during which the traps are turned off for 1.50 µs, to carry out one storage-and-retrieval experiment: Weak coherent signal pulses with a duration of 350 ns and mean photon numbers of 2.2 ± 0.2 are sent into both channels. The control field $\Omega_C \rightarrow 0$ is ramped to zero

to store signal photons while they propagate through the media. The storage time is approximately $t_{st} \approx 170\,\text{ns}$, excluding the fall and rise time of the control field. Including the preparation of the atom clouds, this corresponds to an effective cycle rate of 33.5 kHz. Overall, the storage and retrieval sequence is repeated 25 million times for each datapoint presented below. In the experiments, we typically retrieve between 1% to 3% of the signal photons initially sent into the experiment. The efficiency is limited by strong photon interactions within the same channel [45, 46] (chapter 4), the limited optical depth and length of the media, and motional dephasing [177] due to the finite temperature of the atomic ensembles (section 2.3).

Photon detection

Following storage, the retrieved photons are detected using the dual-channel setup described in section 3.7.3: Behind the storage media photons re-emitted into the two unperturbed signal modes are coupled into separate PM single-mode fibres behind each of which two single photon counters are arranged as HBT [236] interferometers to analyse the retrieved photon statistics. Here, the retrieved light is coupled into single- rather than multi-mode fibres as these allow to clearly distinguish between signal photons re-emitted into their original modes from those retrieved into modified modes as a result of interaction-induced phase shifts.

Figure 5.6 shows examples of the incoming and retrieved signal pulses for both channels and $n = 80$. While slight cross-talk between channels is observed in the transmitted signal light for $d = 10\,\mu\text{m}$ (figure 5.5), no cross-storage occurs between channels, in the sense that no retrieved signal photons above dark counts are detected in channel B if only medium A is present and vice versa.

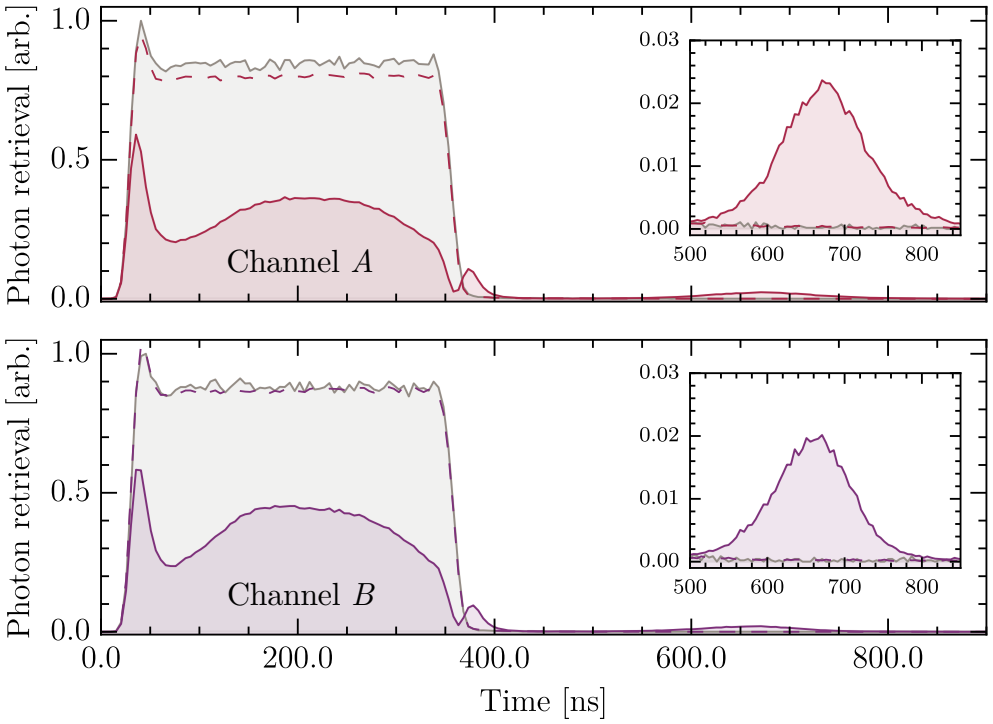

Figure 5.6: Photon storage in side-by-side photon channels. The solid lines show the detected photons during storage and retrieval when both atomic media are present. The dashed lines show the detected photons if the medium of the corresponding channel is absent. The incoming pulses are shown in grey and have been recorded over 2.5 instead of 25 million pulses. The insert shows a zoom on the retrieval window. There is no crosstalk in photon storage, i.e. no photons are retrieved in channel A if only medium B is present and vice versa. The channel separation is $d = 10\,\mu\text{m}$ and $n = 80$.

5.5 Observation of contactless effective photon interactions

In order to observe Rydberg mediated interactions between stored signal photons in spatially separated, non-overlapping channels, we investigate the photon counting statistics of the retrieved signal light (section 5.3). Simultaneously storing signal photons in both channels as collective Rydberg excitations with $|r\rangle = |80S_{1/2}\rangle$ and separation $d \approx 10\,\mu\text{m}$, we find $g^{(2)}_{AB} = 0.40 \pm 0.03$ (figure 5.7). The clear suppression below 1 is the result of a strong anti-correlation between photon detection events in both channels as VdW interactions imprint phase gradients in the collective excitations and modify the retrieval modes of the stored signal photons (section 5.2.2). In addition, we observe strong anti-bunching, $g^{(2)}_{A} = 0.17 \pm 0.03$ and $g^{(2)}_{B} = 0.20 \pm 0.04$, of the retrieved photons in the individual channels when the other is absent (section 4.3.1) as Rydberg blockade [20] and interaction-induced dephasing [45, 46, 49, 50, 89] limit photon storage and retrieval to almost a single photon per channel. In combination with the incoming photon numbers and overall storage-and-retrieval efficiencies of order $1 - 3\%$, this emphasises that interactions occur at the level of individual photons and are in principle suitable for applications in optical QIP. Below, we demonstrate the tunability of the interaction via both the choice of $|r\rangle$ and channel separation d.

5.5.1 Scaling with principal quantum number

To measure the effect of cross-channel interactions with interaction strength, the principal quantum number n of $|r\rangle = |nS_{1/2}\rangle$ is changed while keeping the channel separation $d \approx 10\,\mu\text{m}$ fixed. As previously discussed and demonstrated (section 4.3.1) for a single channel, VdW interactions exhibit a dramatic scaling $C_6 \propto n^{11}$ such that the choice of n presents a powerful handle to tune interactions [18, 19].

We follow the experimental procedure and storage-and-retrieval protocol

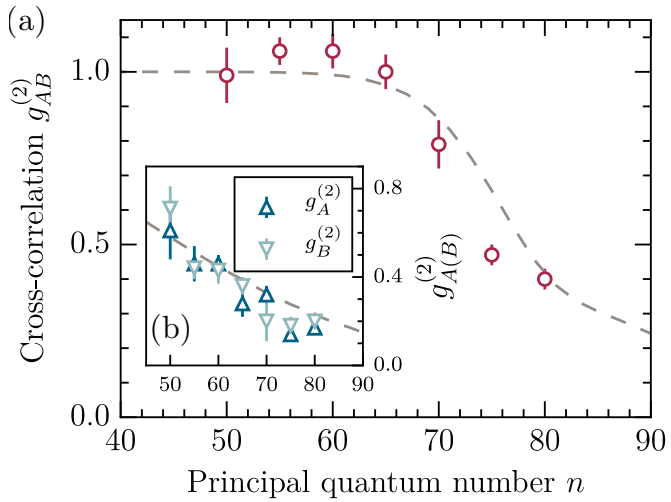

Figure 5.7: Effect of interaction strength on retrieved photon statistics. (a) Cross-channel correlation function $g^{(2)}_{AB}$ measured for photons retrieved following storage in Rydberg state $|r\rangle = |nS_{1/2}\rangle$ with principal quantum number n. The channel separation is 10 µm. Increasingly strong VdW interactions ($\propto n^{11}$) lead to a increasingly strong suppression $g^{(2)}_{AB} < 1$ for $n > 65$. (b) The inset shows the single-channel correlation functions $g^{(2)}_{A(B)}$ for comparison. In both panels, the dashed grey lines represent results of the phase-shift model.

sequence described above. The control Rabi frequency $\Omega_C/2\pi \approx 7 \pm 1\,\mathrm{MHz}$ is approximately constant for all values of n between 50 and 80 by adjusting the intensity accordingly.

The results are presented in figure 5.7 (a). Figure 5.7 (b) shows data for the single channel correlation functions $g^{(2)}_A$ and $g^{(2)}_B$ previously presented in figure 4.11 to allow comparison of inter- and intra-channel interaction strengths. For lower values of $n < 65$, $g^{(2)}_{AB} \approx 1$ indicates that photon retrieval in both channels is uncorrelated and inter-channel interactions are absent. For $n > 65$ an increasingly strong suppression $g^{(2)}_{AB} < 1$ can be observed. The experimental data and results of the model presented in section 5.6 below are in good agreement. This indicates that the cross-channel anti-correlations are the result of phase-shifts induced by VdW interactions between the stored photons that alter the retrieved mode of

the signal photons as outlined in section 5.2.2. As in section 4.3.1 in the previous chapter, the errors are obtained by splitting each dataset into multiple subsets and calculating the mean and statistical standard error over all subsets [250].

While the cross-channel correlation function gives $g^{(2)}_{AB} \approx 1$ for $n < 65$, the single-channel functions are already clearly suppressed for $n = 50$, $g^{(2)}_{A} = 0.6 \pm 0.1$ and $g^{(2)}_{B} = 0.7 \pm 0.1 < 1$. The suppression of the single channel correlation functions is consistently stronger than that of the inter-channel function indicating that intra-channel interactions are stronger than inter-channel. This behaviour can be explained by the emergence of two characteristic interaction length scales: Across channels, the inter-channel distance d represents a geometric constraint for the minimum spacing between excitations and thus the interaction strength (compare section 5.2.2) while the continuous storage medium within a channel imposes no lower bounds on the spacing between Rydberg excitations.

Even though there are no geometric constraints on excitation spacings within a channel, blockade prevents multiple excitations within a sphere defined by r_b [20, 21, 122]. In the most extreme case, the entire medium could be blockaded and saturate the storage. Since the radial extend of the medium is small compared to r_b, $1.5\,\mu\text{m} < 4\,\mu\text{m} \approx r_b^{(6)}(50S_{1/2})$, the excitations would form an ordered one-dimensional chain [48, 51] where the spacing of the emergent 'lattice' corresponds to r_b. In this case, r_b would impose a lower limit for the interaction distance. From $r_b^{(6)}(80S_{1/2}) \approx 9\,\mu\text{m}$ and a cloud length $> 40\,\mu\text{m}$ follows that at least three collective excitations are required for saturation at $n = 80$. Since the storage-and-retrieval efficiency is on the order of 1% and the mean signal photon number is 2.2 ± 0.2, single-channel blockade is not expected to play a major role.

Rydberg blockade also represents another potential cross-channel interaction mechanism as discussed in section 5.2.1. If $r_b > d$, a signal photon stored as a collective excitation in one channel will shift the control field off resonance in a fraction of the other's medium. Since the VdW blockade radius scales as $r_b^{(6)} \propto n^{11/6}$, blockade becomes increasingly important

as n increases (section 2.1.2). For the highest principal quantum number investigated here, $n = 80$, $r_b^{(6)}(80S_{1/2}) \approx 9\,\mu\text{m} < d$ such that only a minimal fraction of the medium may be blockaded.[6] The importance of interaction-induced phase-shifts in comparison to blockade becomes particularly evident as suppression of $g_{AB}^{(2)} < 1$ is already observed for $n = 65$ where $d \approx 10\,\mu\text{m} > r_b^{(6)}(65S_{1/2}) \approx 6\,\mu\text{m}$. This implies that interactions can induce significant phase-shifts outside the blockaded regime and need to be considered in potential applications involving side-by-side storage of photons as collective Rydberg excitations [65, 70, 71]. Observing a significant effect of blockade on the interaction between channels would require to increase $r_b > d$. However, we do not increase $n > 80$ since we observe a strong reduction in the number of retrieved photons for $n \geq 90$, most likely due to density-induced dephasing [55, 189].

5.5.2 Scaling with channel separation

Besides the state dependent interaction strength described by the VdW-coefficient C_6, the dependence of the VdW potential $V_{VdW}(r_{jk}) = C_6/r_{jk}^6$ on the distance r_{jk} between two interacting Rydberg atoms [18, 19] provides another handle to tune interactions. Changes of the channel separation d alter the distribution of spacings between excitation pairs, i.e. $r_{jk} \gtrsim d$. In the following, the dependence of the cross-channel correlation function $g_{AB}^{(2)}$ on d is investigated. Unlike the choice of Rydberg state, this distance dependence of the VdW-interaction remained inaccessible in previous experiments where signal photons were propagating in either the same or overlapping optical modes.

To study the distance dependence, $|r\rangle = |80S_{1/2}\rangle$ remains fixed at a relatively high principal quantum number $n = 80$. This permits to observe

[6] Note that measurements of $g_{AB}^{(2)}$ vs. n or d are in principle insufficient on their own to distinguish the effects of interaction-induced phase-shifts and blockade. The conclusion that phase-shifts are dominant is thus based on $d > r_b^{(6)}$ and comparison to simulations. However, more recent measurements by S. W. Ball show a dependence of $g_{AB}^{(2)}$ on t_{st} giving a clear indication of phase shifts increasing with time [85].

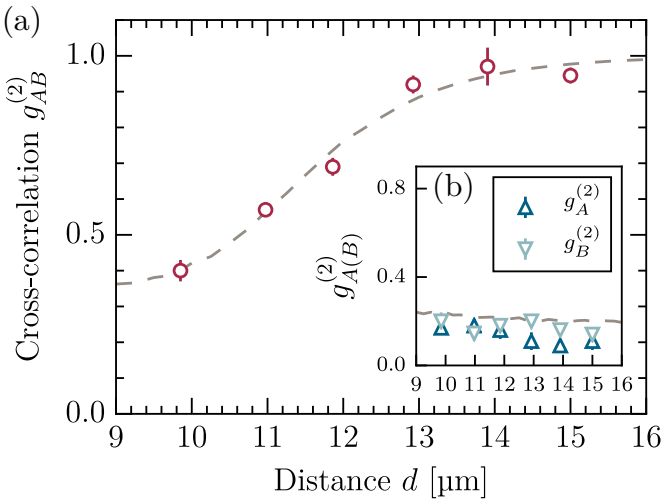

Figure 5.8: Effect of channel separation d on retrieved photon statistics. (a) Cross-channel correlation function $g^{(2)}_{AB}$ at different separations d with $|r\rangle = |80S_{1/2}\rangle$. Suppression below 1 occurs well above the range of the excitation blockade, $r_b^{(6)}(80S_{1/2}) \approx 9\,\mu\text{m}$. (b) The inset shows the single-channel correlation functions $g^{(2)}_{A(B)}$ in absence of the second channel which remains approximately constant as expected showing that inter-channel interactions are independently tunable by varying d. In both panels, the dashed grey lines represent results of the phase-shift model.

the resulting change in interaction strength and interaction-induced phase shifts over a sufficiently large range, without cross-talk in signal photon transmission and storage (section 5.4). The experimental procedure remains the same. Each time d is changed, the control field is realigned and its intensity readjusted to ensure an approximately constant control Rabi frequency $\Omega_C/2\pi = 9 \pm 1\,\text{MHz}$ for both channels, except for $d = 10\,\mu\text{m}$ where $\Omega_C/2\pi = 7 \pm 1\,\text{MHz}$.

The results are shown in figure 5.8 (a). An increasingly strong suppression $g^{(2)}_{AB} < 1$ is observed for separations $d < 13\,\mu\text{m}$. This corresponds to increasingly strong interactions which lead to larger phase-shifts and thus stronger suppression of photon retrieval in the unperturbed signal modes as expected due to the $1/r_{jk}^6$-dependence of $V_{VdW}(r_{jk})$. Besides experimental results, simulation results for $g^{(2)}_{AB}$ are shown (section 5.6 below), again in

good agreement with each other. The inset, figure 5.8 (b), presents $g_A^{(2)}$ and $g_B^{(2)}$ measured in absence of the other channel which are approximately constant as expected. Slight fluctuations result most likely from minor changes in the relative alignment of the signal foci and atom cloud centres.[7]

The observed change in the cross-correlation function $g_{AB}^{(2)}$ while the single-channel functions $g_A^{(2)}$ and $g_B^{(2)}$ remain constant, shows that by changing d, the inter-channel interaction strength can be adjusted without affecting interactions within individual channels. The ability to control the long-range non-linear optical response independently [65, 70] is comparable to a decoupling of self- and cross-Kerr non-linearities which is impossible in a conventional, local non-linear optical medium [5]. It thus represents a genuinely new degree of freedom to engineer effective photon-photon interactions.

The current implementation employs the same Rydberg state for photon storage in both channels such that the degree to which inter- and intra-channel interactions can be decoupled, is limited. I.e. intra-channel interactions will always be at least as strong as inter-channel interactions. Initially storing the photons in different, weakly interacting states and exploiting a (Stark-tuned) Förster resonance [58, 127, 128, 130, 131] or microwave-coupling of $|r\rangle$ to an adjacent state $|p\rangle = |n'P_J\rangle$ with opposite parity [46, 47], would allow to decouple storage and interaction. This approach is central to the scheme that our group pursues to implement a optical CZ-gate [70]. Alternatively, photons could be stored in a non-interacting atomic ground state and subsequently coupled to a Rydberg state which also reduces the influence of motional dephasing [71, 181] (section 2.3.4).

Finally, we note that the observed interactions occur over distances corresponding to $10\lambda_S - 20\lambda_S$, well above the signal wavelength λ_S and thus the fundamental diffraction limited spot size. The observed interaction length scales are convenient for incorporation into multichannel nano-

[7] These fluctuations cannot be fully compensated since the dipole traps cannot be aligned independently in the current setup (figure 3.14).

photonic waveguides interfaced with cold atoms [74] or fibre-based photon memories [256, 257].

5.6 Two-channel phase-shift model

To model the effect of interaction-induced phase shifts on $g^{(2)}_{AB}$ in the experiments presented above, we extend the single-channel model described in section 4.3.2 [50]. The underlying principle does not change: While signal photons are stored as collective Rydberg excitations, they interact and each individual atom pair acquires a distance dependent interaction phase. To calculate the phase-shifts, experimentally realistic parameters, i.e. Gaussian signal modes and atom density distributions, are taken into account. The probability to simultaneously retrieve one photon in each channel is determined from the overlap between the initial two-channel collective ground state with the ground state following photon storage and retrieval in which a phase gradient has been imprinted by the interaction. Based on the probability, $g^{(2)}_{AB}$ can be calculated. As in the previous chapter, the simulations have been implemented jointly with P. Huillery and T. Ilieva.

Photon retrieval and statistics

As in the single channel case (section 4.3.2), the storage process is reversed to obtain the collective ground state of both channels after retrieval of ν and μ photons by acting on the time-evolved two-channel collective state $|R^{(\nu,\mu)}(t_{st})\rangle_{AB}$ (equation 5.4) with the annihilation operators S_A and S_B,

$$|G'(t_{st})\rangle_{AB} = (S_A)^{\nu}(S_B)^{\mu}\,|R^{(\nu,\mu)}(t_{st})\rangle_{AB}\,. \tag{5.7}$$

The reduced retrieval probability in the unperturbed signal modes is quantified by the overlap between the initial ground state $|G\rangle_{AB} = |G\rangle_A \otimes$

$|G\rangle_B$ and $|G'(t_{st})\rangle_{AB}$,

$$D_{AB}^{(\nu,\mu)} = \frac{\langle G|_{AB}|G'(t_{st})\rangle_{AB}}{\langle G|_{AB}(S_A)^\nu(S_B)^\mu(S_A^\dagger)^\nu(S_B^\dagger)^\mu|G\rangle_{AB}} = \frac{\langle G|_{AB}(S_A)^\nu(S_B)^\mu U_{AB}(t_{st})(S_A^\dagger)^\nu(S_B^\dagger)^\mu|G\rangle_{AB}}{\langle G|_{AB}(S_A)^\nu(S_B)^\mu(S_A^\dagger)^\nu(S_B^\dagger)^\mu|G\rangle_{AB}}. \tag{5.8}$$

To obtain values for the inter-channel correlation function $g_{AB}^{(2)}$, the number distribution of initially stored signal photons has to be accounted for because the overlap $D_{AB}^{(\nu,\mu)}$ is calculated for specific photon numbers, not number distributions. Following storage, the ensembles are thus considered in a superposition

$$|R\rangle_{AB} = \sum_{\nu,\mu} c_{\nu,\mu}\,|R^{(\nu,\mu)}\rangle_{AB} \tag{5.9}$$

where the coefficients $c_{\nu,\mu}$ are related to the probability $|c_{\nu,\mu}|^2$ that ν photons are stored in channel A and μ in channel B.[8] The use of a coherent superposition state instead of a density matrix [50, 251] neglects decoherence occurring during the initial storage process and while the photons are stored. This simplification is reasonable as motivated in section 4.3.2 due to the low photon and excitation numbers that are considered here ($\langle\nu\rangle, \langle\mu\rangle \ll 1$).

In the experiments, the mean photon numbers for the incoming signal pulses are of order ≈ 2 and storage-and-retrieval efficiencies of order 0.01. Therefore, it is reasonable to consider no more than a single collective excitation per channel and thus

$$|R\rangle_{AB} = \sum_{\nu,\mu\in\{0,1\}} c_{\nu,\mu}\,|R^{(\nu,\mu)}\rangle_{AB}. \tag{5.10}$$

[8] The coefficients themselves cannot be obtained from the probability distribution as they may also include a complex phase. This is not relevant, however, as only the probability $|c_{\nu,\mu}|^2$ is needed to compute $g_{AB}^{(2)}$.

Consequently, $D_{AB}^{(\nu,\mu)}$ simplifies to

$$D_{AB}^{(1,1)} = \frac{\sum_{j,k} \left(\epsilon_A(\vec{r}_j)\epsilon_B(\vec{r}_k)\right)^2 e^{-iV_{jk}t_{st}/\hbar}}{\sum_{j,k} \left(\epsilon_A(\vec{r}_j)\epsilon_B(\vec{r}_k)\right)^2} \tag{5.11}$$

omitting all terms which correspond to intra-channel interactions. Based on the initial photon number distributions and the probability $|D_{AB}^{(1,1)}|^2$ to retrieve two photons in their original modes, the value for the inter-channel correlation function is given by

$$g_{AB}^{(2)} = \frac{|D_{AB}^{(1,1)}|^2 |c_{1,1}|^2}{\left(|c_{0,1}|^2 + |D_{(AB)}^{(1,1)}|^2 |c_{1,1}|^2\right)\left(|c_{1,0}|^2 + |D_{(AB)}^{(1,1)}|^2 |c_{1,1}|^2\right)}. \tag{5.12}$$

Simulation parameters and results

The simulation procedure itself again follows the steps previously laid out for a single channel in section 4.3.2. The same parameters are used for the ensembles (atom number $\mathcal{N}_A = \mathcal{N}_B = 1000$, Gaussian atom distribution with standard deviations 21 µm along and 1.5 µm perpendicular to the beam axes), signal beam waists ($1/e^2$-radii 1 µm), and mean photon numbers ($\langle\nu\rangle = \langle\mu\rangle = 0.01$). Furthermore, we find again that the values for $\langle\nu\rangle, \langle\mu\rangle, \mathcal{N}_A$, and $\mathcal{N}_B$ do not affect the results as long as $\langle\nu\rangle, \langle\mu\rangle \ll 1 \ll \mathcal{N}_A, \mathcal{N}_B$.

Figure 5.9 shows simulation results for $g_{AB}^{(2)}$ as the principal quantum number n of $|r\rangle = |nS_{1/2}\rangle$ is varied between 50 and 110. As expected, the anti-correlation in the photon retrieval increases with n since the interaction strength of the VdW-potential scales as $V_{VdW} \propto n^{11}$ and increasingly strong phase shifts lead to stronger depletion of the original signal modes. Panel (a) shows the results for different channel separations and $t_{st} = 170\,\text{ns}$, panel (b) for different storage and hence interaction times t_{st} between 100 and 970 ns. Since the phase shifts induced between individual atoms accumulate linearly with t_{st}, longer interaction times result in a stronger suppression of simultaneous photon retrieval. As already shown in figure 5.7, the simulation results are in good agreement with the experimental

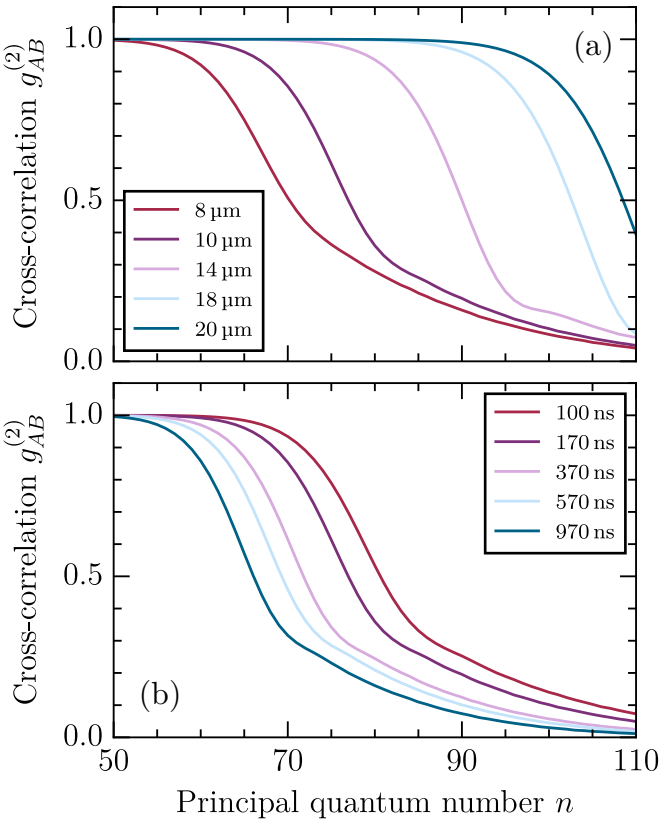

Figure 5.9: Simulation results for cross-correlation function for different principal quantum numbers. (a) Values of $g^{(2)}_{AB}$ for different channel separations d and $t_{st} = 170\,\text{ns}$. (b) Values of $g^{(2)}_{AB}$ for different interaction times t_{st} and $d = 10\,\mu\text{m}$.

data.

In figure 5.10, interaction-induced anti-correlations of the retrieved photons are investigated as a function of the inter-channel distance d. Simulation results are shown for storage in five different Rydberg states $|r\rangle = |nS_{1/2}\rangle$ and $t_{st} = 170\,\text{ns}$. Initially, the anti-correlations increase as the channels are brought closer together and stronger interactions lead to stronger phase shifts. Noticeably, $g^{(2)}_{AB}$ approaches values which approximately correspond to the value of the single channel correlation function $g^2_{A(B)}$ (compare section 4.3). This not surprising, as $g^2_{A(B)}$ becomes

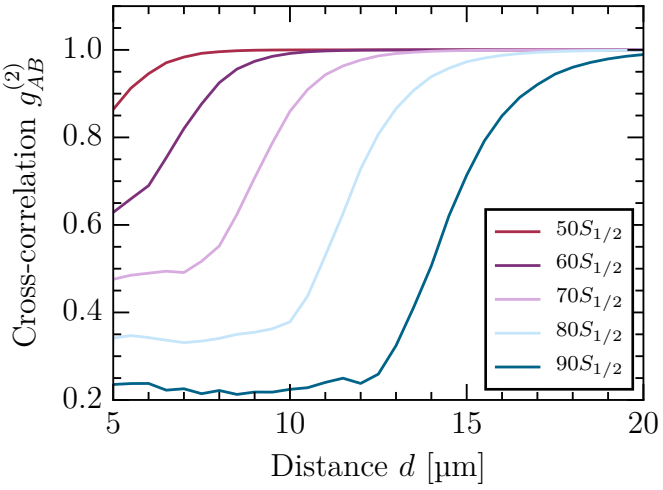

Figure 5.10: Simulation results for cross-correlation function for different inter-channel separations d. Results are shown for different Rydberg states $|nS_{1/2}\rangle$ with principal quantum numbers $n = 50$ to 90.

equivalent to $g^{(2)}_{AB}$ in the limit $d = 0\,\mu\text{m}$. The distances d below which $g^{(2)}_{AB}$ remains constant are similar to typical blockade radii for the corresponding states. Again, the simulation results are in good agreement with the experimental data in figure 5.8.

6 Conclusion and outlook

In summary, this thesis reports on the implementation of an experimental setup dedicated to quantum non-linear optics with cold Rydberg atoms, and on the experimental demonstration of contactless and long-range effective interactions between non-overlapping photons stored as collective Rydberg excitations.

The new experimental setup [88] presented in chapter 3 provides near diffraction limited optical resolution of 1 µm thanks to in-vacuo aspheric lenses [93] which enable the implementation of side-by-side channels consisting of tightly focussed optical modes for signal and microscopic, optically trapped [92] cold Rb ensembles. These channels are individually addressable at distances well below range of dipolar interactions between Rydberg atoms. Effective cycle rates exceeding 100 kHz are the result of fast and efficient MOT loading using an atom beam generated by a 2D MOT [94] as well as the ability to recycle the ensembles several 10 000 times without substantial atom loss. In addition, a set of eight electrodes to actively compensate stray electric fields and tune Rydberg interactions, as well as three microwave antennae to drive transitions between Rydberg states with frequencies of up to 40 GHz are also placed in-vacuo.

In chapter 4, a selection of experiments [88] has demonstrated that the setup is well suited for Rydberg quantum optics. These include the demonstration of an intensity-dependent transmission in Rydberg EIT [26, 40], the saturation of photon storage in a microscopic atomic medium [45] due to interaction-induced dephasing [49, 50] and blockade [20, 21, 122], and the generation of highly non-classical states of light [45, 46]. All these demonstrations of quantum non-linear optics benefit from the fast

cycle times of the new experimental setup, i.e. the analysis of second-order correlations in the retrieved photon statistics which can be measured in 10 minutes or less with relative errors below 10%.

Finally, chapter 5 presents the most important result of this thesis, the demonstration of a contactless interaction between photons stored as collective Rydberg excitations [85]. The interactions manifest themselves in a spatial anti-correlation of the retrieved photons. The anti-correlations emerge as VdW interactions between the collective excitations are imprinting spatially non-uniform phase shifts [50] in the collective spin-waves distorting the retrieval modes, i.e. suppressing photon retrieval in the original signal modes. The interaction has been investigated for different Rydberg states and thus interaction strengths, as well as distances between channels and the results are in good agreement with a phase-shift model building upon earlier work by Bariani *et al.* [50] on interaction-induced dephasing in a single optical mode.

Evolution of the experimental setup

Following the proof-of-principle demonstration of contactless effective photon interactions, several improvements are planned for the experimental setup to study them further and harness them for applications, e.g. in optical QIP and quantum simulation.

It is desirable to increase the atom number in the microscopic traps to achieve higher optical depth and to improve longitudinal confinement of the microscopic atom clouds. Therefore, a crossed optical dipole trap [92, 244] is currently being implemented which will intersect with the microscopic traps at 90° and serve as a reservoir to improve loading of the microscopic traps [61]. Stronger confinement should allow to explore regimes where each ensemble, or even both, can be fully blockaded by a single stored photon [61], in analogy to previous work with individual atoms [24, 25] and ensemble qubits [87].

To individually store, retrieve, and address photons, it can be useful to employ different Rydberg states and/or individual control fields for the

individual channels. Using different states requires an additional laser with a wavelength of 480 nm due to the GHz spacings between Rydberg states. A frequency doubled titanium sapphire laser[1] has recently been installed and is in the process of being set up and frequency stabilised for this purpose.

The storage-and-retrieval efficiency and lifetime are currently limited due to limited compression of the signal pulse inside the storage medium [176], not fully adiabatic state transfer [38, 170], and motional dephasing [177]. To reduce the group velocity and improve the signal compression, one could either decrease Ω_C or increase the optical depth by increasing the atom number density. The viability of the former approach is limited by the spectral width of the signal light which is ideally contained within Δ_{EIT}, the latter by density induced dephasing [55, 189] (section 2.3.4). The signal linewidth could be reduced by stabilising the laser to a high-finesse cavity. The optical depth could be increased without increasing the atom density by either increasing the size of the signal modes or choosing longer storage media. Tiarks *et al.* [59] have achieved $\approx 20\%$ storage-and retrieval efficiency using blue detuned light sheets [258] to control the length of the medium. The adiabacity of the transfer could be improved by controlling the shape of the signal and control pulses. This could be realised with minor modifications to the respective laser systems. Motional dephasing (section 2.3.4) could be suppressed by reducing the temperature of the atoms, for example by implementing Raman sideband cooling [249] or alternative evaporation schemes in conjunction with the new dipole trap mentioned above. Another alternative is a four-level EIT scheme where the angles between beams can be chosen such that the wavevectors of the EIT fields sum to zero resulting in large spin-wave wavelengths [259], but this would be difficult to implement in the current setup. This also applies to two-dimensional atomic monolayers [260] in which high signal extinction may be reached in a short medium and at well-controlled inter-atomic spacings at which density induced dephasing can be avoided.

[1] MSquared SolsTis 2000 ECD-X.

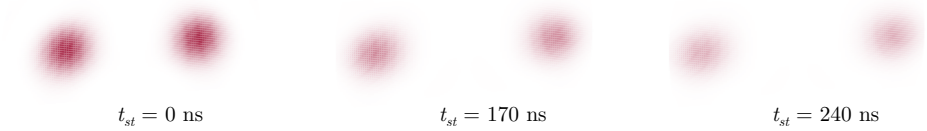

Figure 6.1: Effect of contactless, Rydberg mediated interactions on photon retrieval modes. For strongly localised, spherical ensembles (atom numbers $\mathcal{N}_{A(B)} = 1000$, standard deviation of Gaussian atom distributions $\sigma_r = \sigma_z = 1.5\,\mu\text{m}$, $d = 10\,\mu\text{m}$, $|r\rangle = |80S_{1/2}\rangle$) the imprinted phase-gradients are relatively uniform. Preliminary calculations of the intensity distribution of the retrieval show a 'deflection' rather than just a depletion of the output modes. The deflection increases with time as stronger phase-shits are accumulated. All intensity distributions are normalised to the maximum at $t_{st} = 0\,\text{ns}$.

Outlook

In this thesis, the demonstration of contactless non-linear optics was limited to a proof-of-principle, but a variety of intriguing follow-up experiments come to mind. A logical next step is to investigate if correlations can be observed between retrieved signal photons outside their original modes as suggested by the simulated retrieval patterns in figure 6.1, instead of anti-correlations between their original modes.

An obvious technical application are photonic quantum gates [70, 71]. An important prerequisite of a proposal originating from our group [70] are high-fidelty microwave rotations of stored optical qubits. Figure 6.2 shows preliminary results for microwave Rabi oscillations of a signal photon stored as collective Rydberg excitation [46]. Here, a coherent signal pulse with a mean well below 1 was used to avoid creation of two Rydberg excitations and interactions. Following storage in $|r\rangle = |60S_{1/2}\rangle$, oscillations are driven between $|r\rangle$ and $|r'\rangle = |59P_{1/2}\rangle$. Since the photon is only retrieved if the collective excitation is in $|r\rangle$, the oscillation can be observed in the retrieval as the microwave pulse duration is varied. The absence of strong decay represents a promising starting point for future work on qubit rotations and phase-shifts that can be conditionally suppressed upon the presence

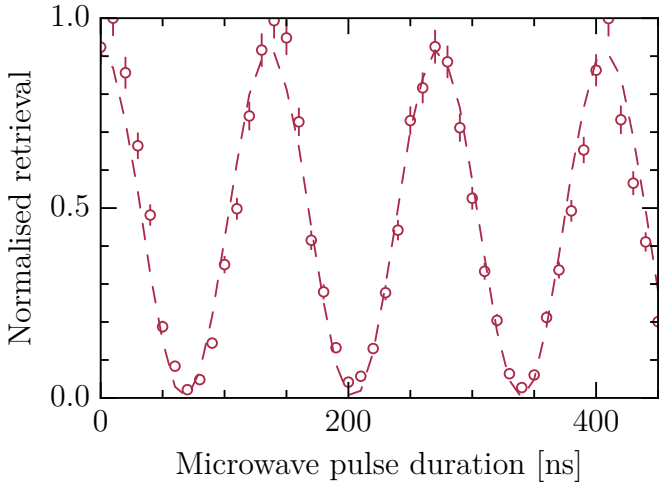

Figure 6.2: Microwave Rabi oscillation of a stored photon. Following storage in $|r\rangle = |60S_{1/2}\rangle$, a microwave field with constant intensity drives oscillations between $|r\rangle$ and $|r'\rangle = |59P_{1/2}\rangle$. As the microwave pulse duration is varied, an oscillation in the retrieved photon number can be observed. The storage time t_{st} remains constant to ensure effects of motional dephasing are the similar regardless of the pulse duration. Courtesy of S. W. Ball.

of a control qubit stored in an adjacent channel [70].

More generally, Rydberg mediated interactions between spatially separated photons open the door to study strongly correlated many-body dynamics with photons stored as collective Rydberg excitations instead of individual Rydberg atoms in ordered arrays or optical lattices. Potential benefits include coherent readout of the collective excitations and the ability to measure phase in addition to amplitude. Potential areas of study include the emergence of spatial correlations in interacting many-body systems [98, 114, 149], non-radiative energy transfer processes [64, 133, 137], and simulation of Ising Hamiltonians [51, 98, 113, 138]. If required, larger arrays of signal photon modes and microscopic dipole traps could be realised with SLMs [96] or acousto-optical deflectors (AODs) [255].

Bibliography

[1] W. Heisenberg and H. Euler, "Folgerungen aus der Diracschen Theorie des Positrons", Z. Phys. **98**, 714–732 (1936).

[2] V. F. Weisskopf, "Über die Elektrodynamik des Vakuums auf Grund der Quantentheorie des Elektrons", Kong. Dans. Vid. Selsk. Math.-fys. Medd. **14**, 3–39 (1936).

[3] K. C. Kao and G. A. Hockham, "Dielectric-fibre surface waveguides for optical frequencies", Proc. IEE **113**, 1151–1158 (1966).

[4] J. L. O'Brien, "Optical Quantum Computing", Science **318**, 1567–1570 (2007).

[5] R. W. Boyd, *Nonlinear Optics*, 3rd ed. (Academic Press, San Diego, 2008).

[6] A. L. Schawlow and C. H. Townes, "Infrared and Optical Masers", Phys. Rev. **112**, 1940–1949 (1958).

[7] T. H. Maiman, "Stimulated Optical Radiation in Ruby", Nature **187**, 493–494 (1960).

[8] D. E. Chang, V. Vuletić, and M. D. Lukin, "Quantum nonlinear optics—photon by photon", Nat. Photon. **8**, 685–694 (2014).

[9] J. M. Raimond, M. Brune, and S. Haroche, "Manipulating quantum entanglement with atoms and photons in a cavity", Rev. Mod. Phys. **73**, 565–582 (2001).

[10] S. Haroche, "Nobel Lecture: Controlling photons in a box and exploring the quantum to classical boundary", Rev. Mod. Phys. **85**, 1083–1102 (2013).

[11] H. J. Kimble, "Strong interactions of single atoms and photons in cavity QED", Phys. Scripta **1998**, 127–137 (1998).

[12] A. Reiserer and G. Rempe, "Cavity-based quantum networks with single atoms and optical photons", Rev. Mod. Phys. **87**, 1379–1418 (2015).

[13] J. McKeever, A. Boca, A. D. Boozer, R. Miller, J. R. Buck, A. Kuzmich, and H. J. Kimble, "Deterministic Generation of Single Photons from One Atom Trapped in a Cavity", Science **303**, 1992–1994 (2004).

[14] K. M. Birnbaum, A. Boca, R. Miller, A. D. Boozer, T. E. Northup, and H. J. Kimble, "Photon blockade in an optical cavity with one trapped atom", Nature **436**, 87–90 (2005).

[15] W. Chen, K. M. Beck, R. Bücker, M. Gullans, M. D. Lukin, H. Tanji-Suzuki, and V. Vuletić, "All-Optical Switch and Transistor Gated by One Stored Photon", Science **341**, 768–770 (2013).

[16] K. M. Beck, M. Hosseini, Y. Duan, and V. Vuletić, "Large conditional single-photon cross-phase modulation", Proc. Natl. Acad. Sci. **113**, 9740–9744 (2016).

[17] B. Hacker, S. Welte, G. Rempe, and S. Ritter, "A photon–photon quantum gate based on a single atom in an optical resonator", Nature **536**, 193–196 (2016).

[18] T. F. Gallagher, *Rydberg Atoms*, 1st ed. (Cambridge University Press, Cambridge, 1994).

[19] M. Saffman, T. G. Walker, and K. Mølmer, "Quantum information with Rydberg atoms", Rev. Mod. Phys. **82**, 2313–2363 (2010).

[20] M. D. Lukin, M. Fleischhauer, R. Côté, L. M. Duan, D. Jaksch, J. I. Cirac, and P. Zoller, "Dipole Blockade and Quantum Information Processing in Mesoscopic Atomic Ensembles", Phys. Rev. Lett. **87**, 037901 (2001).

[21] D. Comparat and P. Pillet, "Dipole blockade in a cold Rydberg atomic sample", J. Opt. Soc. Am. B **27**, A208–A232 (2010).

[22] K. Singer, M. Reetz-Lamour, T. Amthor, L. G. Marcassa, and M. Weidemüller, "Suppression of Excitation and Spectral Broadening Induced by Interactions in a Cold Gas of Rydberg Atoms", Phys. Rev. Lett. **93**, 163001 (2004).

[23] D. Tong, S. M. Farooqi, J. Stanojevic, S. Krishnan, Y. P. Zhang, R. Côté, E. E. Eyler, and P. L. Gould, "Local Blockade of Rydberg Excitation in an Ultracold Gas", Phys. Rev. Lett. **93**, 063001 (2004).

[24] A. Gaëtan, Y. Miroshnychenko, T. Wilk, A. Chotia, M. Viteau, D. Comparat, P. Pillet, A. Browaeys, and P. Grangier, "Observation of collective excitation of two individual atoms in the Rydberg blockade regime", Nat. Phys. **5**, 115–118 (2009).

[25] E. Urban, T. A. Johnson, T. Henage, L. Isenhower, D. D. Yavuz, T. G. Walker, and M. Saffman, "Observation of Rydberg blockade between two atoms", Nat. Phys. **5**, 110–114 (2009).

[26] J. D. Pritchard, D. Maxwell, A. Gauguet, K. J. Weatherill, M. P. A. Jones, and C. S. Adams, "Cooperative Atom-Light Interaction in a Blockaded Rydberg Ensemble", Phys. Rev. Lett. **105**, 193603 (2010).

[27] J. D. Pritchard, K. J. Weatherill, and C. S. Adams, "Nonlinear optics using cold Rydberg atoms", in *Annual Review of Cold Atoms and Molecules, Volume 1*, edited by K. Madison, Y. Wang, A. M. Rey, and K. Bongs (World Scientific, 2013), pp. 301–350.

[28] O. Firstenberg, C. S. Adams, and S. Hofferberth, "Nonlinear quantum optics mediated by Rydberg interactions", J. Phys. B: At. Mol. Opt. Phys. **49**, 152003 (2016).

[29] C. Murray and T. Pohl, "Quantum and Nonlinear Optics in Strongly Interacting Atomic Ensembles", in *Advances in Atomic, Molecular, and Optical Physics, Volume 65*, edited by E. Arimondo, C. C. Lin, and S. F. Yelin (Academic Press, 2016), pp. 321–372.

[30] S. E. Harris, J. E. Field, and A. Imamoğlu, "Nonlinear optical processes using electromagnetically induced transparency", Phys. Rev. Lett. **64**, 1107–1110 (1990).

[31] K.-J. Boller, A. Imamoğlu, and S. E. Harris, "Observation of electromagnetically induced transparency", Phys. Rev. Lett. **66**, 2593–2596 (1991).

[32] M. Fleischhauer, A. Imamoglu, and J. P. Marangos, "Electromagnetically induced transparency: Optics in coherent media", Rev. Mod. Phys. **77**, 633–673 (2005).

[33] A. K. Mohapatra, T. R. Jackson, and C. S. Adams, "Coherent Optical Detection of Highly Excited Rydberg States Using Electromagnetically Induced Transparency", Phys. Rev. Lett. **98**, 113003 (2007).

[34] L. V. Hau, S. E. Harris, Z. Dutton, and C. H. Behroozi, "Light speed reduction to 17 metres per second in an ultracold atomic gas", Nature **397**, 594–598 (1999).

[35] A. Feizpour, M. Hallaji, G. Dmochowski, and A. M. Steinberg, "Observation of the nonlinear phase shift due to single post-selected photons", Nat. Photon **11**, 905–909 (2015).

[36] Z.-Y. Liu, Y.-H. Chen, Y.-C. Chen, H.-Y. Lo, P.-J. Tsai, I. A. Yu, Y.-C. Chen, and Y.-F. Chen, "Large Cross-Phase Modulations at the Few-Photon Level", Phys. Rev. Lett. **117**, 203601 (2016).

[37] M. Bajcsy, S. Hofferberth, V. Balic, T. Peyronel, M. Hafezi, A. S. Zibrov, V. Vuletic, and M. D. Lukin, "Efficient All-Optical Switching Using Slow Light within a Hollow Fiber", Phys. Rev. Lett. **102**, 203902 (2009).

[38] M. Fleischhauer and M. D. Lukin, "Dark-State Polaritons in Electromagnetically Induced Transparency", Phys. Rev. Lett. **84**, 5094–5097 (2000).

[39] C. Liu, Z. Dutton, C. H. Behroozi, and L. V. Hau, "Observation of coherent optical information storage in an atomic medium using halted light pulses", Nature **409**, 490–493 (2001).

[40] T. Peyronel, O. Firstenberg, Q.-Y. Liang, S. Hofferberth, A. V. Gorshkov, T. Pohl, M. D. Lukin, and V. Vuletić, "Quantum nonlinear optics with single photons enabled by strongly interacting atoms", Nature **448**, 57–60 (2012).

[41] C. S. Hofmann, G. Günter, H. Schempp, M. Robert-de-Saint-Vincent, M. Gärttner, J. Evers, S. Whitlock, and M. Weidemüller, "Sub-Poissonian Statistics of Rydberg-Interacting Dark-State Polaritons", Phys. Rev. Lett. **110**, 203601 (2013).

[42] S. Sevinçli, N. Henkel, C. Ates, and T. Pohl, "Nonlocal Nonlinear Optics in Cold Rydberg Gases", Phys. Rev. Lett. **107**, 153001 (2011).

[43] A. V. Gorshkov, J. Otterbach, M. Fleischhauer, T. Pohl, and M. D. Lukin, "Photon-Photon Interactions via Rydberg Blockade", Phys. Rev. Lett. **107**, 133602 (2011).

[44] D. Petrosyan, J. Otterbach, and M. Fleischhauer, "Electromagnetically Induced Transparency with Rydberg Atoms", Phys. Rev. Lett. **107**, 213601 (2011).

[45] Y. O. Dudin and A. Kuzmich, "Strongly Interacting Rydberg Excitations of a Cold Atomic Gas", Science **336**, 887–889 (2012).

[46] D. Maxwell, D. J. Szwer, D. Paredes-Barato, H. Busche, J. D. Pritchard, A. Gauguet, K. J. Weatherill, M. P. A. Jones, and C. S. Adams, "Storage and Control of Optical Photons Using Rydberg Polaritons", Phys. Rev. Lett. **110**, 103001 (2013).

[47] D. Maxwell, D. J. Szwer, D. Paredes-Barato, H. Busche, J. D. Pritchard, A. Gauguet, M. P. A. Jones, and C. S. Adams, "Microwave control of the interaction between two optical photons", Phys. Rev. A **89**, 043827 (2014).

[48] Y. O. Dudin, F. Bariani, and A. Kuzmich, "Emergence of Spatial Spin-Wave Correlations in a Cold Atomic Gas", Phys. Rev. Lett. **109**, 133602 (2012).

[49] F. Bariani, Y. O. Dudin, T. A. B. Kennedy, and A. Kuzmich, "Dephasing of Multiparticle Rydberg Excitations for Fast Entanglement Generation", Phys. Rev. Lett. **108**, 030501 (2012).

[50] F. Bariani, P. M. Goldbart, and T. A. B. Kennedy, "Dephasing dynamics of Rydberg atom spin waves", Phys. Rev. A **86**, 041802 (2012).

[51] S. Bettelli, D. Maxwell, T. Fernholz, C. S. Adams, I. Lesanovsky, and C. Ates, "Exciton dynamics in emergent Rydberg lattices", Phys. Rev. A **88**, 043436 (2013).

[52] R. Heidemann, U. Raitzsch, V. Bendkowsky, B. Butscher, R. Löw, L. Santos, and T. Pfau, "Evidence for Coherent Collective Rydberg Excitation in the Strong Blockade Regime", Phys. Rev. Lett. **99**, 163601 (2007).

[53] V. Parigi, E. Bimbard, J. Stanojevic, A. J. Hilliard, F. Nogrette, R. Tualle-Brouri, A. Ourjoumtsev, and P. Grangier, "Observation and Measurement of Interaction-Induced Dispersive Optical Nonlinearities in an Ensemble of Cold Rydberg Atoms", Phys. Rev. Lett. **109**, 233602 (2012).

[54] O. Firstenberg, T. Peyronel, Q.-Y. Liang, A. V. Gorshkov, M. D. Lukin, and V. Vuletić, "Attractive photons in a quantum nonlinear medium", Nature **502**, 71–75 (2013).

[55] S. Baur, D. Tiarks, G. Rempe, and S. Dürr, "Single-Photon Switch Based on Rydberg Blockade", Phys. Rev. Lett. **112**, 073901 (2014).

[56] H. Gorniaczyk, C. Tresp, J. Schmidt, H. Fedder, and S. Hofferberth, "Single-Photon Transistor Mediated by Interstate Rydberg Interactions", Phys. Rev. Lett. **113**, 053601 (2014).

[57] D. Tiarks, S. Baur, K. Schneider, S. Dürr, and G. Rempe, "Single-Photon Transistor Using a Förster Resonance", Phys. Rev. Lett. **113**, 053602 (2014).

[58] H. Gorniaczyk, C. Tresp, P. Bienias, A. Paris-Mandoki, W. Li, I. Mirgorodskiy, H. P. Büchler, I. Lesanovsky, and S. Hofferberth, "Enhancement of Rydberg-mediated single-photon nonlinearities by electrically tuned Förster resonances", Nat. Commun. **7**, 12480 (2016).

[59] D. Tiarks, S. Schmidt, G. Rempe, and S. Dürr, "Optical π phase shift created with a single-photon pulse", Sci. Adv. **2**, 1600036 (2016).

[60] L. Li, Y. O. Dudin, and A. Kuzmich, "Entanglement between light and an optical atomic excitation", Nature **498**, 466–469 (2013).

[61] C. Tresp, C. Zimmer, I. Mirgorodskiy, H. Gorniaczyk, A. Paris-Mandoki, and S. Hofferberth, "Single-Photon Absorber Based on Strongly Interacting Rydberg Atoms", Phys. Rev. Lett. **117**, 223001 (2016).

[62] B. Olmos, W. Li, S. Hofferberth, and I. Lesanovsky, "Amplifying single impurities immersed in a gas of ultracold atoms", Phys. Rev. A **84**, 041607 (2011).

[63] G. Günter, M. Robert-de-Saint-Vincent, H. Schempp, C. S. Hofmann, S. Whitlock, and M. Weidemüller, "Interaction Enhanced Imaging of Individual Rydberg Atoms in Dense Gases", Phys. Rev. Lett. **108**, 013002 (2012).

[64] G. Günter, H. Schempp, M. Robert-de-Saint-Vincent, V. Gavryusev, S. Helmrich, C. S. Hofmann, S. Whitlock, and M. Weidemüller, "Observing the Dynamics of Dipole-Mediated Energy Transport by Interaction-Enhanced Imaging", Science **342**, 954–956 (2013).

[65] B. He, A. V. Sharypov, J. Sheng, C. Simon, and M. Xiao, "Two-Photon Dynamics in Coherent Rydberg Atomic Ensemble", Phys. Rev. Lett. **112**, 133606 (2014).

[66] J. H. Shapiro, "Single-photon Kerr nonlinearities do not help quantum computation", Phys. Rev. A **73**, 062305 (2006).

[67] J. Gea-Banacloche, "Impossibility of large phase shifts via the giant Kerr effect with single-photon wave packets", Phys. Rev. A **81**, 043823 (2010).

[68] I. Friedler, D. Petrosyan, M. Fleischhauer, and G. Kurizki, "Long-range interactions and entanglement of slow single-photon pulses", Phys. Rev. A **72**, 043803 (2005).

[69] P. Bienias, S. Choi, O. Firstenberg, M. F. Maghrebi, M. Gullans, M. D. Lukin, A. V. Gorshkov, and H. P. Büchler, "Scattering resonances and bound states for strongly interacting Rydberg polaritons", Phys. Rev. A **90**, 053804 (2014).

[70] D. Paredes-Barato and C. S. Adams, "All-Optical Quantum Information Processing Using Rydberg Gates", Phys. Rev. Lett. **112**, 040501 (2014).

[71] M. Khazali, K. Heshami, and C. Simon, "Photon-photon gate via the interaction between two collective Rydberg excitations", Phys. Rev. A **91**, 030301 (2015).

[72] L. Isenhower, E. Urban, X. L. Zhang, A. T. Gill, T. Henage, T. A. Johnson, T. G. Walker, and M. Saffman, "Demonstration of a Neutral Atom Controlled-NOT Quantum Gate", Phys. Rev. Lett. **104**, 010503 (2010).

[73] T. Wilk, A. Gaëtan, C. Evellin, J. Wolters, Y. Miroshnychenko, P. Grangier, and A. Browaeys, "Entanglement of Two Individual Neutral Atoms Using Rydberg Blockade", Phys. Rev. Lett. **104**, 010502 (2010).

[74] M. Kohnen, M. Succo, P. G. Petrov, R. A. Nyman, M. Trupke, and E. A. Hinds, "An array of integrated atom–photon junctions", Nat. Photon. **5**, 35–38 (2011).

[75] J. A. Sedlacek, E. Kim, S. T. Rittenhouse, P. F. Weck, H. R. Sadeghpour, and J. P. Shaffer, "Electric Field Cancellation on Quartz by

Rb Adsorbate-Induced Negative Electron Affinity", Phys. Rev. Lett. **116**, 133201 (2016).

[76] C. Hermann-Avigliano, R. C. Teixeira, T. L. Nguyen, T. Cantat-Moltrecht, G. Nogues, I. Dotsenko, S. Gleyzes, J. M. Raimond, S. Haroche, and M. Brune, "Long coherence times for Rydberg qubits on a superconducting atom chip", Phys. Rev. A **90**, 040502 (2014).

[77] J. Naber, S. Machluf, L. Torralbo-Campo, M. L. Soudijn, N. J. van Druten, H. B. van Linden van den Heuvell, and R. J. C. Spreeuw, "Adsorbate dynamics on a silica-coated gold surface measured by Rydberg Stark spectroscopy", J. Phys. B: At. Mol. Opt. Phys. **49**, 094005 (2016).

[78] C. Conti, M. Peccianti, and G. Assanto, "Observation of Optical Spatial Solitons in a Highly Nonlocal Medium", Phys. Rev. Lett. **92**, 113902 (2004).

[79] M. Peccianti, C. Conti, G. Assanto, A. De Luca, and C. Umeton, "Routing of anisotropic spatial solitons and modulational instability in liquid crystals", Nature **432**, 733–737 (2004).

[80] C. Rotschild, O. Cohen, O. Manela, M. Segev, and T. Carmon, "Solitons in Nonlinear Media with an Infinite Range of Nonlocality: First Observation of Coherent Elliptic Solitons and of Vortex-Ring Solitons", Phys. Rev. Lett. **95**, 213904 (2005).

[81] D. Suter and T. Blasberg, "Stabilization of transverse solitary waves by a nonlocal response of the nonlinear medium", Phys. Rev. A **48**, 4583–4587 (1993).

[82] C. Rotschild, B. Alfassi, O. Cohen, and M. Segev, "Long-range interactions between optical solitons", Nat. Phys **2**, 769–774 (2006).

[83] E. Knill, R. Laflamme, and G. J. Milburn, "A scheme for efficient quantum computation with linear optics", Nature **409**, 46–52 (2001).

[84] J.-W. Pan, D. Bouwmeester, H. Weinfurter, and A. Zeilinger, "Experimental Entanglement Swapping: Entangling Photons That Never Interacted", Phys. Rev. Lett. **80**, 3891–3894 (1998).

[85] H. Busche, P. Huillery, S. W. Ball, T. V. Ilieva, M. P. A. Jones, and C. S. Adams, "Contactless non-linear optics mediated by long-range Rydberg interactions", Nat. Phys., to appear (2017).

[86] L. Béguin, A. Vernier, R. Chicireanu, T. Lahaye, and A. Browaeys, "Direct Measurement of the van der Waals Interaction between Two Rydberg Atoms", Phys. Rev. Lett. **110**, 263201 (2013).

[87] M. Ebert, M. Kwon, T. G. Walker, and M. Saffman, "Coherence and Rydberg Blockade of Atomic Ensemble Qubits", Phys. Rev. Lett. **115**, 093601 (2015).

[88] H. Busche, S. W. Ball, and P. Huillery, "A high repetition rate experimental setup for quantum non-linear optics with cold Rydberg atoms", Eur. Phys. J. Spec. Top. **225**, 2839–2861 (2016).

[89] E. Distante, A. Padrón-Brito, M. Cristiani, D. Paredes-Barato, and H. de Riedmatten, "Storage Enhanced Nonlinearities in a Cold Atomic Rydberg Ensemble", Phys. Rev. Lett. **117**, 113001 (2016).

[90] J. D. Thompson, T. L. Nicholson, Q.-Y. Liang, S. H. Cantu, C. S. Venkatramani A. V., I. A. Fedorov, D. Viscor, T. Pohl, M. D. Lukin, and V. Vuletić, "Symmetry-protected collisions between strongly interacting photons", Nature **542**, 206–209 (2017).

[91] H. J. Metcalf and P. van der Straten, *Laser Cooling and Trapping*, 1st ed. (Springer, New York, 1999).

[92] R. Grimm, M. Weidemüller, and Y. B. Ovchinnikov, "Optical dipole traps for neutral atoms", in *Advances in Atomic, Molecular and Optical Physics, Volume 42*, edited by B. Bederson and H. Walther (Academic Press, 1999), pp. 95–170.

[93] Y. R. P. Sortais, H. Marion, C. Tuchendler, A. M. Lance, M. Lamare, P. Fournet, C. Armellin, R. Mercier, G. Messin, A. Browaeys, and P. Grangier, "Diffraction-limited optics for single-atom manipulation", Phys. Rev. A **75**, 013406 (2007).

[94] K. Dieckmann, R. J. C. Spreeuw, M. Weidemüller, and J. T. M. Walraven, "Two-dimensional magneto-optical trap as a source of slow atoms", Phys. Rev. A **58**, 3891–3895 (1998).

[95] A. Browaeys, D. Barredo, and T. Lahaye, "Experimental investigations of dipole–dipole interactions between a few Rydberg atoms", J. Phys. B: At.,Mol. Opt. Phys. **49**, 152001 (2016).

[96] F. Nogrette, H. Labuhn, S. Ravets, D. Barredo, L. Béguin, A. Vernier, T. Lahaye, and A. Browaeys, "Single-Atom Trapping in Holographic 2D Arrays of Microtraps with Arbitrary Geometries", Phys. Rev. X **4**, 021034 (2014).

[97] M. Saffman, "Quantum computing with atomic qubits and Rydberg interactions: progress and challenges", J. Phys. B: At. Mol. Opt. Phys. **49**, 202001 (2016).

[98] H. Labuhn, D. Barredo, S. Ravets, S. de Léséleuc, T. Macrì, T. Lahaye, and A. Browaeys, "Tunable two-dimensional arrays of single Rydberg atoms for realizing quantum Ising models", Nature **534**, 667–670 (2016).

[99] M. Ebert, A. Gill, M. Gibbons, X. Zhang, M. Saffman, and T. G. Walker, "Atomic Fock State Preparation Using Rydberg Blockade", Phys. Rev. Lett. **112**, 043602 (2014).

[100] C. Ates, I. Lesanovsky, C. S. Adams, and K. J. Weatherill, "Fast and Quasideterministic Single Ion Source from a Dipole-Blockaded Atomic Ensemble", Phys. Rev. Lett. **110**, 213003 (2013).

[101] C. S. Hofmann, G. Günter, H. Schempp, N. L. M. Müller, A. Faber, H. Busche, M. Robert-de-Saint-Vincent, S. Whitlock, and M. Weidemüller, "An experimental approach for investigating many-body phenomena in Rydberg-interacting quantum systems", Front. Phys. **9**, 571–586 (2014).

[102] J. R. Rydberg, "XXXIV. On the structure of the line-spectra of the chemical elements", Philos. Mag. **29**, 331–337 (1890).

[103] N. Bohr, "I. On the constitution of atoms and molecules", Philos. Mag. **26**, 1–25 (1913).

[104] J. D. Pritchard, "Cooperative Optical Non-linearity in a blockaded Rydberg ensemble", PhD thesis (Durham University, 2011).

[105] M. L. Zimmerman, M. G. Littman, M. M. Kash, and D. Kleppner, "Stark structure of the Rydberg states of alkali-metal atoms", Phys. Rev. A **20**, 2251–2275 (1979).

[106] M. T. Frey, X. Ling, B. G. Lindsay, K. A. Smith, and F. B. Dunning, "Use of the Stark effect to minimize residual electric fields in an experimental volume", Rev. Sci. Inst. **64**, 3649–3650 (1993).

[107] A. Osterwalder and F. Merkt, "Using High Rydberg States as Electric Field Sensors", Phys. Rev. Lett. **82**, 1831–1834 (1999).

[108] A. K. Mohapatra, M. G. Bason, B. Butscher, K. J. Weatherill, and C. S. Adams, "A giant electro-optic effect using polarizable dark states", Nat. Phys. **4**, 890–894 (2008).

[109] A. Tauschinsky, R. M. T. Thijssen, S. Whitlock, H. B. van Linden van den Heuvell, and R. J. C. Spreeuw, "Spatially resolved excitation of Rydberg atoms and surface effects on an atom chip", Phys. Rev. A **81**, 063411 (2010).

[110] J. Grimmel, M. Mack, F. Karlewski, F. Jessen, M. Reinschmidt, N. Sándor, and J. Fortágh, "Measurement and numerical calculation of Rubidium Rydberg Stark spectra", New J. Phys. **17**, 053005 (2015).

[111] A. Facon, E.-K. Dietsche, D. Grosso, S. Haroche, J.-M. Raimond, M. Brune, and S. Gleyzes, "A sensitive electrometer based on a Rydberg atom in a Schrödinger-cat state", Nature **535**, 262–265 (2016).

[112] J. A. Sedlacek, A. Schwettmann, H. Kübler, R. Löw, T. Pfau, and J. P. Shaffer, "Microwave electrometry with Rydberg atoms in a vapour cell using bright atomic resonances", Nat. Phys. **8**, 819–824 (2012).

[113] H. Weimer, M. Müller, I. Lesanovsky, P. Zoller, and H. P. Büchler, "A Rydberg quantum simulator", Nat. Phys. **6**, 382–386 (2010).

[114] P. Schauß, J. Zeiher, T. Fukuhara, S. Hild, M. Cheneau, T. Macrì, T. Pohl, I. Bloch, and C. Gross, "Crystallization in Ising quantum magnets", Science **347**, 1455–1458 (2015).

[115] J. Zeiher, R. van Bijnen, P. Schauß, S. Hild, J.-Y. Choi, T. Pohl, I. Bloch, and C. Gross, "Many-body interferometry of a Rydberg-dressed spin lattice", Nat. Phys. **6**, 382–386 (2010).

[116] D. Jaksch, J. I. Cirac, P. Zoller, S. L. Rolston, R. Côté, and M. D. Lukin, "Fast Quantum Gates for Neutral Atoms", Phys. Rev. Lett. **85**, 2208–2211 (2000).

[117] K. J. Weatherill, J. D. Pritchard, R. P. Abel, M. G. Bason, A. K. Mohapatra, and C. S. Adams, "Electromagnetically induced transparency of an interacting cold Rydberg ensemble", J. Phys. B: At. Mol. Opt. Phys. **41**, 201002 (2008).

[118] M. J. Seaton, "The quantum defect method", Mon. Not. R. Astron. Soc. **118**, 504–518 (1958).

[119] W. Li, I. Mourachko, M. W. Noel, and T. F. Gallagher, "Millimeter-wave spectroscopy of cold Rb Rydberg atoms in a magneto-optical trap: Quantum defects of the *ns* , *np* , and *nd* series", Phys. Rev. A **67**, 052502 (2003).

[120] J. Han, Y. Jamil, D. V. L. Norum, P. J. Tanner, and T. F. Gallagher, "Rb nf quantum defects from millimeter-wave spectroscopy of cold ^{85}Rb Rydberg atoms", Phys. Rev. A **74**, 054502 (2006).

[121] M. F. Maghrebi, M. J. Gullans, P. Bienias, S. Choi, I. Martin, O. Firstenberg, M. D. Lukin, H. P. Büchler, and A. V. Gorshkov, "Coulomb Bound States of Strongly Interacting Photons", Phys. Rev. Lett. **115**, 123601 (2015).

[122] M. Moos, M. Höning, R. Unanyan, and M. Fleischhauer, "Many-body physics of Rydberg dark-state polaritons in the strongly interacting regime", Phys. Rev. A **92**, 053846 (2015).

[123] J. D. Jackson, *Classical Electrodynamics*, 3rd ed. (John Wiley & Sons, New York, 1998).

[124] K. Singer, J. Stanojevic, M. Weidemüller, and R. Côté, "Long-range interactions between alkali Rydberg atom pairs correlated to the *ns–ns*, *np–np* and *nd–nd* asymptotes", J. Phys. B: At. Mol. Opt. Phys. **38**, S295 (2005).

[125] N. Šibalić, J. D. Pritchard, C. S. Adams, and K. J. Weatherhill, "ARC: An open-source library for calculating properties of alkali Rydberg atoms", arXiv:1612.05529v1 (2016).

[126] J. Han and T. F. Gallagher, "Millimeter-wave rubidium Rydberg van der Waals spectroscopy", Phys. Rev. A **79**, 053409 (2009).

[127] I. I. Ryabtsev, D. B. Tretyakov, I. I. Beterov, and V. M. Entin, "Observation of the Stark-Tuned Förster Resonance between Two Rydberg Atoms", Phys. Rev. Lett. **104**, 073003 (2010).

[128] J. Nipper, J. B. Balewski, A. T. Krupp, B. Butscher, R. Löw, and T. Pfau, "Highly Resolved Measurements of Stark-Tuned Förster Resonances between Rydberg Atoms", Phys. Rev. Lett. **108**, 113001 (2012).

[129] K. A. Safinya, J. F. Delpech, F. Gounand, W. Sandner, and T. F. Gallagher, "Resonant Rydberg-Atom-Rydberg-Atom Collisions", Phys. Rev. Lett. **47**, 405–408 (1981).

[130] W. R. Anderson, J. R. Veale, and T. F. Gallagher, "Resonant Dipole-Dipole Energy Transfer in a Nearly Frozen Rydberg Gas", Phys. Rev. Lett. **80**, 249–252 (1998).

[131] I. Mourachko, D. Comparat, F. de Tomasi, A. Fioretti, P. Nosbaum, V. M. Akulin, and P. Pillet, "Many-Body Effects in a Frozen Rydberg Gas", Phys. Rev. Lett. **80**, 253–256 (1998).

[132] T. Förster, "Zwischenmolekulare Energiewanderung und Fluoreszenz", Ann. Phys. **437**, 55–75 (1948).

[133] S. Ravets, H. Labuhn, D. Barredo, L. Béguin, T. Lahaye, and A. Browaeys, "Coherent dipole–dipole coupling between two single Rydberg atoms at an electrically-tuned Förster resonance", Nat. Phys. **10**, 914–917 (2014).

[134] C. Chin, R. Grimm, P. Julienne, and E. Tiesinga, "Feshbach resonances in ultracold gases", Rev. Mod. Phys. **82**, 1225–1286 (2010).

[135] R. Faoro, B. Pelle, A. Zuliani, P. Cheniet, E. Arimondo, and P. Pillet, "Borromean three-body FRET in frozen Rydberg gases", Nat. Commun. **6**, 8173 (2015).

[136] J. H. Gurian, P. Cheinet, P. Huillery, A. Fioretti, J. Zhao, P. L. Gould, D. Comparat, and P. Pillet, "Observation of a Resonant Four-Body Interaction in Cold Cesium Rydberg Atoms", Phys. Rev. Lett. **108**, 023005 (2012).

[137] C. S. E. van Ditzhuijzen, A. F. Koenderink, J. V. Hernández, F. Robicheaux, L. D. Noordam, and H. B.v. L. van den Heuvell, "Spatially Resolved Observation of Dipole-Dipole Interaction between Rydberg Atoms", Phys. Rev. Lett. **100**, 243201 (2008).

[138] D. Barredo, H. Labuhn, S. Ravets, T. Lahaye, A. Browaeys, and C. S. Adams, "Coherent Excitation Transfer in a Spin Chain of Three Rydberg Atoms", Phys. Rev. Lett. **114**, 113002 (2015).

[139] S. Ravets, H. Labuhn, D. Barredo, T. Lahaye, and A. Browaeys, "Measurement of the angular dependence of the dipole-dipole interaction between two individual Rydberg atoms at a Förster resonance", Phys. Rev. A **92**, 020701 (2015).

[140] L. D. Carr, D. DeMille, R. V. Krems, and J. Ye, "Cold and ultracold molecules: science, technology and applications", New J. Phys. **11**, 055049 (2009).

[141] S. A. Moses, J. P. Covey, M. T. Miecnikowski, D. S. Jin, and J. Ye, "New frontiers for quantum gases of polar molecules", Nat. Phys. **13**, 23–20 (2017).

[142] T. Lahaye, C. Menotti, L. Santos, M. Lewenstein, and T. Pfau, "The physics of dipolar bosonic quantum gases", Rep. Prog. Phys. **72**, 126401 (2009).

[143] M. A. Baranov, M. Dalmonte, G. Pupillo, and P. Zoller, "Condensed Matter Theory of Dipolar Quantum Gases", Chem. Rev. **112**, PMID: 22877362, 5012–5061 (2012).

[144] T. C. Liebisch, A. Reinhard, P. R. Berman, and G. Raithel, "Atom Counting Statistics in Ensembles of Interacting Rydberg Atoms", Phys. Rev. Lett. **95**, 253002 (2005).

[145] M. Viteau, P. Huillery, M. G. Bason, N. Malossi, D. Ciampini, O. Morsch, E. Arimondo, D. Comparat, and P. Pillet, "Cooperative Excitation and Many-Body Interactions in a Cold Rydberg Gas", Phys. Rev. Lett. **109**, 053002 (2012).

[146] H. Schempp, G. Günter, M. Robert-de-Saint-Vincent, C. S. Hofmann, D. Breyel, A. Komnik, D. W. Schönleber, M. Gärttner, J. Evers, S. Whitlock, and M. Weidemüller, "Full Counting Statistics of Laser Excited Rydberg Aggregates in a One-Dimensional Geometry", Phys. Rev. Lett. **112**, 013002 (2014).

[147] N. Malossi, M. M. Valado, S. Scotto, P. Huillery, P. Pillet, D. Ciampini, E. Arimondo, and O. Morsch, "Full Counting Statistics and Phase Diagram of a Dissipative Rydberg Gas", Phys. Rev. Lett. **113**, 023006 (2014).

[148] A. Schwarzkopf, R. E. Sapiro, and G. Raithel, "Imaging Spatial Correlations of Rydberg Excitations in Cold Atom Clouds", Phys. Rev. Lett. **107**, 103001 (2011).

[149] P. Schauß, M. Cheneau, M. Endres, T. Fukuhara, S. Hild, A. Omran, T. Pohl, C. Gross, S. Kuhr, and I. Bloch, "Observation of spatially ordered structures in a two-dimensional Rydberg gas", Nature **491**, 87–91 (2012).

[150] T. Pohl, E. Demler, and M. D. Lukin, "Dynamical Crystallization in the Dipole Blockade of Ultracold Atoms", Phys. Rev. Lett. **104**, 043002 (2010).

[151] R. M. W. van Bijnen, S. Smit, K. A. H. van Leeuwen, E. J. D. Vredenbregt, and S. J.J.M. F. Kokkelmans, "Adiabatic formation of Rydberg crystals with chirped laser pulses", J. Phys. B: At. Mol. Opt. Phys. **44**, 184008 (2011).

[152] Y. O. Dudin, L. Li, F. Bariani, and A. Kuzmich, "Observation of coherent many-body Rabi oscillations", Nat. Phys. **8**, 790–794 (2012).

[153] D. Barredo, S. Ravets, H. Labuhn, L. Béguin, A. Vernier, F. Nogrette, T. Lahaye, and A. Browaeys, "Demonstration of a Strong Rydberg Blockade in Three-Atom Systems with Anisotropic Interactions", Phys. Rev. Lett. **112**, 183002 (2014).

[154] J. Zeiher, P. Schauß, S. Hild, T. Macrì, I. Bloch, and C. Gross, "Microscopic Characterization of Scalable Coherent Rydberg Superatoms", Phys. Rev. X **5**, 031015 (2015).

[155] M. Saffman and T. G. Walker, "Creating single-atom and single-photon sources from entangled atomic ensembles", Phys. Rev. A **66**, 065403 (2002).

[156] M. O. Scully, E. S. Fry, C. H. R. Ooi, and K. Wódkiewicz, "Directed Spontaneous Emission from an Extended Ensemble of N Atoms: Timing Is Everything", Phys. Rev. Lett. **96**, 010501 (2006).

[157] L. H. Pedersen and K. Mølmer, "Few qubit atom-light interfaces with collective encoding", Phys. Rev. A **79**, 012320 (2009).

[158] R. H. Dicke, "Coherence in Spontaneous Radiation Processes", Phys. Rev. **93**, 99–110 (1954).

[159] J. Gea-Banacloche, Y.-Q. Li, S.-Z. Jin, and M. Xiao, "Electromagnetically induced transparency in ladder-type inhomogeneously broadened media: Theory and experiment", Phys. Rev. A **51**, 576–584 (1995).

[160] T. Baluktsian, B. Huber, R. Löw, and T. Pfau, "Evidence for Strong van der Waals Type Rydberg-Rydberg Interaction in a Thermal Vapor", Phys. Rev. Lett. **110**, 123001 (2013).

[161] B. Darquié, M. P. A. Jones, J. Dingjan, J. Beugnon, S. Bergamini, Y. Sortais, G. Messin, A. Browaeys, and P. Grangier, "Controlled Single-Photon Emission from a Single Trapped Two-Level Atom", Science **309**, 454–456 (2005).

[162] F. Diedrich and H. Walther, "Nonclassical radiation of a single stored ion", Phys. Rev. Lett. **58**, 203–206 (1987).

[163] R. Loudon, *The Quantum Theory of Light*, 3rd ed. (Oxford University Press, Oxford, 2000).

[164] S. H. Autler and C. H. Townes, "Stark Effect in Rapidly Varying Fields", Phys. Rev. **100**, 703–722 (1955).

[165] S. E. Harris, J. E. Field, and A. Kasapi, "Dispersive properties of electromagnetically induced transparency", Phys. Rev. A **46**, R29–R32 (1992).

[166] A. Kasapi, M. Jain, G. Y. Yin, and S. E. Harris, "Electromagnetically Induced Transparency: Propagation Dynamics", Phys. Rev. Lett. **74**, 2447–2450 (1995).

[167] O. Schmidt, R. Wynands, Z. Hussein, and D. Meschede, "Steep dispersion and group velocity below $\frac{c}{3000}$ in coherent population trapping", Phys. Rev. A **53**, R27–R30 (1996).

[168] M. M. Kash, V. A. Sautenkov, A. S. Zibrov, L. Hollberg, G. R. Welch, M. D. Lukin, Y. Rostovtsev, E. S. Fry, and M. O. Scully, "Ultraslow Group Velocity and Enhanced Nonlinear Optical Effects in a Coherently Driven Hot Atomic Gas", Phys. Rev. Lett. **82**, 5229–5232 (1999).

[169] D. Budker, D. F. Kimball, S. M. Rochester, and V. V. Yashchuk, "Nonlinear Magneto-optics and Reduced Group Velocity of Light in Atomic Vapor with Slow Ground State Relaxation", Phys. Rev. Lett. **83**, 1767–1770 (1999).

[170] M. Fleischhauer and M. D. Lukin, "Quantum memory for photons: Dark-state polaritons", Phys. Rev. A **65**, 022314 (2002).

[171] D. F. Phillips, A. Fleischhauer, A. Mair, R. L. Walsworth, and M. D. Lukin, "Storage of Light in Atomic Vapor", Phys. Rev. Lett. **86**, 783–786 (2001).

[172] A. V. Gorshkov, R. Nath, and T. Pohl, "Dissipative Many-Body Quantum Optics in Rydberg Media", Phys. Rev. Lett. **110**, 153601 (2013).

[173] E. T. Jaynes and F. W. Cummings, "Comparison of quantum and semiclassical radiation theories with application to the beam maser", Proc. IEEE **51**, 89–109 (1963).

[174] J. Honer, R. Löw, H. Weimer, T. Pfau, and H. P. Büchler, "Artificial Atoms Can Do More Than Atoms: Deterministic Single Photon Subtraction from Arbitrary Light Fields", Phys. Rev. Lett. **107**, 093601 (2011).

[175] A. V. Gorshkov, A. André, M. Fleischhauer, A. S. Sørensen, and M. D. Lukin, "Universal Approach to Optimal Photon Storage in Atomic Media", Phys. Rev. Lett. **98**, 123601 (2007).

[176] A. V. Gorshkov, A. André, M. D. Lukin, and A. S. Sørensen, "Photon storage in Λ-type optically dense atomic media. II. Free-space model", Phys. Rev. A **76**, 033805 (2007).

[177] S. D. Jenkins, T Zhang, and T. A. B. Kennedy, "Motional dephasing of atomic clock spin waves in an optical lattice", J. Phys. B: At. Mol. Opt. Phys. **45**, 124005 (2012).

[178] K. Bergmann, H. Theuer, and B. W. Shore, "Coherent population transfer among quantum states of atoms and molecules", Rev. Mod. Phys. **70**, 1003–1025 (1998).

[179] Y.-H. Chen, M.-J. Lee, I.-C. Wang, S. Du, Y.-F. Chen, Y.-C. Chen, and I. A. Yu, "Coherent Optical Memory with High Storage Efficiency and Large Fractional Delay", Phys. Rev. Lett. **110**, 083601 (2013).

[180] Y.-F. Hsiao, P.-J. Tsai, H.-S. Chen, S.-X. Lin, C. C. Hung, C. Y.-H. Lee C.-H., Y.-F. Chen, I. A. Yu, and Y.-C. Chen, "EIT-based pho-

tonic memory with near-unity storage efficiency", arXiv:1605.08519 (2016).

[181] L. Li and A. Kuzmich, "Quantum memory with strong and controllable Rydberg-level interactions", Nat. Commun. **7**, 13618 (2016).

[182] B. Zhao, Y.-A. Chen, X.-H. Bao, T. Strassel, C.-S. Chuu, X.-M. Jin, J. Schemidmayer, Z.-S. Yuan, S. Chen, and J.-W. Pan, "A Millisecond Quantum Memory for Scalable Quantum Networks", Nat. Phys **5**, 95–99 (2009).

[183] R. Zhao, Y. O. Dudin, S. D. Jenkins, C. J. Campbell, D. N. Matsukevich, T. A. B. Kennedy, and A. Kuzmich, "Long-lived quantum memory", Nat. Phys **5**, 100–104 (2009).

[184] U. Schnorrberger, J. D. Thompson, S. Trotzky, R. Pugatch, N. Davidson, S. Kuhr, and I. Bloch, "Electromagnetically Induced Transparency and Light Storage in an Atomic Mott Insulator", Phys. Rev. Lett. **103**, 033003 (2009).

[185] Y. O. Dudin, L. Li, and A. Kuzmich, "Light storage on the time scale of a minute", Phys. Rev. A **87**, 031801 (2013).

[186] E. Amaldi and E. Segré, "Effect of Pressure on High Terms of Alkaline Spectra", Nature **133**, 141 (1934).

[187] C. H. Greene, A. S. Dickinson, and H. R. Sadeghpour, "Creation of Polar and Nonpolar Ultra-Long-Range Rydberg Molecules", Phys. Rev. Lett. **85**, 2458–2461 (2000).

[188] V. Bendkowsky, B. Butscher, J. Nipper, J. P. Shaffer, R. Löw, and T. Pfau, "Observation of ultralong-range Rydberg molecules", Nature **458**, 1005–1008 (2009).

[189] A. Gaj, A. T. Krupp, J. B. Balewski, R. Löw, S. Hofferberth, and T. Pfau, "From molecular spectra to a density shift in dense Rydberg gases", Nat. Commun. **5**, 4546 (2014).

[190] J. B. Balewski, A. T. Krupp, A. Gaj, D. Peter, H. P. Büchler, R. Löw, S. Hofferberth, and T. Pfau, "Coupling a single electron to a Bose–Einstein condensate", Nature **502**, 664–667 (2013).

[191] M. Gärttner and J. Evers, "Nonlinear absorption and density-dependent dephasing in Rydberg electromagnetically-induced-transparency media", Phys. Rev. A **88**, 033417 (2013).

[192] T. Niederprüm, O. Thomas, T. Manthey, T. M. Weber, and H. Ott, "Giant Cross Section for Molecular Ion Formation in Ultracold Rydberg Gases", Phys. Rev. Lett. **115**, 013003 (2015).

[193] E. L. Raab, M. Prentiss, A. Cable, S. Chu, and D. E. Pritchard, "Trapping of Neutral Sodium Atoms with Radiation Pressure", Phys. Rev. Lett. **59**, 2631–2634 (1987).

[194] S. Chu, J. E. Bjorkholm, A. Ashkin, and A. Cable, "Experimental Observation of Optically Trapped Atoms", Phys. Rev. Lett. **57**, 314–317 (1986).

[195] M. H. Anderson, J. R. Ensher, M. R. Matthews, C. E. Wieman, and E. A. Cornell, "Observation of Bose-Einstein Condensation in a Dilute Atomic Vapor", Science **269**, 198–201 (1995).

[196] K. B. Davis, M. O. Mewes, M. R. Andrews, N. J. van Druten, D. S. Durfee, D. M. Kurn, and W. Ketterle, "Bose-Einstein Condensation in a Gas of Sodium Atoms", Phys. Rev. Lett. **75**, 3969–3973 (1995).

[197] B. DeMarco and D. S. Jin, "Onset of Fermi Degeneracy in a Trapped Atomic Gas", Science **285**, 1703–1706 (1999).

[198] K. J. Weatherill, J. D. Pritchard, P. F. Griffin, U. Dammalapati, C. S. Adams, and E. Riis, "A versatile and reliably reusable ultrahigh vacuum viewport", Rev. Sci. Instrum. **80**, 026105 (2009).

[199] R. P. Abel, C. Carr, U. Krohn, and C. S. Adams, "Electrometry near a dielectric surface using Rydberg electromagnetically induced transparency", Phys. Rev. A **84**, 023408 (2011).

[200] W. S. Bakr, A. Peng, M. E. Tai, R. Ma, J. Simon, J. I. Gillen, S. Fölling, L. Pollet, and M. Greiner, "Probing the Superfluid–to–Mott Insulator Transition at the Single-Atom Level", Science **329**, 547–550 (2010).

[201] J. F. Sherson, C. Weitenberg, M. Endres, M. Cheneau, I. Bloch, and S. Kuhr, "Single-atom-resolved fluorescence imaging of an atomic Mott insulator", Nature **467**, 68–72 (2010).

[202] C. Weitenberg, M. Endres, J. F. Sherson, M. Cheneau, P. Schauß, T. Fukahara, I. Bloch, and S. Kuhr, "Single-spin addressing in an atomic Mott insulator", Nature **471**, 319–324 (2011).

[203] J. D. Carter, O. Cherry, and J. D. D. Martin, "Electric-field sensing near the surface microstructure of an atom chip using cold Rydberg atoms", Phys. Rev. A **86**, 053401 (2012).

[204] D. Barredo, S. de Léséleuc, V. Lienhard, T. Lahaye, and A. Browaeys, "An atom-by-atom assembler of defect-free arbitrary two-dimensional atomic arrays", Science **354**, 1021–1023 (2016).

[205] H. Labuhn, "Creating arbitrary 2D arrays of single atoms for the simulation of spin systems with Rydberg states", Eur. Phys. J. Spec. Top. **225**, 2817–2838 (2016).

[206] H. Kurisu, K. Ishizawa, S. Yamamoto, M. Hesaka, and Y. Saito, "Application of titanium materials to vacuum chambers and components", J. Phys.: Conf. Ser. **100**, 092002 (2008).

[207] J. A. Sedlacek, A. Schwettmann, H. Kübler, and J. P. Shaffer, "Atom-Based Vector Microwave Electrometry Using Rubidium Rydberg Atoms in a Vapor Cell", Phys. Rev. Lett. **111**, 063001 (2013).

[208] K. S. Chan, M. Siercke, C. Hufnagel, and R. Dumke, "Adsorbate Electric Fields on a Cryogenic Atom Chip", Phys. Rev. Lett. **112**, 026101 (2014).

[209] H. Hattermann, M. Mack, F. Karlewski, F. Jessen, D. Cano, and J. Fortágh, "Detrimental adsorbate fields in experiments with cold Rydberg gases near surfaces", Phys. Rev. A **86**, 022511 (2012).

[210] A. Hindmarch, Private communication, 2013.

[211] R. Löw, H. Weimer, J. Nipper, J. B. Balewski, B. Butscher, H. P. Büchler, and T. Pfau, "An experimental and theoretical guide to strongly interacting Rydberg gases", J. Phys. B: At. Mol. Opt. Phys. **45**, 113001 (2012).

[212] M. Tanasittikosol, J. D. Pritchard, D. Maxwell, A. Gauguet, K. J. Weatherill, R. M. Potvliege, and C. S. Adams, "Microwave dressing of Rydberg dark states", J. Phys. B: At. Mol. Opt. Phys. **44**, 184020 (2011).

[213] L. A. Jones, J. D. Carter, and J. D. D. Martin, "Rydberg atoms with a reduced sensitivity to dc and low-frequency electric fields", Phys. Rev. A **87**, 023423 (2013).

[214] S. Sevinçli and T. Pohl, "Microwave control of Rydberg atom interactions", New J. Phys. **16**, 123036 (2014).

[215] D. A. Steck, *Rubidium 87 D Line Data*, (2009, accessed 20th February 2017) `http://steck.us/alkalidata/rubidium87numbers.pdf`.

[216] J. H. Shirley, "Modulation transfer processes in optical heterodyne saturation spectroscopy", Opt. Lett. **7**, 537–539 (1982).

[217] D. J. McCarron, S. A. King, and S. L. Cornish, "Modulation transfer spectroscopy in atomic rubidium", Meas. Sci. Technol. **19**, 105601 (2008).

[218] S. C. Bell, D. M. Heywood, J. D. White, J. D. Close, and R. E. Scholten, "Laser frequency offset locking using electromagnetically induced transparency", Appl. Phys. Lett. **90**, 171120 (2007).

[219] R. P. Abel, A. K. Mohapatra, M. G. Bason, J. D. Pritchard, K. J. Weatherill, U. Raitzsch, and C. S. Adams, "Laser frequency stabilization to excited state transitions using electromagnetically induced transparency in a cascade system", Appl. Phys. Lett. **94**, 071107 (2009).

[220] G. C. Bjorklund, "Frequency-modulation spectroscopy: a new method for measuring weak absorptions and dispersions", Opt. Lett. **5**, 15–17 (1980).

[221] T. P. Wiles, "Dynamics of bright solitary matter-waves", PhD thesis (Durham University, 2013).

[222] W. D. Phillips and H. Metcalf, "Laser Deceleration of an Atomic Beam", Phys. Rev. Lett. **48**, 596–599 (1982).

[223] T. G. Tiecke, S. D. Gensemer, A. Ludewig, and J. T. M. Walraven, "High-flux two-dimensional magneto-optical-trap source for cold lithium atoms", Phys. Rev. A **80**, 013409 (2009).

[224] S. Götz, B. Höltkemeier, C. S. Hofmann, D. Litsch, B. D. DePaola, and M. Weidemüller, "Versatile cold atom target apparatus", Rev. Sci. Instrum. **83**, 073112 (2012).

[225] B. Höltkemeier, "2D MOT as a source of a cold atom target", Diplomarbeit (Ruprecht-Karls-Universität Heidelberg, 2011).

[226] H. Busche, "Efficient loading of a magneto-optical trap for experiments with dense ultracold Rydberg gases", Diplomarbeit (Ruprecht-Karls-Universität Heidelberg, 2011).

[227] C. S. Hofmann, "Emergence of correlations in strongly interacting ultracold Rydberg gases", PhD thesis (Ruprecht-Karls-Universität Heidelberg, 2011).

[228] J. Schoser, A. Batär, R. Löw, V. Schweikhard, A. Grabowski, Y. B. Ovchinnikov, and T. Pfau, "Intense source of cold Rb atoms from a pure two-dimensional magneto-optical trap", Phys. Rev. A **66**, 023410 (2002).

[229] S. Chaudhuri, S. Roy, and C. S. Unnikrishnan, "Realization of an intense cold Rb atomic beam based on a two-dimensional magneto-optical trap: Experiments and comparison with simulations", Phys. Rev. A **74**, 023406 (2006).

[230] J. Catani, P. Maioli, L. De Sarlo, F. Minardi, and M. Inguscio, "Intense slow beams of bosonic potassium isotopes", Phys. Rev. A **73**, 033415 (2006).

[231] J. Ramirez-Serrano, N. Yu, J. M. Kohel, J. R. Kellogg, and L. Maleki, "Multistage two-dimensional magneto-optical trap as a compact cold atom beam source", Opt. Lett. **31**, 682–684 (2006).

[232] Y. Bruneau, G. Khalili, P. Pillet, and D. Comparat, "Guided and focused slow atomic beam from a 2 dimensional magneto optical trap", Eur. Phys. J. D **68**, 92 (2014).

[233] V. Carrat, C. Cabrera-Gutiérrez, M. Jacquey, J. W. Tabosa, B. V. de Lesegno, and L. Pruvost, "Long-distance channeling of cold atoms exiting a 2D magneto-optical trap by a Laguerre-Gaussian laser beam", Opt. Lett. **39**, 719–722 (2014).

[234] D. T. Maxwell, "Light storage and control of photon-photon interactions in a cold Rydberg gas", PhD thesis (Durham University, 2013).

[235] W. Ketterle, D. S. Durfee, and D. M. Stamper-Kurn, "Making, probing and understanding Bose-Einstein condensates", in *Bose-Einstein condensation in atomic gases, Proceedings of the International School of Physics Enrico Fermi, Course CXL*, edited by M. Inguscio, S. Stringari, and C. E. Wieman (IOS Press, Amsterdam, 1999), pp. 67–176.

[236] R. Hanbury-Brown and R. Q. Twiss, "Correlation between Photons in two Coherent Beams of Light", Nature **177**, 27–29 (1956).

[237] J. D. Miller, R. A. Cline, and D. J. Heinzen, "Far-off-resonance optical trapping of atoms", Phys. Rev. A **47**, R4567–R4570 (1993).

[238] A. S. Arnold, J. S. Wilson, and M. G. Boshier, "A simple extended-cavity diode laser", Rev. Sci. Instrum. **69**, 1236–1239 (1998).

[239] R. A. Nyman, G. Varoquaux, B. Villier, D. Sacchet, F. Moron, Y. Le Coq, A. Aspect, and P. Bouyer, "Tapered-amplified antireflection-

coated laser diodes for potassium and rubidium atomic-physics experiments", Rev. Sci. Instrum. **77**, 033105 (2006).

[240] W. Ketterle, K. B. Davis, M. A. Joffe, A. Martin, and D. E. Pritchard, "High densities of cold atoms in a *dark* spontaneous-force optical trap", Phys. Rev. Lett. **70**, 2253–2256 (1993).

[241] W. Petrich, M. H. Anderson, J. R. Ensher, and E. A. Cornell, "Behavior of atoms in a compressed magneto-optical trap", J. Opt. Soc. Am. B **11**, 1332–1335 (1994).

[242] P. D. Lett, R. N. Watts, C. I. Westbrook, W. D. Phillips, P. L. Gould, and H. J. Metcalf, "Observation of Atoms Laser Cooled below the Doppler Limit", Phys. Rev. Lett. **61**, 169–172 (1988).

[243] P. D. Lett, W. D. Phillips, S. L. Rolston, C. E. Tanner, R. N. Watts, and C. I. Westbrook, "Optical molasses", J. Opt. Soc. Am. B **6**, 2084–2107 (1989).

[244] C. S. Adams, H. J. Lee, N. Davidson, M. Kasevich, and S. Chu, "Evaporative Cooling in a Crossed Dipole Trap", Phys. Rev. Lett. **74**, 3577–3580 (1995).

[245] R. P. Abel, "Coherent excitation of ultracold atoms between ground and Rydberg states", PhD thesis (Durham University, 2011).

[246] M. Chalony, R. Pierrat, D. Delande, and D. Wilkowski, "Coherent flash of light emitted by a cold atomic cloud", Phys. Rev. A **84**, 011401 (2011).

[247] C. C. Kwong, T. Yang, M. S. Pramod, K. Pandey, D. Delande, R. Pierrat, and D. Wilkowski, "Cooperative Emission of a Coherent Superflash of Light", Phys. Rev. Lett. **113**, 223601 (2014).

[248] C. C. Kwong, T. Yang, D. Delande, R. Pierrat, and D. Wilkowski, "Cooperative Emission of a Pulse Train in an Optically Thick Scattering Medium", Phys. Rev. Lett. **115**, 223601 (2015).

[249] V. Vuletić, C. Chin, A. J. Kerman, and S. Chu, "Degenerate Raman Sideband Cooling of Trapped Cesium Atoms at Very High Atomic Densities", Phys. Rev. Lett. **81**, 5768–5771 (1998).

[250] I. G. Hughes and T. P. A. Hase, *Measurements And Their Uncertainties: A practical guide to modern error analysis*, 1st ed. (Oxford University Press, Oxford, 2009).

[251] F. Bariani and T. A. B. Kennedy, "Retrieval of multiple spin waves from a weakly excited, metastable atomic ensemble", Phys. Rev. A **85**, 033811 (2012).

[252] R. Boddeda, I. Usmani, E. Bimbard, A. Grankin, A. Ourjoumtsev, E. Brion, and P. Grangier, "Rydberg-induced optical nonlinearities from a cold atomic ensemble trapped inside a cavity", J. Phys. B: At. Mol. Opt. Phys. **49**, 084005 (2016).

[253] E. Distante, P. Farrera, A. Padrón-Brito, D. Paredes-Barato, G. Heinze, and H. de Riedmatten, "Storing single photons emitted by a quantum memory on a highly excited Rydberg state", Nat. Commun. **8**, 14072 (2017).

[254] Y.-Y. Jau, A. M. Hankin, T. Keating, I. H. Deutsch, and G. W. Biedermann, "Entangling atomic spins with a Rydberg-dressed spin-flip blockade", Nat. Phys. **12**, 71–74 (2016).

[255] M. Endres, H. Bernien, A. Keesling, H. Levine, E. R. Anschuetz, A. Krajenbrink, C. Senko, V. Vuletic, M. Greiner, and M. D. Lukin, "Atom-by-atom assembly of defect-free one-dimensional cold atom arrays", Science **354**, 1024–1027 (2016).

[256] B. Gouraud, D. Maxein, A. Nicolas, O. Morin, and J. Laurat, "Demonstration of a Memory for Tightly Guided Light in an Optical Nanofiber", Phys. Rev. Lett. **114**, 180503 (2015).

[257] C. Sayrin, C. Clausen, B. Albrecht, P. Schneeweiss, and A. Rauschenbeutel, "Storage of fiber-guided light in a nanofiber-trapped ensemble of cold atoms", Optica **2**, 353–356 (2015).

[258] A. L. Gaunt, T. F. Schmidutz, I. Gotlibovych, R. P. Smith, and Z. Hadzibabic, "Bose-Einstein Condensation of Atoms in a Uniform Potential", Phys. Rev. Lett. **110**, 200406 (2013).

[259] N. Šibalić, J. M. Kondo, C. S. Adams, and K. J. Weatherill, "Dressed-state electromagnetically induced transparency for light storage in uniform-phase spin waves", Phys. Rev. A **94**, 033840 (2016).

[260] R. J. Bettles, S. A. Gardiner, and C. S. Adams, "Enhanced Optical Cross Section via Collective Coupling of Atomic Dipoles in a 2D Array", Phys. Rev. Lett. **116**, 103602 (2016).

Acknowledgements

Over the past few years, Charles Adams has been a very inspiring supervisor. His intuition and enthusiasm for physics, and his creativity are impressive. I am very grateful for his constant support and guidance, as well as the trust, encouragement, and freedom he gave me when building, and later running, the new experiment. I am also very grateful to my co-supervisor Matt Jones. With his vast knowlegde of physics and on technical aspects, he has provided invaluable advice on many occasions, especially when things were going not too well, and his guidance has been extremely helpful during paper and thesis writing.

I would also like to thank the external examiners, Michel Brune and Nicholas Parker, for their interest in this work and the time and effort taken to examine this thesis as well as independent chair Ifan Hughes for the organisation of the examination process.

When I arrived in Durham, "Team Blockade" included Dan Maxwell, David Paredes, David Szwer, and Kevin Weatherill. Alongside Charles and Matt, they all provided valuable input on the new experimental setup and taught me a lot during discussions. I thank Kevin for his contributions and guidance during the design of the experimental setup and for answering countless questions on experimental design. David S. has adapted the experimental control system to our needs and without his work, we would not have been able to detect a single photon. We also benefited immensely from Dan's experience on the previous setup when trying to overlap three or more laser beams within a µm. Countless conversations with David P. helped to shape my understanding of Rydberg physics. Outside the lab and office, I enjoyed many afternoons playing board games and having excellent conversations with both Davids.

By the time the new experiment was being set up, "Team Blockade" had transformed into the somewhat more accurately, but less rebelliously, named "Rydberg Quantum Optics" team. I have to thank everyone for their contributions to the joined effort of building, maintaining, and running the experiment, to analysing our results and getting them published, as well as extensive proof reading of this thesis. Working with both teams was (and still is) a privilege. I spent countless days with Simon Ball winding

coils and cleaning vacuum parts, turning CAD drawings into an actual experiment. His excellent sense of humour brightened up many moments of encountering yet another obstacle to overcome. I was extremely lucky to work with Paul Huillery who is not only a highly talented and motivational postdoc, but also great company when staying late in the lab or pub. His guidance, support, and continued optimism are very much appreciated. Teodora Ilieva, together with Paul, started the effort to model our results. Besides excellent support in the lab, she also ensured a healthy regime of coffee breaks, making sure that I would take my mind off thesis and paper writing. I hope I will be able to return the favour and provide the same support during the final year of her PhD. Nick Spong joined our team when I was writing up. I thank him for proof reading almost the entire thesis and look forward to working with him over the next year. The experiment will be left in good hands with him.

Besides my immediate co-workers, I enjoyed sharing a somewhat cramped lab 54 with Kate Whittaker, Chris Wade, James Keaveney, Nikola Šibalić, and Chris Carr. Even though arguments over the choice of music in the lab resulted in occasional threats of fingerprints on optics (by some), they all were very pleasant company and I enjoyed many chats and discussions about physics, technical issues, and beyond.

The Durham AtMol group benefits from its great social atmosphere resulting in constant and informal exchange and collaboration across different projects. Consequently, I have to thank all group members for helping to resolve technical issues during quick chats over tea (or a pint on a Friday evening), sharing code, or lending out kit from the lab next door (which I hopefully returned). Besides those already mentioned, I would like to particularly thank Rob Bettles, Ifan Hughes, Dan Whiting, Dan Sadler, Ryan Hanley, Dani Pizzey, Liz Bridge, Alistair Bounds, Niamh Keegan, Massayuki Kondo, Tom Ogden, Steve Hopkins, Anna Marchant, and Ana Rakonjac. Ryan and Dani, along with James and Nikola, have also proof read parts of this thesis. An important thanks also goes to Simon Cornish and his group, in particular Tim Wiles, for sharing their excellent experimental control software.

Besides the AtMol group, this work was made possible by the support of many other people in the department. In particular, I thank Stephen Lishman and the mechanical workshop team for their continued support and excellent work, especially Malcolm Robertshaw for the in-vacuo mounts and Michael Clarey for the 2D MOT cage. I also thank Aidan Hindmarch, lecturer in the Centre of Materials Physics, for applying the platinum coatings to the lens mount.

I was maybe one of the last postgrads in England who benefited from funding by the European Union through the Marie Curie ITN "COHERENCE" (and later FET-PROACT project "RySQ"). Besides the generous financial support, I am equally grateful for the various schools, workshops, and conferences, and the continued exchange with other postgrads and researchers in the field. I would like to especially thank Antoine Browaeys and his group at the Institute d'Optique – Daniel Barredo, Henning Labuhn, Thierry Lahaye, Sylvain Ravets, Stephan Jennewein, and Yvan Sortais – for cooperation on the in-vacuo lenses, quick help during the "mouldy lens incident", and of course their hospitality while I spent a month working in their impressive lab. Henning, along with Tom Ogden, was also a great post-conference road trip companion in the "Canyonero". I also thank Matthias Weidemüller, coordinator of the network, and his group in Heidelberg, for the encouragement to apply for a PhD in Durham and everything I learnt from them about building cold atom apparatus, 2D MOTs, and Rydberg physics during my diploma work.

These acknowledgements would not be complete without thanking my friends back in Germany (and elsewhere) for their friendship and support despite my all too infrequent visits during the last years. I look forward to seeing you more often again. Last, but certainly not least, I am immensely grateful to my family for their continued support and understanding throughout the years. Thank you for everything you have done for me and for helping me to get to this point!